Astronomy Letters, Vol. 27, No. 2, 2001, pp. 108–117. Translated from Pis'ma v Astronomicheskiĭ Zhurnal, Vol. 27, No. 2, 2001, pp. 132–143.

Absolute Magnitudes and Kinematic Parameters of the Subsystem of RR Lyrae Variables

A. K. Dambis* and A. S. Rastorguev

Sternberg Astronomical Institute, Universitetskiĭ pr. 13, Moscow, 119899 Russia

Received February 23, 2000; in final form, April 20, 2000

Abstract—The statistical parallax technique is applied to a sample of 262 RRab Lyrae variables with published photoelectric photometry, metallicities, and radial velocities and with measured absolute proper motions. Hipparcos, PPM, NPM, and the Four-Million Star Catalog (Volchkov *et al.* 1992) were used as the sources of proper motions; the proper motions from the last three catalogs were reduced to the Hipparcos system. We determine parameters of the velocity distribution for halo [$(U_0, V_0, W_0) = (-9 \pm 12, -214 \pm 10, -16 \pm 7)$ km s^{-1} and $(\sigma_U, \sigma_V, \sigma_W) = (164 \pm 11, 105 \pm 7, 95 \pm 7)$ km s^{-1}] and thick-disk [$(U_0, V_0, W_0) = (-16 \pm 8, -41 \pm 7, -18 \pm 5)$ km s^{-1} and $(\sigma_U, \sigma_V, \sigma_W) = (53 \pm 9, 42 \pm 8, 26 \pm 5)$ km s^{-1}] RR Lyrae, as well as the intensity-averaged absolute magnitude for RR Lyrae of these populations: $\langle M_V \rangle = 0.77 \pm 0.10$ and $\langle M_V \rangle = +1.11 \pm 0.28$ for the halo and thick-disk objects, respectively. The metallicity dependence of the absolute magnitude of RR Lyrae is analyzed ($\langle M_V \rangle = (0.76 \pm 0.12) + (0.26 \pm 0.26) \cdot ([\mathrm{Fe/H}] + 1.6) = 1.17 + 0.26 \cdot [\mathrm{Fe/H}]$). Our results are in satisfactory agreement with the $\langle M_V \rangle$(RR)–[Fe/H] relation from Carney *et al.* (1992) ($\langle M_V \rangle(\mathrm{RR}) = 1.01 + 0.15 \cdot [\mathrm{Fe/H}]$) obtained by Baade–Wesselink's method. They provide evidence for a short distance scale: the LMC distance modulus and the distance to the Galactic center are 18.22 ± 0.11 and 7.4 ± 0.5 kpc, respectively. The zero point of the distance scale and the kinematic parameters of the RR Lyrae populations are shown to be virtually independent of the source of absolute proper motions used and of whether they are reduced to the Hipparcos system or not. © *2001 MAIK "Nauka/Interperiodica".*

Key words: *stars—variable and peculiar*

INTRODUCTION

RR Lyrae variables are among the tools of greatest value for determining the distances to old stellar systems both in our Galaxy and beyond, to globular clusters, Galactic center, and Local-Group galaxies. These stars are so important as one of the distance indicators in the Universe, because they have very similar luminosities [the dispersion of absolute magnitudes of RR Lyraes with the same metal abundance does not exceed $0^m.15$ (Sandage 1990)], are easy to discover (because of substantial variability), and can be reliably classified (by low metallicity, period, and the shape of the light curve). Thus the main task to be resolved in order to successfully use these stars to confidently measure the distances is to set the zero point of their distance scale, i.e., determine the mean absolute magnitude of RR Lyraes. Because of its high homogeneity, the subsystem of RR Lyraes in our Galaxy proves to be an ideal object for the application of the statistical parallax technique, which can yield not only the kinematic parameters of a stellar population but also to constrain with high accuracy the mean absolute magnitude of its constituent stars. The latter quantity is one of the fundamental parameters that form the basis of modern distance scale in the Universe.

Almost half a century ago, Pavlovskaya (1953) published her pioneering work where she used for the first time the statistical parallax technique to determine the absolute magnitude of RR Lyrae stars (with a standard error of $\sim 0^m.2$). Pavlovskaya's result made it necessary to reduce by $\sim 0^m.5$ the mean absolute magnitude of RR Lyraes adopted at that time and has led to a radical revision (reduction by a factor of ~1.25) of the then adopted distance scale. Later, as the amount of observational data increased, many other authors applied the statistical parallax technique to RR Lyrae stars (van Herk 1965; Hemenway 1975; Clube and Dawe 1980a; Hawley *et al.* 1986; Strugnell *et al.* 1986; Layden *et al.* 1996; Popowski and Gould 1998a, 1998b; Fernley *et al.* 1998, and Tsujimoto *et al.* 1998), and, in spite of some scatter in the results obtained, the latter invariably favored the short distance scale. A number of authors tried to increase the accuracy of the method. To this end, they abandoned numerous simplifying assumptions by applying the maximum likelihood method (Rigal 1958; Heck and Lakaye 1978; Clube and Dawe 1980a). However, only Hawley *et al.* (1986) and Strugnell *et al.* (1986) were the first to use this technique correctly. The latter two groups used the rigorous algorithm of multi-

* E-mail address for contacts: mirage@sai.msu.ru

dimensional minimization, also referred to as the simplex method and based on the method of Nedler and Mead (1965). Layden (1994) and Layden *et al.* (1996) used both their own observational material and the data by other authors to increase substantially the number of RR Lyrae stars with known metallicities, magnitudes, radial velocities, and proper motions. The above authors increased substantially the quality of the material used and applied the statistical parallax technique to the sample thus obtained (Layden *et al.* 1996). These efforts allowed the accuracy of both the inferred kinematical parameters of RR Lyrae type star population and the mean absolute magnitude of these stars to be increased: the standard error of the latter has been reduced to $0^m.12$. The result of Layden *et al.* (1996) was recently slightly refined by Popovski and Gould (1998a) (who used the same observational data) and also by Gould and Popovski (1998), Fernley *et al.* (1998), and Tsujimoto *et al.* (1998) [the latter three works made use of the proper motions measured by the Hipparcos satellite (ESA 1997)]. Note that all works published before Layden *et al.* (1996) used relative proper motions of RR Lyraes exclusively absolutized via statistical methods. The results thus obtained (especially, the kinematic parameters) could therefore depend on the assumptions used in absolutization (in particular, those concerning the kinematics of the reference stars). However, even Layden *et al.* (1996) were forced to use relative proper motions to obtain a balanced sample, because their main source of absolute proper motions—the NPM1 catalog (Klemola *et al.* 1993)—contains neither southern-sky stars (located south of $\delta = -23°$) nor stars located near the Galactic equator.

In recent years, the Astrometry Division of the Sternberg Astronomical Institute has created the Four-Million Catalog of positions and proper motions of stars (Volchkov *et al.* 1992), hereafter referred to as the 4M catalog for the sake of brevity. The proper motions of more than four million stars in this catalog were determined from the differences of coordinates given in the Astrographic Catalogue (Carte du Ciel) and the Hubble Space Telescope Guide Star Catalogue, and then reduced to the proper-motion system of the PPM catalog (Roser *et al.* 1991). Below, we give the reasons why it has become necessary, in our opinion, to apply once more the statistical parallax technique to RR Lyrae stars in order to further refine the mean absolute magnitude of these objects.

First, the 4M catalog gives us the so far largest sample (236 objects) of RR(ab) Lyraes for which the proper motions determined in a *homogeneous* system are available along with photoelectric magnitudes, metallicities, and radial velocities. Note for comparison that Layden *et al.* (1996) obtained their results from a sample of 213 stars using proper motions adopted from two sources (NPM1 catalog for 171 stars and a compilation of statistically absolutized proper motions for 52 stars).

Second, the 4M catalog, which covers the entire sky, makes it possible to abandon completely the use of statistically absolutized proper motions.

Third, we can now estimate to what degree the results obtained via statistical parallaxes depend on the nature and source of the adopted proper motions: statistically absolutized proper motions, absolute proper motions computed on a reference frame defined by distant galaxies (NPM1 catalog), absolute proper motions measured on board the Hipparcos satellite on a short time interval (~3 years), and absolute proper motions from the 4M catalog determined from two to four photographic positions spanning a time interval of ~100 years.

Fourth, the Hipparcos catalog (ESA 1997), which contains almost 120 000 stars with high-precision coordinates and proper motions allows an inertial reference frame and the corresponding system of proper motions to be determined with high accuracy. The latter can be used to reduce the proper motions adopted from other catalogs and to subsequently average the reduced proper motions in order build the so far largest and at the same time homogeneous sample of RR Lyraes with known metallicities, kinematic, and photometric (photoelectric) parameters.

THE METHOD

The essence of the statistical parallax technique consists in balancing the mean kinematic parameters of a stellar group as inferred from radial velocities and from the velocity vector components perpendicular to the line of sight, i.e., in the end, from the components of proper motion. The point is that the line-of-sight velocity component (i.e., radial velocity) is obtained directly from observations, whereas the components perpendicular to the line of sight are determined by multiplying the corresponding proper-motion components by a provisional distance to the star (usually the photometric distance determined from the observed magnitude, interstellar extinction, and an assumed absolute magnitude) and are therefore directly proportional to the adopted distance scale. This fundamental difference between the line-of-sight component of the full velocity vector and the two components perpendicular to it allows a correction factor to the adopted distance scale of objects under study to be estimated. The optimum factor is considered to be the value that ensures the best agreement of the inferred kinematic parameters with both observed radial velocities and proper motions of stars.

In this paper, we use the modern, most rigorous version of the statistical parallax technique, whose detailed description can be found in Murray's (1986) book (see page 284) and in the paper by Hawley *et al.* (1986). This method consists in simultaneous determination of the set of kinematic parameters (the vector of the full space velocity and the components of the velocity dispersion tensor) and the correction factor to the initial

distance scale to maximize the likelihood of the actual combination of the observed data (coordinates, relative distances, radial velocities, and proper motions).

INITIAL DATA

Metallicities, Radial Velocities, and Photometry

Our primary sources of metallicities ([Fe/H]) and radial velocities of RR Lyrae stars were the papers of Layden (1994) and Layden *et al.* (1996), which we supplemented by the data recently published by Fernley and Barnes (1997), Solano *et al.* (1997), and Fernley *et al.* (1998). We used the metallicities from the latter three papers only for the stars absent from Layden's lists [which provides the greatest [Fe/H] data set for field RR Lyraes homogeneously reduced to a single abundance scale that matches the globular-cluster metallicity scale of Zinn and West (1984)]. We reduced the corresponding data to the system adopted by Layden using the following relation:

$$[\mathrm{Fe/H}]_{\mathrm{Layden}} = [\mathrm{Fe/H}]_{\mathrm{Fernley\ and\ Solano}} - 0.16 \pm 0.13, \quad (1)$$

derived from 33 common stars.

As the main sources of radial velocities, we, on the contrary, used the lists of Fernley *et al.* (1998) and Solano *et al.* (1997), because the corresponding data are more accurate (they rely on original measurements and all earlier published data), supplementing them with the data adopted from Layden *et al.* (1996) and Layden (1994) for the stars lacking in the two lists mentioned above. Depending on the completeness of observational data available, the above authors determined the mean radial velocities by integrating radial-velocity curves, simple averaging of the measurements of different authors, or just gave the individual radial-velocity measurements (in the cases where only one measurement was available for the star). The resulting radial velocities have errors of less than 5 km s^{-1} for 97 stars, from 6 to 10 km s^{-1} for 62 stars, from 11 to 15 km s^{-1} for 38 stars, and only 65 stars have their radial velocities measured with errors exceeding 15 km s^{-1} (the maximum error is 53 km s^{-1}).

Our main source of intensity-mean $\langle V \rangle$ magnitudes was the paper by Fernley *et al.* (1998), whose initial data were photometric observations taken onboard Hipparcos satellite and then reduced to the scale of V magnitudes of the Johnson system. Following Gould and Popovski (1998), for the remaining stars we used first the $\langle V \rangle$ values inferred using Layden's (1994) technique from the data by Bookmeyer *et al.* (1977), Schmidt (1991), Schmidt *et al.* (1995, 1996), and Layden (1993, 1997), whose photometric systems coincide with that of Fernley *et al.* (1998). In addition, we used the $\langle V \rangle$ magnitudes inferred by Layden *et al.* (1996) from the photometry by Clube and Dawe (1980b). We transformed the latter to the system of Fernley *et al.* (1998) using the following relation:

$$\langle V \rangle_{\mathrm{Fernley\ \textit{et al.}}} = (\langle V \rangle_{\mathrm{Clube\ and\ Dawe}} - 0.146)/0.983 \quad (2)$$

[see formula (6) of Gould and Popovski (1998)]. Thus, unlike Layden *et al.* (1996), we did not reduce the magnitudes of RR Lyraes to the system of Clube and Dawe (1980b), because Gould and Popowski (1998) found that it differs systematically not only from the magnitude scale of Bookmeyer *et al.* (1977), Schmidt (1991), Schmidt *et al.* (1995), and Schmidt and Seth (1996) [as noted by Layden *et al.* (1996)], but also from that of Fernley *et al.* (1998), whereas the magnitude scales of all above authors except Clube and Dawe (1980b) are in excellent agreement with each other. Finally, we left unchanged the $\langle V \rangle$ magnitudes of the remaining stars adopted from Layden (1994). Note that four of these stars have their $\langle V \rangle$ magnitudes determined via a careful recalibration of high-precision photographic photometry [see Layden (1997)], and those of 11 stars were determined by Layden (1994) by recomputing the intensity-mean photographic magnitudes whose photometric systems are rather unclear and must therefore be of not too high an accuracy. We included these stars into our sample, because they were used by Layden *et al.* (1996), who argue that the magnitudes of all RR Lyraes in their list have been reduced to the scale of photoelectric $\langle V \rangle$ magnitudes of the Johnson system. In any case, the number of these stars is too small (they make up about 4% of the entire sample) to distort the results substantially [see a discussion in Gould and Popowski (1998)].

Interstellar Extinction

It is well known that to correctly determine a photometric distance to a star, one must know not only its apparent and absolute magnitudes but also interstellar extinction in the photometric passband used (A_V in our case). We adopted $A_V = 3.1E_{(B-V)}$ values from Fernley *et al.* (1998), Layden (1994), and Layden *et al.* (1996), who determined most of them using HI absorption maps of Burstein and Heiles (1982) (for stars located more than 10° from the Galactic equator).

Proper Motions

The aim of this paper is to determine the kinematic parameters of RR(ab) Lyrae type stars based on the largest sample available and to compare the results obtained using proper motions adopted from different catalogs. That is why we tried to use all mass sources of absolute proper motions available to us. These are, first and foremost, the 4M catalog of positions and proper motions (Volchkov *et al.* 1992), including its reference catalog PPM (Roser *et al.* 1991). The second source is the recently released Hipparcos catalog, which contains the proper motions of about 118 000 stars. The proper motions in this catalog were determined from three-year-long high-precision position observations, and their standard errors (for the RR Lyraes included in the catalog) are on the average equal to 0.″002–0.″003/year. Our third source was the NPM1 catalog (Klemola *et al.* 1993;

Hanson 1994), which contains about 149 000 stars north of declination –23° (except for the region of low Galactic latitudes, $|b| < 10°$). The proper motions of stars in this catalog were determined in a frame referred to the positions of about 50 000 faint galaxies and are therefore completely independent of the proper motions of the Hipparcos and 4M catalogs.

Note, however, that the proper motions in the above catalogs have been determined using different techniques and can therefore differ systematically from each other. Therefore, before applying the statistical parallax technique to the combined sample, we must reduce all proper motions to a single system. As was noted above, we consider the Hipparcos catalog to define the most accurate proper motion system of the three catalogs, and we therefore used it as a reference to reduce the proper motions from the other two catalogs (NPM1 and 4M + PPM).

We reduced the proper motions adopted from the 4M and its reference catalog PPM to the Hipparcos system assuming that within small areas (of radius 2°) in the vicinity of each program star the systematic differences $\Delta\mu_\alpha = \mu_{\alpha(\text{Hipparcos})} - \mu_{\alpha(4M)}$ for the stars common to both catalogs depend linearly on coordinates α and δ:

$$\Delta\mu_\alpha = a_\alpha + b_\alpha\Delta\alpha + c_\alpha\Delta\delta, \quad (3)$$

$$\Delta\mu_\delta = \alpha_\delta + b_\delta\Delta\alpha + c_\delta\Delta\delta, \quad (4)$$

where $\Delta\alpha = \alpha(*) - \alpha(\text{st})$ and $\Delta\delta = \delta(*) - \delta(\text{st})$ are the differences of the coordinates of a star in the vicinity of the program star (*) and the program star proper (st). We determined parameters a_α, b_α, c_α, a_δ, b_δ, and c_δ using the least squares method based on all stars (common to the Hipparcos and 4M catalogs) within a circle of radius 2° centered on the program star (except for the program star itself even if it is included in the Hipparcos catalog). We then determined the reduced proper-motion components as follows:

$$\mu_{\alpha(\text{Red})} = \mu_{\alpha(4M)} + a_\alpha, \quad (5)$$

$$\mu_{\delta(\text{Red})} = \mu_{\delta(4M)} + a_\delta. \quad (6)$$

Unfortunately, this technique cannot be used to reduce the proper motions adopted from NPM1. The point is that this catalog contains only about 13 000 stars in common with the Hipparcos catalog of which less than 4000 (3760) are fainter than $V = 9^m.6$, the magnitude of the brightest RR Lyrae star in the NPM1 catalog. Using brighter stars to reduce the proper motions is undesirable because of a rather strong magnitude equation (no such problem exists in the case of the reduction of the proper motions from the 4M catalog, because its intersection with the Hipparcos list consists almost exclusively of the stars from the reference catalog PPM used to derive the proper motions of the 4M catalog). That is why we had to use a different technique to reduce the proper motions from the NPM1 catalog. We analyzed how the differences of proper-motion components of stars fainter than $V = 9^m.6$ and common to the Hipparcos and NPM1 catalogs depend on the position on the sky. We found (see Figs. 1, 2) μ_α to depend systematically on declination δ in the $\delta < -7°$ region and found no systematic dependence of μ_α on either coordinate and μ_δ on α. We therefore did not correct the NPM1 proper-motion components in right ascension and determined the corrections to μ_δ as arithmetic means of $\mu_{\delta(\text{Hipparcos})} - \mu_{\delta(\text{NPM1})}$ to the stars common to the NPM1 and Hipparcos catalogs, fainter than $V = 9^m.6$, and located within the declination interval from $\delta(*) - 0.25°$ to $\delta(*) + 0.25°$. We then determined the reduced values as follows:

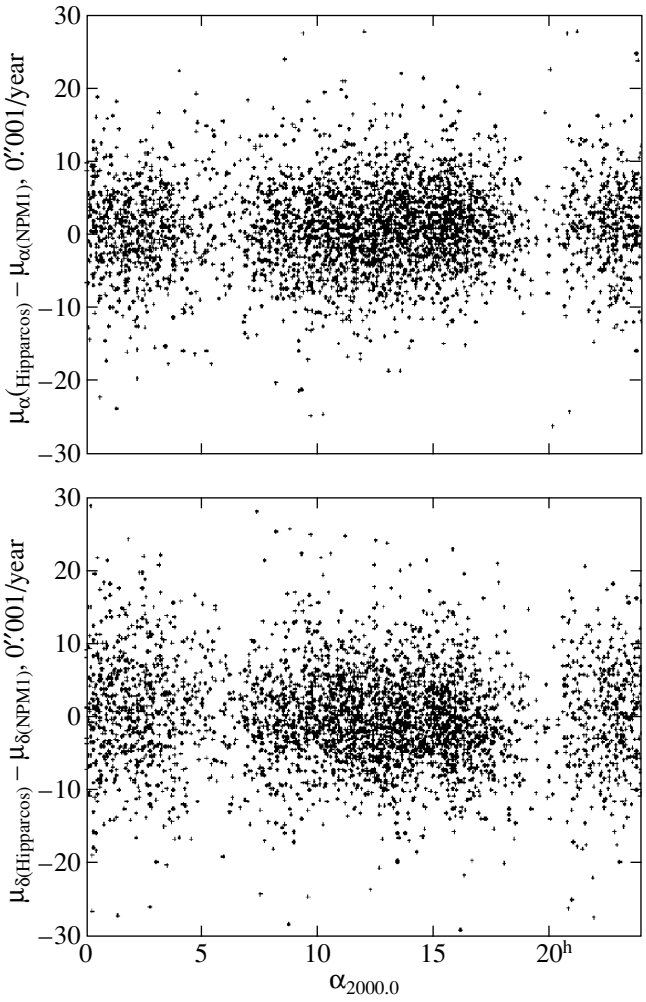

Fig. 1. The proper-motion component difference for stars fainter than $V = 9^m.6$ and common to the NPM1 and Hipparcos catalogs as a function of right ascension, $\alpha_{2000.0}$.

$$\mu_{\alpha(\text{Red})} = \mu_{\alpha(\text{NPM1})}, \quad (7)$$

$$\mu_{\delta(\text{Red})} = \mu_{\delta(\text{NPM1})} + \langle\mu_{\delta(\text{Hipparcos})} - \mu_{\delta(\text{NPM1})}\rangle. \quad (8)$$

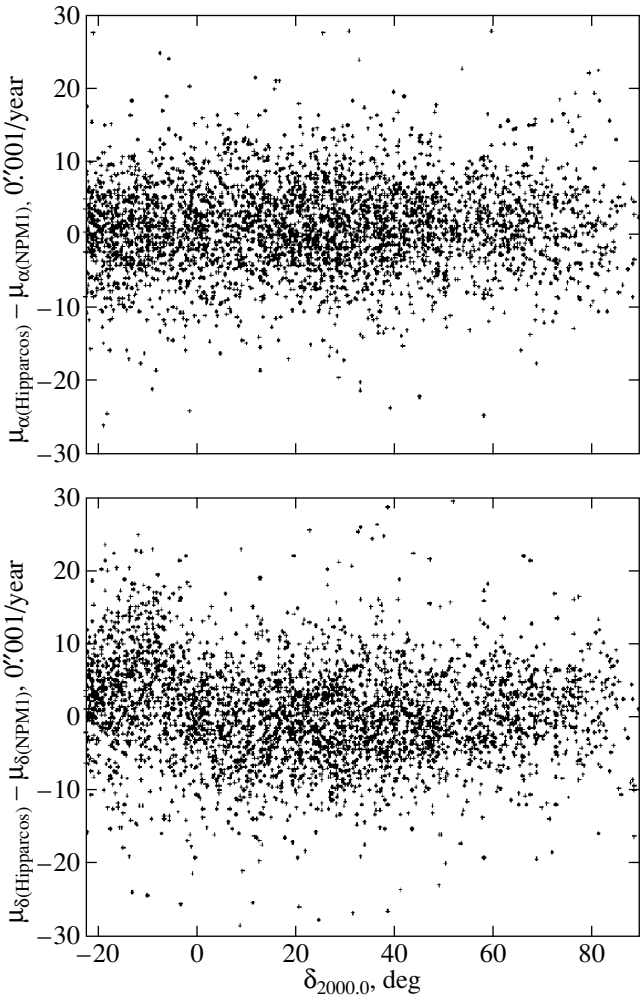

Fig. 2. The same as Fig. 1 but for declination $\delta_{2000.0}$.

Errors of Proper Motions

To apply statistical parallax technique, we must not only know the proper-motion components but also correctly estimate (in the statistical sense) the standard errors of the latter. Of all sources mentioned above, confident *individual* estimates of the standard errors of proper motions are available only for the stars in the Hipparcos catalog. At the same time, only mean errors averaged over the entire catalog are available for NPM1 and 4M. However, the random errors in the proper-motion components given by these catalogs can and are likely to be magnitude dependent, and the mean standard error can therefore depend on the magnitude distribution of the sample considered. And this distribution for the RR Lyraes in a certain catalog can differ substantially from the magnitude distribution for the entire catalog. Moreover, even if we adopt the standard errors of the proper motions quoted by the catalog authors, these errors can characterize *only the nonreduced* proper motions and in the general case tell nothing about the accuracy of the corresponding *reduced motions*. In view of the above, we estimated the standard errors of proper motions as follows. We determine only the mean (i.e., not individual) errors for each particular catalog averaged over the corresponding subset of our combined sample of RR Lyraes. To this end, we determine (using the stars common to the Hipparcos and the catalog considered) the root mean square differences of proper-motion components $\sigma(\mu_{\alpha(\mathrm{Hip})} - \mu_{\alpha(\mathrm{Cat})})$ and $\sigma(\mu_{\delta(\mathrm{Hip})} - \mu_{\delta(\mathrm{Cat})})$, and then assume that the proper-motion errors of the two catalogs are independent to obtain the following error estimates for the catalog under study:

$$\sigma(\mu_{\alpha(\mathrm{Cat})})^2 = \langle(\mu_{\alpha(\mathrm{Hipparcos})} - \mu_{\alpha(\mathrm{Cat})})^2\rangle - \langle\sigma(\mu_{\alpha(\mathrm{Hipparcos})})^2\rangle, \quad (9)$$

$$\sigma(\mu_{\delta(\mathrm{Cat})})^2 = \langle(\mu_{\delta(\mathrm{Hipparcos})} - \mu_{\delta(\mathrm{Cat})})^2\rangle - \langle\sigma(\mu_{\delta(\mathrm{Hipparcos})})^2\rangle. \quad (10)$$

Here we substituted $\sigma(\mu_{\alpha(\mathrm{Hipparcos})} - \mu_{\alpha(\mathrm{Cat})})^2$ and $\sigma(\mu_{\delta(\mathrm{Hipparcos})} - \mu_{\delta(\mathrm{Cat})})^2$ for $\langle(\mu_{\alpha(\mathrm{Hipparcos})} - \mu_{\alpha(\mathrm{Cat})})^2\rangle$ and $\langle(\mu_{\delta(\mathrm{Hipparcos})} - \mu_{\delta(\mathrm{Cat})})^2\rangle$, respectively, to allow for eventual zero offsets.

Table 1 gives the standard errors of (nonreduced and reduced) proper-motion components of the NPM1 and 4M catalogs. It is evident from this table that our reduction indeed improved the initial proper motions (the errors of reduced motions are lower than those of the nonreduced motions).

Averaged Proper Motions

We seem to have all grounds to believe that the reduced proper motions of stars common to the 4M and NPM1 catalogs are independent of each other and of the proper motions of the Hipparcos catalog. We therefore considered it possible to determine the weighted averages of μ_α and μ_δ and the corresponding covariance matrix for the stars with proper motions available from several sources. We computed the resulting covariance matrix taking into account the correlation between the errors of μ_α and μ_δ given in the Hipparcos catalog and assuming the corresponding correlation coefficients to be zero for the other two catalogs. As a result, we obtained a combined sample of RR Lyraes containing a total of 262 stars.

INITIAL DISTANCES: DISK AND HALO STARS

Layden (1995) and Layden *et al.* (1996) showed that the kinematic population of RR Lyraes in our Galaxy breaks conspicuously into two subclasses: halo and thick-disk stars. At first approximation, the two subclasses can be separated by the metallicity value [Fe/H] = –1.0: the overwhelming majority of more metal-deficient stars exhibit a kinematic behavior typical of the objects of the Galactic halo, whereas the kinematics of

more metal-rich stars is more similar to that of the Galactic disk.

Following Layden *et al.* (1996), we subdivided our sample into the halo and thick-disk subsamples in three ways using three definitions of the disk and halo (by metallicity and velocity components). To this end, we computed velocity components U, V, and W in the Cartesian Galactic system with allowance for the solar motion relative to the Local Standard of Rest (+9, +12, and +7) km s^{-1} (Mihalas and Binney 1981) and the rotation of the Sun around the Galactic center [220 km s^{-1}, Kerr and Lynden-Bell (1986)], and transformed them into the velocity components in the Galactocentric cylindrical system ($V_R V_\theta V_Z$). To transform the proper motions into the space-velocity components, we used the provisional star distances computed using the absolute-magnitude calibration $\langle M_V\rangle$(RR) – [Fe/H] of Carney *et al.* (1992):

$$\langle M_V\rangle(\mathrm{RR}) = 1.01 + 0.15[\mathrm{Fe/H}]. \qquad (11)$$

We then followed the procedure described in Table 2, which gives modified definitions of the halo and disk subsamples from Layden *et al.* (1996) (see Table 3 in that paper). (We consider RW Col and IK Hya to be halo stars based on their space velocities, although they formally match D-1 and D-3 criteria of the paper mentioned above, and thus add them to AO Peg and FU Vir as exceptions to the general rule.)

Final Sample

Our final sample of RR Lyrae stars consists of 262 stars for which all five types of initial data, proper motions, radial velocities, metallicities, interstellar extinction, and *photoelectric or CCD* intensity-mean $\langle V\rangle$ magnitudes, are available. Our list thus contains substantially more stars than any other sample previously used to this end. Moreover, the proper motions from the 4M catalog allowed us to do without *statistically* absolutized proper motions.

Table 3[1] gives the list of the 262 RR Lyraes used in this paper together with their parameters. The latter include the accurate equatorial coordinates for the epoch and equinox of J2000.0; proper-motion components in right ascension and declination adopted from the Hipparcos (with the corresponding standard errors and the correlation coefficient), 4M + PPM, and NPM1 catalogs; the 4M + PPM and NPM1 proper-motion components reduced to the Hipparcos system; intensity-mean $\langle V\rangle$ magnitudes; [Fe/H]; and mean radial velocities and their standard errors. For three stars AE Dra, BD Dra, and BK Eri, we adopted the NPM1 proper motions refined by Layden *et al.* (1996). Finally, we excluded from our sample a number of stars that are classified as RR Lyraes in the GCVS, but must actually be of different variability types [see comments to Table 3 of this paper and to Table 1 of Fernley *et al.* (1998)].

[1] Table 3 is published in electronic form only and is available from the Strasbourg Data Center at ftp: cdsarc.u-strasbg.fr/pub/cats/J (130.79.128.5) or http://cdsweb.u-strasbg.fr/pub/cats/J.

Table 1. Standard errors of the proper motions estimated from stars common with the Hipparcos catalog

Catalog	Errors of nonreduced proper motions, 0″.001/year		Errors of reduced proper motions, 0″.001/year	
	$\sigma(\mu_\alpha)$	$\sigma(\mu_\delta)$	$\sigma(\mu_{\alpha(\mathrm{Red})})$	$\sigma(\mu_{\delta(\mathrm{Red})})$
PPM	6.34	5.97	4.62	5.35
4M	5.95	7.40	5.15	5.92
NPM1	5.40	7.15	5.40	6.30

Table 2. Definitions of disk and halo RR Lyrae subsamples

Definition	Description
Disk-1	All stars with $V_\theta > -400 \cdot$ [Fe/H] – 300 km s^{-1} except AO Peg, FU Vir, RW Col, and IK Hya
Halo-1	All other stars
Disk-2	All stars with [Fe/H] ≥ –1.0 V_θ > 80 km s^{-1} except AO Peg
Halo-2	All other stars
Disk-3	All stars of the Disk-1sample and the stars with $\lvert V_R\rvert$ < 100 km s^{-1}, V_θ > 80 km s^{-1}, $\lvert V_Z\rvert$ < 60 km s^{-1}, $\lvert Z\rvert$ < 1 kpc, and [Fe/H] > –1.6
Halo-3	All other stars

RESULTS

We first applied the statistical parallax technique described above to nine samples of Galactic halo RR Lyraes that differ from each other by the source of proper motions (Hipparcos, NPM1, and 4M + PPM) and the method of separation of halo and thick-disk stars. Table 4 gives the resulting parameters for the RR Lyrae samples thus defined. Column 1 gives the name of the halo sample according to the definition in Table 2; column 2, the source (catalog) of proper motions; column 3, the number of stars in the sample; column 4, the mean [Fe/H] averaged over the sample; columns 5 to 7, the mean velocity components, U_0, V_0, and W_0 (in the direction to the Galactic center, Galactic rotation, and North Galactic Pole, respectively); columns 8 to 10, the corresponding diagonal components of the velocity dispersion tensor, σ_U, σ_V, and σ_W [we assume the nondiagonal components to be equal to zero; see Layden *et al.* (1996)]; column 11, the inferred correction to the initial mean absolute magnitude $\langle M_V\rangle$ given by formula (11); column 12, the mean absolute magnitude $\langle M_V\rangle$ at [Fe/H] = –1.60; and column 13, the corresponding LMC distance modulus. Columns 5 to 13 also give the standard errors of the corresponding parameters for each sample. The results obtained for different samples can be seen to agree excellently with each other: the inferred parameters are virtually independent of both the adopted criterion of halo and disk separation [this result agrees with that of Layden *et al.* (1996)] and the

Table 4. Kinematic parameters of the subsystem of halo RR Lyraes inferred using nonreduced proper motions

Sample	Catalog	N	$\langle$[Fe/H]$\rangle$	U_0, km s^{-1}	V_0, km s^{-1}	W_0, km s^{-1}	σ_U, km s^{-1}	σ_V, km s^{-1}	σ_W, km s^{-1}	$\Delta\langle M_V\rangle$	$\langle M_V\rangle$ (–1.60)	DM (LMC)
Halo-1	Hipparcos	100	–1.568	–19	–217	–8	167	106	98	–0.08	+0.69	18.30
				±17	±14	±10	±15	±9	±9	±0.14	±0.14	±0.15
Halo-2	Hipparcos	101	–1.558	–17	–213	–9	166	109	97	–0.07	+0.70	18.29
				±17	±14	±10	±15	±9	±8	±0.14	±0.14	±0.15
Halo-3	Hipparcos	95	–1.572	–18	–222	–9	171	106	100	–0.08	+0.69	18.30
				±18	±15	±10	±16	±10	±9	±0.15	±0.15	±0.16
Halo-1	4M + PPM	185	–1.592	–4	–206	–17	170	104	97	+0.02	+0.79	18.20
				±13	±10	±8	±12	±7	±7	±0.11	±0.11	±0.12
Halo-2	4M + PPM	196	–1.564	–4	–198	–18	165	107	95	+0.02	+0.79	18.20
				±12	±10	±7	±11	±7	±7	±0.11	±0.11	±0.12
Halo-3	4M + PPM	179	–1.600	–5	–209	–18	172	105	98	+0.03	+0.80	18.19
				±13	±11	±8	±12	±8	±7	±0.12	±0.12	±0.13
Halo-1	NPM1	134	–1.593	–8	–204	–13	159	101	87	+0.04	+0.81	18.18
				±14	±13	±8	±13	±9	±7	±0.13	±0.13	±0.14
Halo-2	NPM1	139	–1.589	–9	–195	–14	157	109	86	+0.04	+0.81	18.18
				±14	±13	±8	±13	±9	±7	±0.13	±0.13	±0.14
Halo-3	NPM1	184	–1.593	–7	–207	–13	160	100	89	+0.05	+0.82	18.17
				±15	±13	±8	±13	±9	±8	±0.14	±0.14	±0.15

proper-motion source used (which we consider to be a fact of greater or at least equal importance).

We then applied the statistical parallax technique to the six RR Lyrae samples with reduced proper motions [two sources (4M + PPM and NPM1 catalogs) and three halo criteria (the proper motions from the Hipparcos catalog)], naturally, were not reduced. The corresponding results are summarized in Table 5, which has the same layout as Table 4. Again, the inferred parameters can be seen to agree well with those based on Hipparcos data. Moreover, as one would expect, the agreement is even better than in the case when nonreduced proper motions were used. This result serves to justify the averaging of proper motions from the three catalogs considered (naturally, with weights inversely proportional to the squared errors of the corresponding values) in order to build a combined RR Lyrae sample consisting of a total of 262 stars with absolute proper motions on the Hipparcos system. We subdivided this sample, too, into halo and thick-disk subsamples using three criteria from Layden *et al.* (1996) in a slightly modified form (see Table 2). We then applied statistical parallax technique to this combined sample to infer three (most accurate) sets of parameter values for both the halo and the thick-disk RR Lyrae populations. The results thus obtained are given in Table 6, whose layout, too, is identical to that of Table 4, except for the second part, which gives the results for the thick-disk RR Lyrae samples: the corresponding absolute magnitudes $\langle M_V\rangle$ refer not to [Fe/H] = –1.60 but to the mean $\langle$[Fe/H]$\rangle$ for the corresponding sample as given in column 3. Based on the same reasons as Layden *et al.* (1996), we consider the results obtained using Halo-3 sample to be most representative of the halo population. However, we prefer the Halo-2 sample solution as a more justified option in the case of the thick-disk population, because the corresponding sample is least "contaminated" by halo stars. We thus finally adopt $(U_0, V_0, W_0) = (-9 \pm 12, -214 \pm 10, -16 \pm 7)$ km s^{-1}, $(\sigma_U, \sigma_V, \sigma_W) = (164 \pm 11, 105 \pm 7, 95 \pm 7)$ km s^{-1}, and $\langle M_V\rangle = 0.77 \pm 0.10$ for halo objects (201 stars) and $(U_0, V_0, W_0) = (-16 \pm 8, -41 \pm 67, -18 \pm 5)$ km s^{-1}, $(\sigma_U, \sigma_V, \sigma_W) = (53 \pm 9, 42 \pm 8, 26 \pm 5)$ km s^{-1}, and $\langle M_V\rangle = +1.11 \pm 0.28$ for thick-disk objects (46 stars), which agrees very well with the results of Layden *et al.* (1996).

$\langle M_V\rangle$([Fe/H]) RELATION

Our list is superior in size to all other RR Lyrae samples previously used and it must therefore allow the statistical parallax technique to be used for the first time to obtain confident conclusions about the behavior of the heavy-element abundance dependence of RR Lyrae luminosities. The previous such attempt by Layden *et al.* (1996) failed: these authors found $\Delta\langle M_V\rangle/\Delta$[Fe/H] = $+0.09 \pm 0.38$. We subdivided the Halo-2 sample from Table 6 into four approximately equal subsamples with mean metallicities $\langle$[Fe/H]$\rangle_1 = -2.02$, $\langle$[Fe/H]$\rangle_2 = -1.53$, $\langle$[Fe/H]$\rangle_3 = -1.43$, and $\langle$[Fe/H]$\rangle_4 = -1.17$, and applied the statistical parallax technique to each of them. The results are summarized in Table 7. We thus obtained four halo RR Lyrae absolute-magnitude estimates at four metallicity values. We now add to them the $\langle M_V\rangle$

Table 5. Kinematic parameters of the subsystem of halo RR Lyraes inferred using proper motions reduced to the Hipparcos system

Sample	Catalog;	N	⟨[Fe/H]⟩	U_0, km s^{-1}	V_0, km s^{-1}	W_0, km s^{-1}	σ_U, km s^{-1}	σ_V, km s^{-1}	σ_W, km s^{-1}	$\Delta\langle M_V\rangle$	$\langle M_V\rangle$ (–1.60)	DM (LMC)
Halo-1	4M + PPM	187	–1.588	–10	–206	–16	166	105	97	0.00	+0.77	18.22
				±13	±10	±7	±11	±7	±7	±0.11	±0.11	±0.12
Halo-2	4M + PPM	194	–1.573	–9	–199	–18	164	109	96	+0.00	+0.77	18.22
				±12	±10	±7	±11	±7	±7	±0.11	±0.11	±0.12
Halo-3	4M + PPM	176	–1.605	–10	–213	–17	171	105	100	0.00	+0.77	18.22
				±13	±11	±8	±12	±7	±7	±0.11	±0.11	±0.12
Halo-1	NPM1	136	–1.596	–7	–204	–16	158	105	87	+0.04	+0.81	18.18
				±14	±13	±8	±13	±9	±7	±0.13	±0.13	±0.14
Halo-2	NPM1	138	–1.593	–6	–197	–16	156	110	86	+0.06	+0.83	18.16
				±14	±13	±8	±13	±9	±7	±0.13	±0.13	±0.14
Halo-3	NPM1	130	–1.610	–6	–208	–16	161	105	89	+0.04	+0.81	18.18
				±15	±13	±8	±13	±9	±8	±0.14	±0.14	±0.15

value obtained for thick-disk RR Lyraes (see solution Disk-2 in Table 6) to make up a total of five data points on the [Fe/H]–$\langle M_V\rangle$ diagram (see Table 7 and Fig. 3), which yield the following least-squares fit:

$$\langle M_V\rangle = (0.76 \pm 0.12) + (0.26 \pm 0.26)\cdot([\mathrm{Fe/H}] + 1.6), \quad (12)$$

or

$$\langle M_V\rangle = 1.17 \pm 0.26 \cdot [\mathrm{Fe/H}]. \quad (13)$$

This result is, on the whole, consistent with formula (11) derived for field RR Lyraes using the Baade–Wesseling technique (Carney *et al.* 1992). We inferred the slope of the [Fe/H]($\langle M_V\rangle$) relation one and a half times more accurately than Layden *et al.* (1996), although, unfortunately, the error remains too high.

DISTANCE SCALE

As was noted above, the mean absolute magnitude of RR Lyrae type stars forms one of the bases of the distance scale in the Universe and can be used, in particular, to measure the distances to the LMC and the Galactic center, because both objects contain RR Lyraes.

The Distance to the LMC

If applied to photometric observations of RR Lyraes in seven globular clusters in the LMC (Walker 1992), our calibration of the zero point of the [Fe/H]($\langle M_V\rangle$) relation (Halo-2 in Table 6: $\langle M_V\rangle([\mathrm{Fe/H}] = -1.60) = +0.77 \pm 0.10$) yields an LMC distance modulus of $DM_{\mathrm{LMC}} = 18.22 \pm 0.11$, which is in excellent agreement with the result of Layden *et al.* (1996) and the value of 18.25 ± 0.05 (Berdnikov *et al.* 1996) obtained using the period-luminosity relation for classical Cepheids (in terms of the short distance scale).

The Distance to the Galactic Center

Layden *et al.* (1996) applied their calibration of the [Fe/H]($\langle M_V\rangle$) relationship to the data of Walker and Mack (1988) to infer a distance of $R_0 = 7.6 \pm 0.6$ kpc to the Galactic center. Our $\langle M_V\rangle$ is $0^m.06$ fainter than that obtained by Layden *et al.* (1996) and somewhat more accurate, and we therefore find $R_0 = 7.4 \pm 0.5$ kpc, which agrees excellently with the estimates inferred from (1) the rotation-curve analysis of classical Cepheids based on the *short* distance scale [$R_0 = 7.1 \pm 0.5$ kpc (Dambis *et al.* 1995)]; (2) the rotation-curve analysis of a more extensive sample of young Galactic objects, also based on the short distance scale [$R_0 = 7.3 \pm 0.3$ kpc (Glushkova *et al.* (1998)]; and (3) the only available

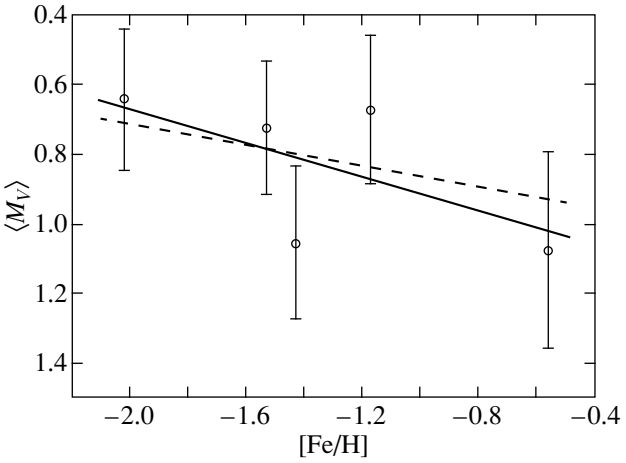

Fig. 3. Metallicity ([Fe/H]) dependence of the mean absolute magnitude $\langle M_V\rangle$ of RR Lyraes. Dots are the values inferred using statistical parallax technique. Solid and dashed lines are the relation of Carney *et al.* (1992) [formula (11)] and linear least squares fit to our results [formula (13)], respectively.

Table 6. Kinematic parameters of the subsystem of halo RR Lyraes inferred using proper motions reduced to the Hipparcos system and averaged over three catalogs

Sample	N	⟨[Fe/H]⟩	U_0, km s^{-1}	V_0, km s^{-1}	W_0, km s^{-1}	σ_U, km s^{-1}	σ_V, km s^{-1}	σ_W, km s^{-1}	$\Delta\langle M_V\rangle$	$\langle M_V\rangle$ (–1.60)	DM (LMC)
Halo-1	211	–1.574	–9	–208	–15	161	106	93	–0.01	+0.76	18.23
			±11	±10	±7	±10	±7	±6	±0.10	±0.10	±0.11
Halo-2	216	–1.565	–8	–202	–15	158	109	92	+0.01	+0.78	18.21
			±11	±10	±7	±10	±7	±6	±0.10	±0.10	±0.11
Halo-3	201	–1.585	–9	–214	–16	164	105	95	0.00	+0.77	18.22
			±12	±10	±7	±11	±7	±7	±0.10	±0.10	±0.11
Sample	N	⟨[Fe/H]⟩	U_0, km s^{-1}	V_0, km s^{-1}	W_0, km s^{-1}	σ_U, km s^{-1}	σ_V, km s^{-1}	σ_W, km s^{-1}	$\Delta\langle M_V\rangle$	$\langle M_V\rangle$(⟨[Fe/H]⟩)	
Disk-1	51	–0.622	–12	–34	–16	47	35	24	+0.40	+1.35	
			±7	±6	±4	±8	±6	±5	±0.28	±0.28	
Disk-2	46	–0.560	–16	–41	–18	53	42	26	+0.16	+1.11	
			±8	±7	±5	±9	±8	±5	±0.28	±0.28	
Disk-3	61	–0.740	–12	–49	–17	54	47	26	–0.02	+0.92	
			±7	±7	±4	±9	±7	±5	±0.23	±0.24	

Table 7. Kinematic parameters of the subsystems of halo RR Lyraes with different metallicities (subsamples of Halo-2 sample) inferred using proper motions reduced to the Hipparcos system and averaged over three catalogs

min([Fe/H])	max([Fe/H])	⟨[Fe/H]⟩	N	U_0, km s^{-1}	V_0, km s^{-1}	W_0, km s^{-1}	σ_U, km s^{-1}	σ_V, km s^{-1}	σ_W, km s^{-1}	$\Delta\langle M_V\rangle$	$\langle M_V\rangle$
–2.84	–1.80	–2.020	46	–29	–228	+4	154	130	89	–0.07	+0.64
				±21	±23	±13	±20	±16	±11	±0.20	±0.20
–1.79	–1.52	–1.526	55	–25	–210	–33	174	107	96	–0.05	+0.72
				±24	±18	±13	±20	±13	±12	±0.19	±0.19
–1.51	–1.33	–1.434	48	+12	–201	–33	158	86	83	+0.26	+1.05
				±23	±19	±13	±21	±11	±12	±0.22	±0.22
–1.32	–0.80	–1.172	57	+9	–173	0	141	103	89	–0.16	+0.67
				±19	±18	±13	±19	±13	±11	±0.21	±0.21

direct estimate based on the measurement of the proper motions of an H_2O maser [$R_0 = 7.2 \pm 1.3$ kpc (Reid 1993)].

CONCLUSION

The application of the statistical-parallax technique to the largest sample of RR Lyraes with known kinematic parameters (a total of 262 stars, i.e., a 25% increase over the largest of such samples used so far) leads us to the following conclusions:

(1) Our analysis provides further and more precise evidence in favor of the short distance scale: the implied LMC distance modulus and the distance to the Galactic center are equal to 18.22 ± 0.11 and 7.4 ± 0.5 kpc, respectively.

(2) The conclusion about the short distance scale is independent of the proper-motion source used.

(3) The inferred slope of the [Fe/H]($\langle M_V\rangle$) relation is close to that determined using the Baade–Wesselink method.

ACKNOWLEDGMENTS

We are grateful to the referee, A.A.Tokovinin, for a number of useful comments. This research has made use of NASA's Astrophysics Data System Abstract Service. The work was supported by the Russian Foundation for Basic Research (grants nos. 98-02-16107, 99-02-17842, and 00-02-17804), the Council for the Support of Leading Science Schools (grant no. 00-15-96627), and "Astronomy" State Science and Technology Program.

REFERENCES

1. L. N. Berdnikov, O. V. Vozyakova, and A. K. Dambis, Pis'ma Astron. Zh. **22**, 936 (1996) [Astron. Lett. **22**, 838 (1996)].
2. B. B. Bookmeyer, W. S. Fitch, T. A. Lee, *et al.*, Rev. Mex. Astron. Astrofis. **2**, 235 (1977).
3. D. Burstein and C. Heiles, Astron. J. **87**, 1165 (1982).
4. B. W. Carney, J. Storm, and R. V. Jones, Astrophys. J. **386**, 663 (1992).

5. S. V. Clube and J. A. Dawe, Mon. Not. R. Astron. Soc. **190**, 575 (1980a).
6. S. V. Clube and J. A. Dawe, Mon. Not. R. Astron. Soc. **190**, 591 (1980b).
7. A. K. Dambis, A. M. Mel'nik, and A. S. Rastorguev, Pis'ma Astron. Zh. **21**, 331 (1995) [Astron. Lett. **21**, 291 (1995)].
8. J. Fernley and T. G. Barnes, Astron. Astrophys., Suppl. Ser. **125**, 313 (1997).
9. J. Fernley, T. G. Barnes, I. Skillen, *et al.*, Astron. Astrophys. **330**, 515 (1998).
10. E. V. Glushkova, A. K. Dambis, A. M. Mel'nik, and A. S. Rastorguev, Astron. Astrophys. **329**, 514 (1998).
11. A. Gould and P. Popowski, Astrophys. J. **508**, 844 (1998).
12. R. B. Hanson, *Lick Proper Motion Program: NPM1 Catalog—Documentation for the Computer-Readable Version*, National Space Science Data Center Document No. NSSDC/WDC-A-R\&S 93-41 (1994).
13. S. L. Hawley, W. H. Jeffreys, T. G. Barnes III, and L. Wan, Astrophys. J. **302**, 626 (1986).
14. A. Heck and J. M. Lakaye, Mon. Not. R. Astron. Soc. **184**, 17 (1978).
15. M. K. Hemenway, Astron. J. **80**, 199 (1975).
16. L. J. Kerr and D. Lynden-Bell, Mon. Not. R. Astron. Soc. **221**, 1023 (1986).
17. A. R. Klemola, R. B. Hanson, and B. F. Jones, *Lick Proper Motion Program: NPM1 Catalog*, National Space Science Data Center—Astronomical Data Center Catalog No. A1199 (1993).
18. A. C. Layden, PhD Dissertation (Yale University, 1993).
19. A. C. Layden, Astron. J. **108**, 1016 (1994).
20. A. C. Layden, Astron. J. **110**, 2288 (1995).
21. A. C. Layden, Publ. Astron. Soc. Pac. **109**, 524 (1997).
22. A. C. Layden, R. B. Hanson, S. L. Hawley, *et al.*, Astron. J. **112**, 2110 (1996).
23. D. Mihalas and J. Binney, *Galactic Astronomy* (Freedman, San Francisco, 1981).
24. C. A. Murray, *Vectorial Astrometry* (Adam Hilger, Bristol, 1983; Naukova Dumka, Kiev, 1986).
25. J. A. Nedler and R. Mead, Comput. J. **7**, 308 (1965).
26. E. D. Pavlovskaya, Perem. Zvezdy **9**, 349 (1953).
27. P. Popowski and A. Gould, Astrophys. J. **506**, 259 (1998a).
28. P. Popowski and A. Gould, Astrophys. J. **506**, 271 (1998b).
29. M. J. Reid, Annu. Rev. Astron. Astrophys. **31**, 345 (1993).
30. J. L. Rigal, Bull. Astron. **22**, 171 (1958).
31. S. Roser, U. Bastian, V. V. Nesterov, *et al.*, *PPM: Star Catalogue: Positions and Proper Motions* (Astronomisches Rechen Inst., Heidelberg, 1991).
32. A. Sandage, Astrophys. J. **350**, 603 (1990).
33. E. G. Schmidt, Astron. J. **102**, 1766 (1991).
34. E. G. Schmidt and A. Seth, Astron. J. **112**, 2769 (1996).
35. E. G. Schmidt, J. R. Chab, and D. E. Reiswig, Astron. J. **109**, 1239 (1995).
36. E. Solano, R. Garrido, J. Fernley, and T. G. Barnes, Astron. Astrophys., Suppl. Ser. **125**, 321 (1997).
37. P. Strugnell, N. Reid, and C. A. Murray, Mon. Not. R. Astron. Soc. **220**, 413 (1986).
38. T. Tsujimoto, M. Miyamoto, and Y. Yoshii, Astrophys. J. Lett. **492**, L79 (1998).
39. G. van Herk, Bull. Astron. Inst. Netherlands **18**, 71 (1965).
40. A. A. Volchkov, A. V. Kuz'min, and V. V. Nesterov, in *On the Four-Million Catalog of Stars*, Ed. by A. P. Gulyaev and V. V. Nesterov (Mosk. Gos. Univ., Moscow, 1992), p. 67.
41. A. R. Walker, Astrophys. J. Lett. **390**, L81 (1992).
42. A. R. Walker and P. Mack, Astron. J. **96**, 872 (1988).
43. R. Zinn and M. J. West, Astrophys. J., Suppl. Ser. **55**, 45 (1984).
44. ESA, *The Hipparcos and Tycho Catalogues* (ESA, Nordwijk, 1997), ESA SP-1200.

Translated by A. Dambis

Astronomy Letters, Vol. 27, No. 2, 2001, pp. 118–123. Translated from Pis'ma v Astronomicheskiĭ Zhurnal, Vol. 27, No. 2, 2001, pp. 144–149.

Oscillations of Flux Tube Bundles and the Structure of Sunspot Magnetic Fields

E. Yu. Nagovitsyna and Yu. A. Nagovitsyn*

Pulkovo Observatory, Russian Academy of Sciences, Pulkovskoe sh. 65, St. Petersburg, 196140 Russia

Received August 18, 1999; in final form, March 22, 2000

Abstract—Observational aspects of the previously found quasi-hourly oscillations of magnetic fragments in sunspot polar coordinates are investigated. The orientation of the oscillations is shown to be azimuthally anisotropic, with their amplitude reaching a maximum in penumbra at a distance of ~0.8 sunspot radius (the maximum amplitude is estimated to be 3700 km). Based on the detected deviations of the oscillations from the radial direction, we numerically simulate the horizontal configuration of field lines in the region of the major spots in bipolar groups. © *2001 MAIK "Nauka/Interperiodica".*

Key words: *Sun, active regions, magnetic field, oscillations*

INTRODUCTION

"Until recently a sunspot has been considered as a single homogeneous structure; at best, a distinction has been made between umbra and penumbra, although evidence for sunspot inhomogeneity has been known for more than a hundred years … . Available data give the following picture, which, in our view, is most likely: a sunspot is a collection of ropes combined into a single tube, which, however, is not isolated from convection—convection exists inside it, in its lower parts" (Obridko 1985).

The objects under study are represented here by pores and dark features inside sunspots—fragments of white-light images for active regions with horizontal sizes of ~10^3 km and a brightness of less than 0.8 of the surrounding background. The lifetime of such fragments ranges from several hours to several days, and their material carriers are local magnetic-field nonuniformities—flux tube bundles with characteristic magnetic fluxes of ~10^{19}–10^{20} M (Keppens and Martinez 1996). The bundles may belong to an intermediate type of a strong magnetic field between developed sunspots with penumbrae (a scale of ~10^4 km) and elementary ropes (~10^2 km).

While studying the horizontal motion of magnetic fragments, we found that it could be more accurately represented as a sum of a linear trend and quasi-periodic oscillations. The slow trend with a mean velocity of ~100 m s^{-1} is probably attributable to supergranulation convection (Nagovitsyna and Nagovitsyn 1999, 1998a). The component of the dynamics that remains after subtracting the trend is associated with quasi-hourly spatial tube oscillations with characteristic periods of 40–100 min (Mashnich and Bashkirtsev 1999). This phenomenon was first observed by Bashkirtsev *et al.* (1983) in longitudinal and torsional prominence oscillations. Subsequently, it was observed by Gopasyuk (1985) in torsional oscillations of sunspots and by Demchenko *et al.* (1985) in variations of their area. Approximately at the same time, we detected and began to study this phenomenon in latitudinal and longitudinal sunspot oscillations and in radial and azimuthal fragment oscillations. On the one hand, fragment oscillations are not synchronized and reflect asymmetric and nonuniform tube variations, and, on the other hand, the general component corresponding to the oscillations of the tube as a whole can be revealed by averaging (Nagovitsyna 1990).

Based on the observational data used here, we previously investigated the quasi-periodic dynamics of fragments by a harmonic analysis (Nagovitsyna and Nagovitsyn 1998b). Here, we consider it in a nonharmonic approximation by analyzing only spatial parameters, the oscillation amplitude and orientation on the solar surface.

OBSERVATIONS AND DATA REDUCTION

Our observations with the special Pulkovo Observatory photoheliograph on June 24, 1989 (06:30–12:10 UT) yielded a 340-min-long series of photoheliograms taken at 15-min intervals on 22 FU-5 ORWO (9×12 cm^2) plates. Each plate contains three images of the full solar disk at 2-min intervals. We measured the plates with a

* E-mail address for contacts: nag@gao.spb.ru

universal two-coordinate microscope (UIM-23). The objects' heliographic latitudes and longitudes were determined with an accuracy of 0.05° (~600 km) using the HELICOR computer-based technique (Nagovitsyna and Nagovitsyn 1996). This technique reveals and corrects the image distortions produced by several factors: discrepancy of equatorial mounting, differential atmospheric refraction, lens distortion, instrumental errors of the optical system (plate tilt, tube flexure, etc.), and solar-limb distortions (irradiation, differential extinction, image tremor).

To study the patterns of motion, we use simplexes—bipolar and unipolar groups with a simple magnetic configuration; the major spots are well developed, have penumbrae, and generally occupy more than 75% of the group area. Our observational data cover the heliographic coordinates of 19 sunspot centers in 12 groups and 130 fragments at 22 instants of time for each plate of the series. The main problem is to identify fragments on plates: fragments can appear and disappear repeatedly, changing their apparent brightness. We first identified 143 fragments. However, an analysis of their coordinates revealed 13 cases of characteristic jumps suggesting the disappearance of one fragment and the appearance of another fragment nearby.

We transformed the heliographic coordinates of fragments to polar r and θ coordinates relative to the sunspot centers. Pointing at the optical center of a sunspot as at the centroid of its umbra, a customary procedure for observers, is more accurate than might seem at first glance. Besides, the dispersion of the center coordinates contributes equally to the dispersions of the relative coordinates of all fragments: it raises the lower dispersion level, but does not form its functional dependence on radial distance.

The fragment azimuth was associated with an absolute coordinate system:

$$\begin{aligned} \theta = 0^\circ &\longrightarrow \text{west (W)}, \quad \theta = 90^\circ \longrightarrow \text{north (N)}, \\ \theta = 180^\circ &\longrightarrow \text{east (E)}, \\ \theta = 270^\circ &\longrightarrow \text{south (S)}. \end{aligned} \tag{1}$$

This association enables us to properly allow for asymmetric effects in sunspots, for example, the east–west (E–W) asymmetry of the opposite sign in the preceding (p) and following (f) sunspot of a bipolar group attributable to tube curvature above the photosphere (Nagovitsyna and Nagovitsyn 1999, 1998a), or the latitude–longitude asymmetry that shows up in a meridional (N–S) flattening of sunspots.

The mean radial distance $\bar{r}$ of fragments was normalized to the radius R of a sunspot with penumbra, which we define in the symmetric approximation as the radius of a circle equivalent in area to the observed sunspot:

$$\rho = \frac{\bar{r}}{R}, \quad \bar{r} = \frac{1}{n}\sum_{i=1}^{n} r_i, \quad R\ (\text{km}) = 984\sqrt{S\ (\text{m.s.h.})},$$

where S (m.s.h.) is the area of the spot with penumbra, in millionths of the solar hemisphere. The areas were measured on plates with the best images and were assumed to have been constant during the observations. Note that an error in the measured S even by 20% introduces an error of $\Delta\rho = 0.087\rho$ in the radial distance of a fragment, which is equal to $<0.03R$, $<0.09R$, and $\leq 0.2R$ in the sunspot umbra, penumbra, and the pore zone, respectively, i.e., an order of magnitude smaller than the sizes of structural sunspot regions. The amount of available data allows a parallel analysis and comparison of the results for three independent samples: the N-hemisphere p sunspots, 41 fragments, six sunspots, and the mean $R = 18\,600$ km; the S-hemisphere p sunspots, 49 fragments, six sunspots, and the mean $R = 14\,300$ km; and the f spots of both hemispheres, 40 fragments, seven sunspots, and the mean $R = 13\,700$ km.

The linear trend of a fragment can be estimated using the most probable radial (V_r) and azimuthal (V_a) velocities by least squares from sequences of fragment r_i and θ_i coordinates at times t_i. The coordinate residuals after trend subtraction,

$$\begin{aligned} \Delta r_i &= r_i - V_r t_i - r_0, \quad \Delta\theta_i = \theta_i - V_\theta t_i - \theta_0, \\ \Delta a_i &= \frac{\pi}{180}\bar{r}\Delta\vartheta_i, \quad i = 1\text{–}22, \end{aligned} \tag{2}$$

contain information about the oscillations of interest.

OSCILLATION AMPLITUDE

The dispersion of the fragment coordinates characterizes the amplitude of their horizontal oscillations. The dispersion (or, more precisely, the unbiased standard deviation) of the coordinates is given by the standard relations

$$\sigma = \sqrt{\sigma_r^2 + \sigma_a^2}, \quad \sigma_r^2 = \frac{1}{n-1}\sum_{i=1}^{n}\Delta r_i^2,$$

$$\sigma_a^2 = \frac{1}{n-1}\sum_{i=1}^{n}\Delta a_i^2,$$

where the radial (Δr_i) and azimuthal (Δa_i) residuals are given by Eqs. (2). The lower σ level is 410 ± 30 km, as inferred from the three samples. Assuming that it is completely attributable to the total errors of pointing at the sunspot and fragment centers during measurements, we subtract this lower dispersion level from the observational data as noise: $\sigma = \sqrt{\sigma_{\text{obs}}^2 - 410^2}$ (which corre-

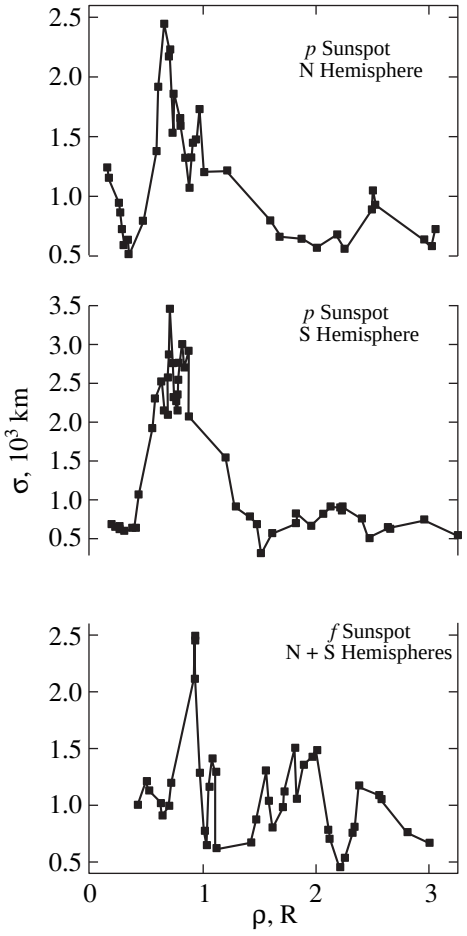

Fig. 1. Dispersion of the fragment coordinates verses radial distance.

sponds to an upper limit of $410/\sqrt{2} = 290$ km on the error of pointing at the sunspot or fragment center).

In Fig. 1, fragment-coordinate dispersion is plotted against radial distance; this plot was obtained by linear three-point smoothing. The pattern can be described as follows. The *umbra*: σ may decrease insignificantly, from 1100 to 600 km, as one recedes from the center to the umbra boundary ($\rho \approx 0.45$). The *penumbra*: σ monotonically increases, reaching its absolute maximum $\sigma_{max} \approx 2600$ km at $\rho \approx 0.8$, and then gradually decreases to 400 km in the region of the outer bright ring ($\rho \approx 1.6$). The *pore zone*: a double-peak maximum ($\sigma_{max\,1} \approx 1100$ km at $\rho \approx 2.2$ and $\sigma_{max\,2} \approx 900$ km at $\rho \approx 2.8$) associated with the convective roller surrounding the sunspot (Nagovitsyna and Nagovitsyn 1999, 1998a) is most likely localized here; however, this peak is significant, reaching 1500 km, only for the *f* sunspots. We also see that the *f* sunspots have a σ maximum in the penumbra that is narrower than that for the *p* sunspots. This generally reflects a weaker development of the relatively narrower penumbra in the *f* sunspots.

Assuming a harmonic oscillator, the absolute maximum of the coordinate dispersion in the penumbra (2600 km) corresponds to the oscillation amplitude

$$A = \sqrt{2}\,\sigma \approx 3700 \text{ km},$$

which accounts for about one-tenth of the sunspot diameter. For a characteristic oscillation period of T = 50 min [the period at which the energy of a harmonic oscillator reaches a maximum in the period range 30–300 min (Nagovitsyna and Nagovitsyn 1998b)], this corresponds to the velocity amplitude

$$V_{max} = \frac{2\pi A}{T} \approx 8 \text{ km s}^{-1}.$$

Since the oscillations under consideration are not harmonic, these values are upper limits on the parameters.

The inferred radial variations in fragment oscillation amplitude qualitatively correspond to the variations in the magnitude of the velocity of their linear trends (Nagovitsyna and Nagovitsyn 1999) and to the variations in radial velocity of the matter from the sunspot, which was deduced spectroscopically and is known as the Evershed effect. Such synchronous variations in various characteristics of the *horizontal* velocity are probably attributable to the three-dimensional magnetic-field structure or, more specifically, to the radial variation in the ratio of its horizontal and vertical components (the penumbra field is known to be virtually horizontal).

OSCILLATION ORIENTATION

As was noted in the Introduction, the tube oscillations in polar coordinates have both a radial component, which shows up in sunspot area variations, and an azimuthal component, which shows up in torsional matter oscillations. The coordinate method allows the ratio of these components in fragment oscillations to be directly determined, for example, as the angular deviation of these oscillations from the radial direction

$$d = \arctan b.$$

The most probable value of b can be determined by least squares technique from the system of equations

$$\Delta a_i = b\Delta r_i + c, \quad i = 1\text{–}22,$$

where the experimental radial (Δr_i) and azimuthal (Δa_i) oscillation components are given by (2). Thus, d is actually the angle between the principal axis of the cloud of data points formed by the dispersion of the fragment coordinates and the radial direction toward the center of this cloud.

Contrary to our expectations, we could not find any definite radial-distance dependence of the orientation of fragment oscillations, much as we did for the orien-

tation of their linear trends. Note that the radial gradient in trend orientation allowed us to detect a spiral macrostructure (Nagovitsyna and Nagovitsyn 1999, 1998a). At the same time, the azimuthal variations, which are related to heliographic coordinates by (1), proved to be most pronounced in the oscillation orientation.

In Fig. 2, angular deviation of the oscillations from the radial direction is plotted against fragment azimuth; the function $d(\theta)$ was obtained by linear seven-point smoothing. We can see that $d(\theta)$ successively passes through four extrema of different amplitude and opposite sign: the positive peaks are located roughly northeast and southwest of the sunspot center, while the negative peaks lie northwest and southeast. According to (1), the positive and negative values of d correspond to counterclockwise and clockwise deviations of the oscillations from the radial direction, respectively.

MAGNETIC-FIELD STRUCTURE

It would be natural to assume that the azimuthal variations in the orientation of magnetic-fragment oscillations are attributable to the azimuthally anisotropic magnetic-field structure in the sunspot region. The experimentally measured angular deviation $d(\theta)$ (Fig. 2) can be used to numerically simulate the horizontal configuration of field lines as follows. For each of the three samples, we fit $d(\theta)$ by second- or third-degree polynomials $p(\theta)$ in four azimuthal sectors containing individual positive or negative extrema of d and then join the polynomials at the ends (dashed line in Fig. 2). The shape of the field line is modeled as the trajectory $\rho(t)$, $\theta(t)$ in polar coordinates that is described by a point moving at angle $p(\theta(t))$ to the radial direction (t is the time). In this case, we introduce discreteness: the point is assumed to traverse small distances s in time intervals Δt. Having the polar coordinates ρ_i, θ_i at time t_i, the point then moves at angle $p(\theta_i)$ and passes at time $t_{i+1} = t_i + \Delta t$ to the position

$$\rho_{i+1} = \sqrt{\rho_i^2 + 2\rho_i s\cos p(\vartheta_i) + s^2},$$

$$\vartheta_{i+1} = \vartheta_i + \arctan\frac{s\sin p(\vartheta_i)}{\rho_i + s\cos p(\vartheta_i)}.$$

The point with the ρ_{i+1} and θ_{i+1} coordinates will move at angle $p(\theta_{i+1})$ and pass to the next position, according to the above recursion relation. Thus, specifying the initial position at 10° azimuthal intervals, we obtain a family of trajectories in the range $\rho = 0.3$–3.3, which corresponds to the observed deviations $d(\theta)$ in Fig. 2 and are assumed to reflect the horizontal shape of field lines in the region of the major spots of bipolar groups (Fig. 3).

As we see from Fig. 3, the highest concentration of field lines, i.e., an increase in magnetic-field strength, takes place along the E–W axis of the group connecting the major spots of opposite polarity—this is a possible

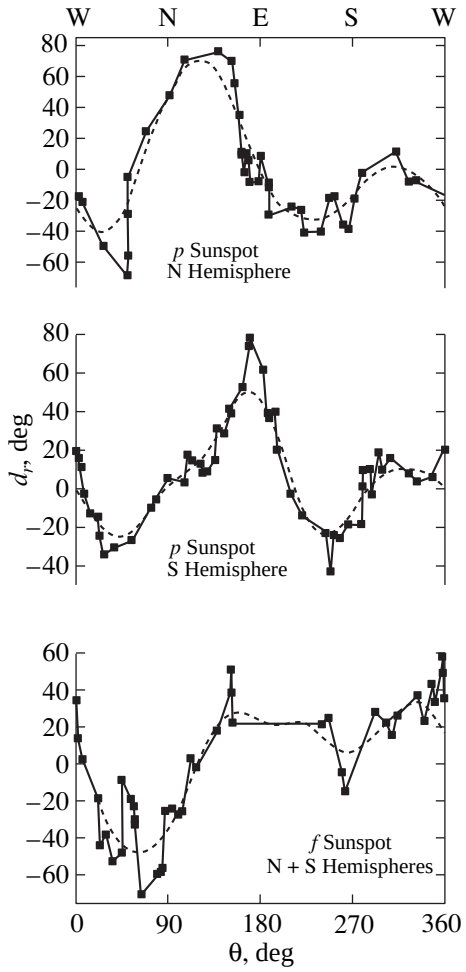

Fig. 2. Angular deviation of fragment oscillations from the radial direction versus azimuth. The dashed line indicates a polynomial fit.

reflection of their opposing inclination due to tube curvature above the photosphere. We can even see that the concentration of field lines for the p sunspots reaches a maximum not in the E direction, but at some deviation (~15°) toward the pole of the hemisphere where the group is located. This result probably reflects the phenomenon that is known as the *tilt of the group axis relative to the equator*: the p sunspots are mostly located at lower heliographic latitudes than the f sunspots. According to current views, this effect is assumed to be due to the Coriolis force that acts on the expanding Ω-shaped tube of an active region rising from the depth of the convection zone.

The meridional flattening of the sunspot magnetic-field structure (clearly seen in Fig. 3) corresponds to the above latitude–longitude asymmetry, which makes the visible sunspots elliptical in shape. Figure 3 shows how this effect bends the field lines and proves its physical reality. However, we cannot yet explain this phenomenon.

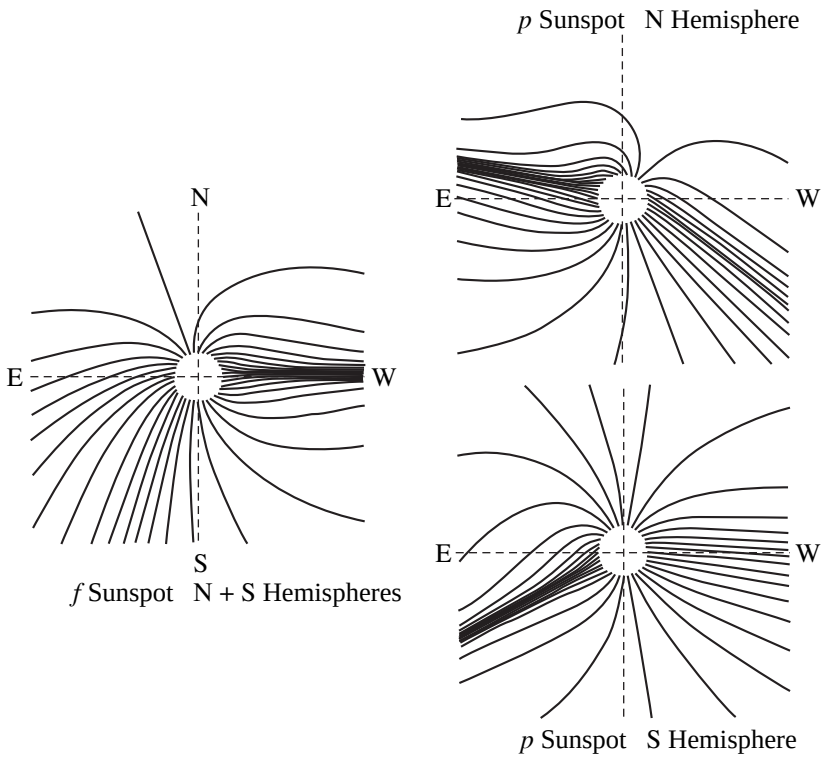

Fig. 3. Horizontal magnetic field in the region of the major sunspots of bipolar groups obtained by numerically simulating the shapes of magnetic field lines based on the observed oscillation orientation (corresponds to the dashed line in Fig. 2).

Curiously, the distribution of field lines in Fig. 3 generally matches the distribution of bundles in bipolar groups: pores are more commonly observed between the major spots along the E–W axis of the group, slightly more rarely westward of the *p* sunspots and eastward of the *f* sunspots, and rarely at markedly differing latitudes. This relationship may stem from the fact that the horizontal magnetic field of a bipolar group stabilizes the vertical bundles by compressing them in the transverse direction and slowing down their decay.

CONCLUSION

Our analysis shows that the photospheric spatial oscillations of magnetic fragments allow several fine features of the magnetic-field structure in active regions to be traced:

(1) The functional dependence of the oscillation amplitude on radial distance with a maximum in the sunspot penumbra may reflect radial variations in the ratio of the vertical and horizontal magnetic fields.

(2) The functional dependence of the oscillation orientation on azimuth may reflect meridional flattening of the magnetic-field structure.

(3) The peculiar deviations of oscillations from the radial direction may reflect tube curvature above the surface and a tilt of the axis of a sunspot group to the equator.

The peculiar features of the quasi-periodic dynamics revealed here cannot be accidental in nature, because they are reproduced for three independent samples. They come as no surprise to us, because they are in good agreement with other observational facts. Unfortunately, the spatial oscillations of magnetic fragments have not yet allowed us to reveal the special evidence of the spiral magnetic-field macrostructure found in the linear component of their motion (Nagovitsyna and Nagovitsyn 1999, 1998a).

ACKNOWLEDGMENTS

This study was supported by the Russian State Program “Astronomy” (project no. 1.5.1.3).

REFERENCES

1. V. S. Bashkirtsev, N. I. Kobanov, and G. P. Mashnich, Sol. Phys. **82**, 443 (1983).
2. B. I. Demchenko, G. S. Minasyants, N. G. Makarenko, and S. O. Obashev, Astron. Tsirk., 3 (1985).
3. S. I. Gopasyuk, Izv. Krym. Astrofiz. Obs. **73**, 9 (1985).
4. R. Keppens and P. V. Martínez, Astron. Astrophys. **316**, 229 (1996).

5. G. P. Mashnich and V. S. Bashkirtsev, Sol. Phys. **185**, 35 (1999).

6. Yu. A. Nagovitsyn and E. Yu. Nagovitsyna, Kinematika Fiz. Nebesnykh Tel **12**, 55 (1996).

7. E. Yu. Nagovitsyna, Author's Abstract of Candidate's Dissertation (GAO Akad. Nauk SSSR, Leningrad, 1990).

8. E. Yu. Nagovitsyna and Yu. A. Nagovitsyn, Pis'ma Astron. Zh. **24**, 554 (1998a).

9. E. Yu. Nagovitsyna and Yu. A. Nagovitsyn, in *A New Solar Cycle: Observational and Theoretical Aspects (Proceedings of Conference)* (GAO Ross. Akad. Nauk, St. Petersburg, 1998b), p. 129.

10. E. Yu. Nagovitsyna and Yu. A. Nagovitsyn, Sol. Phys. **186**, 193 (1999).

11. V. N. Obridko, *Sunspots and Activity Complexes* (Nauka, Moscow, 1985).

Translated by A. Dambis

Astronomy Letters, Vol. 27, No. 2, 2001, pp. 124–133. Translated from Pis'ma v Astronomicheskiĭ Zhurnal, Vol. 27, No. 2, 2001, pp. 150–160.

On the Motion of a Mass Point Inside a Rotating Inhomogeneous Ellipsoidal Body

S. A. Gasanov*

Sternberg Astronomical Institute, Universitetskiĭ pr. 13, Moscow, 119899 Russia

Received December 1, 1999

Abstract—The plane motion of a mass point inside an inhomogeneous rotating ellipsoidal body with a homothetic density distribution is considered. The force function of the problem is expanded in terms of the ellipsoid's second eccentricities up to the fourth order, which are taken as small parameters. We derive an expression for the perturbing function and solve the equations of perturbed motion in orbital elements. © *2001 MAIK "Nauka/Interperiodica".*

Key words: *rotating inhomogeneous ellipsoidal bodies; homothetic (ellipsoidal) density distribution; general potential, perturbing function*

INTRODUCTION

Abalakin (1959) considered the spatial motion of a mass point inside an inhomogeneous ellipsoidal body with a homothetic density distribution in a stationary coordinate system. Periodic solutions were found, and qualitative studies were carried out. This problem arises, in particular, when studying the motion of an individual star inside a star cluster under the gravity of the entire system. The problem can be solved if semicollisions and collisions between cluster stars and their effects on the motion of this star are disregarded, at least to a first approximation (Abalakin 1959).

Such problems are considered when studying the structures and evolution of galaxies and stellar systems in a rotating coordinate system. Kuzmin (1956) investigated a model of a stationary Galaxy with a gravitational field that, apart from the energy and kinetic-momentum integrals, admits the third integral of motion proposed by this author. If the density on the symmetry axis rapidly decreases with increasing distance from the center, then the surfaces of constant density prove to be considerably flattened. In this case, the density distribution and the corresponding gravitational potential are generally consistent with the current view of the Galactic structure.

When studying the structure and evolution of barred spiral galaxies, Freeman (1966a, 1966b, 1966c) and Hunter (1974) showed that, in Hubble's classification, the direction of evolution in conventional notation is SBc $\longrightarrow$ SBa.

Of considerable interest are the works by Tim de Zeew and others, who considered various models of triaxial ellipsoidal bodies with gravitational potentials in the form of Stäckel's (1890, 1891) potential in ellipsoidal coordinates with separable variables. These models are used to solve problems on the motion of stars inside elliptical, spiral, and lenticular galaxies and other problems (Tim de Zeew and Merrit 1983; Tim de Zeew and Lynden-Bell 1985; Tim de Zeew 1985a, 1985b; Tim de Zeew *et al.* 1986; Tim de Zeew and Carollo 1996).

In the problem under consideration, our goal is to solve the equations of perturbed motion in orbital elements in a rotating coordinate system. In addition, terms up to the fourth order inclusive relative to the second eccentricities of the ellipsoid in question, which are assumed to be small parameters, are retained in the perturbing function. We also average the perturbing function over the rapidly changing angular variable.

STATEMENT OF THE PROBLEM AND THE FORCE FUNCTION

Consider an inhomogeneous body T bounded by an ellipsoidal surface

$$\frac{x^2}{A^2} + \frac{y^2}{B^2} + \frac{z^2}{C^2} = 1, \qquad (1)$$

assuming that $A > B > C$.

Let the density ρ of this body be a function of some parameter p and vary continuously from the center to the external surface. We assume that the body has a homothetic (ellipsoidal) density distribution; i.e., its layers of equal density are bounded by similar ellipsoidal surfaces with the same orientation relative to each other. Such a density distribution satisfactorily repre-

* E-mail address for contact: gasnizh@sai.msu.ru

1063-7737/01/2702-0124$21.00 © 2001 MAIK "Nauka/Interperiodica"

sents the density distribution for an ellipsoidal body that is stationary or rotates with a relatively low angular velocity about the polar *OZ* axis (Abalakin 1959). The constraint imposed on the angular velocity stems from the fact that, at a sufficiently high angular velocity of an inhomogeneous ellipsoidal body, its existence as an equilibrium figure requires that the interfaces between the layers of equal density be confocal ellipsoids (Tisserand 1891).

Consider the motion of a passively gravitating mass point inside a given ellipsoidal body under the attraction from this body alone.

Let a mass point P move inside an ellipsoidal body T rotating at a constant and relatively low angular velocity m about the OZ axis and having a homothetic density distribution. The x, y, z coordinates of this point are referred to a rectangular coordinate system with the origin O at the center of the ellipsoidal body and with the OX, OY, and OZ axes along the corresponding principal axes of the ellipsoid (1).

We can draw an ellipsoidal surface given by the following equation through point $P(x, y, z)$ at each instant of time t:

$$\frac{x^2}{\bar{\alpha}^2} + \frac{y^2}{\bar{\beta}^2} + \frac{z^2}{\bar{\gamma}^2} = 1. \quad (2)$$

This surface separates the ellipsoidal inhomogeneous body T bounded by the ellipsoidal surface (1) into two parts, E and I. Let V_e be the potential at point P produced by the ellipsoidal body bounded by the surface (2) and correspond to part E and V_i be the potential at the same point P produced by the ellipsoidal layer confined between the surfaces (1) and (2) and correspond to part I. Therefore, the total potential V produced by the ellipsoidal inhomogeneous body T at the internal point $P(x, y, z)$ at each instant of time t can be represented as the sum

$$V = V_e + V_i. \quad (3)$$

Note that the potentials V_e and V_i produced by the inhomogeneous ellipsoidal body and layer at point P can be expressed in terms of the well-known potentials produced by an inhomogeneous ellipsoid at the external and internal points, respectively. To this end, we consider a homogeneous ellipsoid with a density ρ bounded by an ellipsoidal surface

$$\frac{\xi^2}{\alpha^2} + \frac{\eta^2}{\beta^2} + \frac{\zeta^2}{\gamma^2} = 1, \quad (4)$$

whose α, β, and γ semiaxes are so far arbitrary. The following expressions in Dirichlet's form are known for the potential of this body:

$$\rho V_e' = \pi f \alpha\beta\gamma\rho \int_u^\infty L(s)K(s)ds \quad (5)$$

is the potential at the external point $P(x, y, z)$, and

$$\rho V_i' = \pi f \alpha\beta\gamma\rho \int_0^\infty L(s)K(s)ds \quad (6)$$

is the potential at the internal point in the same notation. Here, f is the gravitational constant, and the functions $L(s)$ and $K(s)$ are given by

$$L(s) = 1 - \frac{x^2}{\alpha^2 + s} - \frac{y^2}{\beta^2 + s} - \frac{z^2}{\gamma^2 + s},$$

$$K(s) = \frac{1}{\sqrt{(\alpha^2 + s)(\beta^2 + s)(\gamma^2 + s)}}.$$

The lower limit u of the integral in (5) is a positive root of the cubic equation for u

$$\frac{x^2}{\alpha^2 + u} + \frac{y^2}{\beta^2 + u} + \frac{z^2}{\gamma^2 + u} = 1. \quad (7)$$

It is a function of the coordinates of the attracted point P and the ellipsoid semiaxes.

Consider a layer of the inhomogeneous ellipsoidal body T with density $\rho(p^*)$ confined between the surfaces of the ellipsoids with semiaxes α^*, β^*, γ^* and $\alpha^* + d\alpha^*$, $\beta^* + d\beta^*$, and $\gamma^* + d\gamma^*$. The semiaxes of these ellipsoids are assumed to be functions of the same parameter p and correspond to its values p^* and $p^* + dp^*$. The elementary potentials produced by this infinitely thin layer at the external and internal points for $\alpha^* = \alpha$, $\beta^* = \beta$, and $\gamma^* = \gamma$ ($p^* = p$) are (Subbotin 1941)

$$dV_e = \rho(p)\frac{dV_e'}{dp}dp, \quad dV_i = \rho(p)\frac{dV_i'}{dp}dp. \quad (8)$$

If p_c and p_f correspond to the center and external surface of the ellipsoidal body, respectively, then the total potential V produced by the inhomogeneous ellipsoidal body T at the internal point P can be determined, in view of (3), by integrating and subsequently summing expressions (8) for homothetic layers over p. In this case, the integration is performed in the segment $[p_c, \bar{p}]$ for the potential $\rho V_e'$ and in the segment $[\bar{p}, p_f]$ for $\rho V_i'$. Here, $\bar{p}$ is the value of p corresponding to the boundary ellipsoidal surface (2). Consequently, the total potential V is given by

$$V = \int_{p_c}^{\bar{p}} \rho(p)\frac{dV_e'}{dp}dp + \int_{\bar{p}}^{p_f} \rho(p)\frac{dV_i'}{dp}dp. \quad (9)$$

Assuming that $\alpha > \beta > \gamma$, we define the second eccentricities λ and μ of the ellipsoid (4) by the equations

$$\lambda^2 = \frac{\alpha^2 - \gamma^2}{\gamma^2}, \quad \mu^2 = \frac{\beta^2 - \gamma^2}{\gamma^2};$$

hence,

$$\alpha^2 = \gamma^2(1+\lambda^2), \quad \beta^2 = \gamma^2(1+\mu^2), \quad (\mu^2 < \lambda^2 < 1). \tag{10}$$

We take the ratio of the polar semiaxes of the ellipsoidal surfaces (4) and (1) squared as the parameter p; i.e., we set

$$p = \frac{\gamma^2}{C^2}, \quad (0 \le p \le 1, \quad p_c = p(0) = 0, \quad p_f = p(C) = 1). \tag{11}$$

In this case, the value $\bar{p}$ of p can be directly inferred from (2) using the formula

$$\bar{p} = \frac{\bar{\gamma}^2}{C^2} = \frac{1}{C^2}\left[r^2 + \sum_{k=1}^{\infty}(-1)^k(\lambda^{2k}x^2 + \mu^{2k}y^2)\right], \tag{12}$$

which is derived by expanding the left part of Eq. (2) in terms of the second eccentricities λ and μ, in view of (10) and (11). Since the second eccentricities λ and μ coincide for any homothetic ellipsoidal layers, the semiaxes α and β when passing from layer to layer are functions of p alone. Consequently, the density of the inhomogeneous ellipsoidal body is a function of p alone. The density ρ can therefore be represented as a converging power series of p:

$$\rho = \rho(p) = \rho_0 + \sum_{n=1}^{\infty}\rho_n\varepsilon^n p^n, \quad (0 < \varepsilon < 1), \tag{13}$$

where ε is a small parameter characterizing the density distribution. In addition, the following conditions are satisfied:

$$\rho(0) = \rho_0 > 0, \quad \rho(1) = \rho_f, \quad \rho_n < 0, \quad (n = 1, 2, \ldots). \tag{14}$$

Here, ρ_0 and ρ_f are the densities at the center and on the surface of ellipsoidal body T, respectively.

In expression (5) for the potential $\rho V_e'$ of a homogeneous ellipsoid, we introduce a new variable ξ in place of the integration variable s, which is given by

$$\xi = \frac{\gamma}{\sqrt{\gamma^2 + s}}. \tag{15}$$

Clearly, $\xi \le 1$ for $s \ge 0$. The range of the variable s, the half-segment $[u, \infty]$, then changes to $[U, 0]$, where U is given, according to (15), by

$$U = \frac{\gamma}{\sqrt{\gamma^2 + u}}. \tag{16}$$

After changing the variable, expression (5) can be written as

$$\rho V_e' = \frac{G}{2}\rho\int_0^U\left(\frac{\gamma^2}{\xi^2} - \frac{x^2}{1+\lambda^2\xi^2} - \frac{y^2}{1+\mu^2\xi^2} - z^2\right) \times \frac{\xi^2 d\xi}{\sqrt{(1+\lambda^2\xi^2)(1+\mu^2\xi^2)}}, \tag{17}$$

where

$$G = 4\pi f\sqrt{(1+\lambda^2)(1+\mu^2)}.$$

We take into account inequality (10) and the condition $|\xi| \le 1$. Expanding the coefficients of x^2 and y^2 in formula (17) in a binomial power series of $\lambda^2\xi^2$ and $\mu^2\xi^2$, we then obtain for the potential $\rho V_e'$

$$\rho V_e' = \frac{G}{2}\rho\int_0^U\left[\frac{\gamma^2}{\xi^2} - x^2\sum_{k=0}^{\infty}(-1)^k(\lambda\xi)^{2k} - y^2\sum_{k=0}^{\infty}(-1)^k(\mu\xi)^{2k} - z^2\right] \times \sum_{i+j=1}^{\infty}(1 + a_{ij}\lambda^{2i}\mu^{2j}\xi^{2(i+j)})\xi^2 d\xi. \tag{18}$$

The potential V_i at the internal point is easier to calculate: it will suffice to set $u = 0$, i.e., $U = 1$, in (5) or (18). In addition, it may be shown that Eq. (7) defines u as an implicit holomorphic function of all its arguments. Indeed, in view of Eqs. (10) and (16), Eq. (7) can be written as

$$\frac{x^2}{1+\lambda^2U^2} + \frac{y^2}{1+\mu^2U^2} + z^2 = \frac{\gamma^2}{U^2}. \tag{19}$$

Since the second eccentricities are small, we introduce an auxiliary small parameter ν:

$$\lambda^2 = \lambda_0^2\nu, \quad \mu^2 = \mu_0^2\nu, \quad (0 < \nu < 1). \tag{20}$$

Then, assuming that

$$w = U^2, \quad b = \frac{\gamma^2}{r^2}, \quad f(w) = \frac{\alpha_1}{r^2}w^2 - \frac{\beta_1}{r^2}\nu w^3, \tag{21}$$

where

$$\alpha_1 = \lambda_0^2x^2 + \mu_0^2y^2, \quad \beta_1 = \lambda_0^4x^2 + \mu_0^4y^2, \tag{22}$$

we derive from Eq. (19)

$$w - b - \nu f(w) = 0. \tag{23}$$

Clearly, the function $f(w)$ given by (21) is a holomorphic (even integer) function of its arguments. Therefore, Eq. (23) has a unique root, which is a holomorphic (integer) function of b provided that the inequality

$$\frac{|\nu f(w)|}{|w-b|} < 1$$

is satisfied on the entire complex plane. Using relations (21), this root can then be represented as a series (Duboshin 1975):

$$\begin{aligned} w &= b + \nu f(b) + \nu^2 f(b) f'(b) + \ldots \\ &= \frac{\gamma^2}{r^2}\left[1 + \frac{\gamma^2}{r^4}\alpha_1\nu + \frac{\gamma^4}{r^8}(2\alpha_1^2 - \beta_1 r^2)\nu^2\right], \end{aligned} \tag{24}$$

where the terms of the third or higher orders in ν were discarded. Here, α_1 and β_1 are given by (22). Since $U^2 = w$, we easily find from (24)

$$U = \frac{\gamma}{r}[1 + U_1\nu + U_2\nu^2 + \ldots], \tag{25}$$

where

$$U_1 = \frac{\gamma^2}{2r^4}\alpha_1, \quad U_2 = \frac{\gamma^4}{8r^8}(7\alpha_1^2 - 4\beta_1 r^2). \tag{26}$$

The expansion (24), in which the terms up to ν^2 inclusive were retained, converges in view of Eqs. (16) and (20) for all x and y that satisfy the inequality $|u| < \gamma^2$.

Thus, to derive the final expression for the potential V_e requires determining a positive root of the cubic equation (7) and then, in view of (16), finding the corresponding value of U. Integrating expression (18) and substituting the derived U yields

$$\rho V_e' = \frac{G}{2}\rho(\gamma^2 X_0 - x^2 X_1 - y^2 X_2 - z^2 X_3), \tag{27}$$

where the coefficients X_k ($k = 0, 1, 2, 3$) are polynomials for U and the second eccentricities λ^2 and μ^2 (or the small parameter ν), which are presented in Appendix A. Therefore, the inequality (10) and the convergence condition for the series (25) ensure that the expansion (27) converges.

Similarly, we obtain for the attractive potential $\rho V_i'$ produced by a homogeneous ellipsoid at the internal point ($U = 1$)

$$\rho V_i' = \frac{G}{2}\rho[\gamma^2 Y_0 - x^2 Y_1 - y^2 Y_2 - z^2 Y_3], \tag{28}$$

where the coefficients Y_k ($k = 0, 1, 2, 3$) are polynomials for the second eccentricities λ^2 and μ^2 (or the small parameter ν), which are also presented in Appendix A.

The convergence of (28) is ensured by the same conditions as the convergence of the expansion (27).

Let us substitute the expansions (27) and (28) and expression (13) for $\rho(p)$ in formula (9), in which Eqs. (11) and (12) must be taken into account. Performing elementary operations and transformation of the integrand, we then obtain, after integration, an expression for the total potential V. Since we consider a two-dimensional problem, this expression for V at $z = 0$ takes the form

$$V = V_0 + R, \quad V_0 = -\frac{1}{2}(V_{01}x^2 + V_{02}y^2), \tag{29}$$

$$\begin{aligned} R &= \frac{\varepsilon}{4}(R_1 x^4 + R_2 y^4 + 2R_3 x^2 y^2) \\ &+ \frac{\varepsilon^2}{6}(R_4 x^6 + R_5 y^6 + 3R_6 x^4 y^2 + 3R_7 x^2 y^4) + \ldots, \end{aligned} \tag{30}$$

where the coefficients $V_{01}, \ldots, R_6, R_7$ are polynomials for the second eccentricities λ^2 and μ^2, which are provided in Appendix A.

UNPERTURBED MOTION OF A MASS POINT INSIDE AN INHOMOGENEOUS ELLIPSOID

Consider the plane motion of a mass point P inside an ellipsoidal body rotating at a constant and relatively low angular velocity m about the OZ axis. The coordinates x, y, z of this point are referred to a rectangular coordinate system with origin O at the center of this ellipsoidal body and with the OX, OY, and OZ axes along the corresponding principal axes. If point $P(x, y, z)$ moves in the equatorial plane of the ellipsoidal body, which is taken as the principal coordinate plane, then the problem reduces to solving the system of differential equations

$$\begin{aligned} \frac{d^2x}{dt^2} - 2m\frac{dy}{dt} - m^2 x &= \frac{\partial V}{\partial x}, \\ \frac{d^2y}{dt^2} + 2m\frac{dx}{dt} - m^2 y &= \frac{\partial V}{\partial y}. \end{aligned} \tag{31}$$

We now turn to expression (29) for the total potential. Assume that the difference between inhomogeneous and homogeneous ellipsoids is sufficiently small. Discarding the terms of the order of and higher than ε^2, we obtain from (29) and (30)

$$V = V_0 + \bar{R}, \quad \bar{R} = \frac{\varepsilon}{4}(R_1 x^4 + R_2 y^4 + 2R_3 x^2 y^2). \tag{32}$$

Therefore, $\bar{R}$ and V_0 are called the perturbing function and the attractive potential in unperturbed motion, respectively.

Let us now set up the equations of unperturbed motion. To this end, we set $\varepsilon = 0$ in expression (32) for V. The system of equations (31) then takes the form

$$\begin{aligned} \frac{d^2x}{dt^2} - 2m\frac{dy}{dt} + g_1^2 x &= 0, \\ \frac{d^2y}{dt^2} + 2m\frac{dx}{dt} + g_2^2 y &= 0. \end{aligned} \tag{33}$$

Here, we set

$$g_1^2 = V_{01} - m^2, \quad g_2^2 = V_{02} - m^2. \tag{34}$$

The right parts are positive by virtue of Poincaré's inequality, which is a necessary condition for the equilibrium of rotating ellipsoidal figures. Indeed, in our case, Poincaré's inequality is (Poincaré 1911; Ogorodnikov 1958):

$$m^2 < \frac{G\rho_0}{6}\Big[1 - \frac{3}{10}(\lambda_0^2 + \mu_0^2)\nu + \frac{3}{56}(3\lambda_0^4 + 2\lambda_0^2\mu_0^2 + 3\mu_0^4)\nu^2\Big] = g^2. \quad (35)$$

On the other hand, in view of (10) and (35), we have

$$m^2 < g^2 < V_{01} < V_{02}, \quad g_1^2 < g_2^2. \quad (36)$$

Consequently, Eq. (34) hold, and the angular velocity m of the coordinate system satisfies the inequalities (35) and (36).

We now multiply the first equation by dx/dt and the second equation by dy/dt. Adding up these equations and performing integration yield an analog of the Jacobi integral for the system of equations (33) of unperturbed motion in the form

$$\left(\frac{dx}{dt}\right)^2 + \left(\frac{dy}{dt}\right)^2 + g_1^2x^2 + g_2^2y^2 = 2c_0, \quad (37)$$

where $c_0 > 0$ is the integration constant. It follows from the integral (37) that

$$g_1^2x^2 + g_2^2y^2 < 2c_0. \quad (38)$$

Consequently, in the two-dimensional problem, point P can move inside the ellipsoid under consideration only inside the ellipse with the semiaxes

$$a = \frac{\sqrt{2c_0}}{g_1}, \quad b = \frac{\sqrt{2c_0}}{g_2}. \quad (39)$$

We now turn to solving the system of equations (33), whose characteristic equation can be rewritten as (Matveev 1967)

$$\Lambda^4 + (4m^2 + g_1^2 + g_2^2)\Lambda^2 + g_1^2g_2^2 = 0. \quad (40)$$

In view of the conditions (36), this equation has purely imaginary roots. The solution to the system (33) can then be represented as (Matveev 1967)

$$x = C_1\cos\beta_1 + P_2C_2\sin\beta_2,$$
$$y = P_1C_1\sin\beta_1 + C_2\cos\beta_2, \quad (41)$$

where

$$\beta_n = \theta_n t + \sigma_n, \quad (n = 1, 2), \quad P_1^2 < P_2^2 < 1. \quad (42)$$

Here, C_n and σ_n are arbitrary constants; the roots $\Lambda_n^2 = -\theta_n^2$ of the biquadratic equation (40) and the quantities P_n ($n = 1, 2$) are given in Appendix A.

The orbit (41) can be interpreted as the trajectory of the leading center with frequency θ_1 along an ellipse with semiaxes C_1 and P_1C_1 and as the rotational motion about this center with frequency θ_2 along an ellipse with semiaxes P_2C_2 and C_2. Consequently, the orbit (41) is an elliptical epicycloid.

Note that, apart from c_0 in Eq. (37), we have four more arbitrary constants C_n and σ_n ($n = 1, 2$). However, in view of the solution (41), we obtain the relation between c_0 and the constants C_1 and C_2 from the analog of the Jacobi integral (37):

$$2c_0 = (P_1^2\theta_1^2 + g_1^2)C_1^2 + (P_2^2\theta_2^2 + g_2^2)C_2^2 = (\theta_1^2 + P_1^2g_2^2)C_1^2 + (\theta_2^2 + P_2^2g_1^2)C_2^2. \quad (43)$$

EQUATIONS OF PERTURBED MOTION IN ORBITAL ELEMENTS

Consider the system of equations (31) where the perturbing function $\bar{R}$ given by (32) is nonzero. The equations of perturbed motion of point P inside an ellipsoidal body T then take the form

$$\frac{d^2x}{dt^2} - 2m\frac{dy}{dt} + g_1^2x = \frac{\partial\bar{R}}{\partial x},$$
$$\frac{d^2y}{dt^2} + 2m\frac{dx}{dt} + g_2^2y = \frac{\partial\bar{R}}{\partial y}. \quad (44)$$

In this case, the necessary condition (35) for the equilibrium of rotating ellipsoidal figures is (Poincaré 1911; Ogorodnikov 1958)

$$m^2 < g^2 - \varepsilon\bar{g}^2, \quad (45)$$

where g^2 is given by Eq. (35), and $\bar{g}^2$ is given by

$$\bar{g}^2 = -\frac{G\rho_1}{20}\Big[1 - \frac{15}{14}(\lambda_0^2 + \mu_0^2)\nu + \frac{5}{24}(5\lambda_0^4 + 6\lambda_0^2\mu_0^2 + 5\mu_0^4)\nu^2\Big]. \quad (46)$$

Here, we took into account the conditions (14) and (36).

We solve the system (44) by the Lagrangian method (the method of variation of constants), which yields the following system of differential equations:

$$\frac{P_kC_k}{\sigma}\frac{dC_k}{dt} = +\frac{\partial\bar{R}}{\partial\sigma_k},$$
$$\frac{P_kC_k}{\sigma}\frac{d\sigma_k}{dt} = -\frac{\partial\bar{R}}{\partial C_k}, \quad (k = 1, 2). \quad (47)$$

Here, the quantity σ (see Appendix A) depends on m and the roots θ_k. This system is called the system of equations of perturbed motion. Multiplying the first equations by $d\sigma_k/dt$ and the second equations by $-dC_k/dt$, per-

forming summation over $k = 1, 2$, and integrating the derived equations, we obtain the first integral

$$\bar{R} = c_1 = \text{const}. \tag{48}$$

Let us now introduce new action–angle variables L, Q, and l, q:

$$L = \frac{1}{2\sigma}(P_1C_1^2 + P_2C_2^2), \quad Q = \frac{1}{2\sigma}P_2C_2^2,$$
$$l = \beta_1, \quad q = \beta_2 - \beta_1. \tag{49}$$

The system of equations (47) then takes the form

$$\frac{dL}{dt} = \frac{\partial \bar{R}}{\partial l}, \quad \frac{dl}{dt} = \theta_1 - \frac{\partial \bar{R}}{\partial L},$$
$$\frac{dQ}{dt} = \frac{\partial \bar{R}}{\partial q}, \quad \frac{dq}{dt} = \theta_2 - \theta_1 - \frac{\partial \bar{R}}{\partial Q}. \tag{50}$$

This is the system of equations of perturbed motion in the new variables.

Note that for $\varepsilon = 0$ ($L = \text{const}$, $Q = \text{const}$), i.e., in unperturbed motion, the analog of the Jacobi integral (37) in the new variables is

$$c_0 = \theta_1 L + (\theta_2 - \theta_1)Q. \tag{51}$$

Now, using Eqs. (30) and (41), we express the perturbing function $\bar{R}$ in terms of the action–angle variables L, Q and l, q given by (49). Averaging $\bar{R}$ over the rapidly changing variable l gives

$$\bar{R} = \frac{\varepsilon}{4}(R_1x^4 + R_2y^4 + 2R_3x^2y^2)$$
$$= K_0 + K_1\sin q + K_2\cos 2q, \tag{52}$$

with

$$K_0 = \varepsilon(\xi_1Q^2 + 2\xi_2LQ + \xi_3L^2),$$
$$K_2 = \varepsilon\zeta_1Q(L-Q), \tag{53}$$
$$K_1 = \varepsilon\sqrt{Q(L-Q)}[\eta_2Q + \eta_1(L-Q)].$$

The quantities $\xi_1, \xi_2, \ldots, \zeta_1$ are provided in Appendix A. In this case, the first integral (48) is

$$K_0 + K_1\sin q + K_2\cos 2q = c_1, \tag{54}$$

from which it follows that

$$K_2\cos 2q = c_1 - K_0 - K_1\sin q,$$
$$4K_2\sin q = K_1 + E(Q). \tag{55}$$

Here,

$$E(Q) = \sqrt{Q(L-Q)}Y(Q),$$
$$Y(Q) = \pm\sqrt{E_2Q^2 + 2E_1Q + E_0}. \tag{56}$$

The coefficients E_k ($k = 0, 1, 2$) are given in Appendix A. Next, substituting the expression for the perturbing function $\bar{R}$ from (52) into the system of equations (50) and taking into account relations (55) in the derived equations yield

$$\frac{dL}{dt} = 0, \quad \frac{dQ}{dt} = \varepsilon Y(Q)F(Q),$$
$$\frac{dl}{dt} = \theta_1 + \varepsilon F_1(Q), \quad \frac{dq}{dt} = \theta_2 - \theta_1 + \varepsilon F_2(Q), \tag{57}$$

where

$$F(Q) = \frac{1}{4\zeta_1}\sqrt{16\zeta_1^2Q(L-Q) - [\eta_2Q + \eta_1(L-Q) + Y(Q)]^2},$$

$$F_1(Q) = a_0 + a_1Q + \frac{a_2}{L-Q} - \frac{1}{8\zeta_1}\left(\eta_2 + \eta_1 - \frac{\eta_2L}{L-Q}\right)Y(Q), \tag{58}$$

$$F_2(Q) = b_0 + \frac{b_1}{Q} + \frac{b_2}{L-Q} - \frac{L}{8\zeta_1}\left(\frac{\eta_2}{L-Q} - \frac{\eta_1}{Q}\right)Y(Q),$$

and the coefficients a_k and b_k ($k = 0, 1, 2$) are provided in Appendix A.

We obtain another first integral directly from the system (57):

$$L = \text{const}. \tag{59}$$

We now change the variable Q to the new variable u by using the substitution

$$Y(Q) = \pm\sqrt{E_2Q^2 + 2E_1Q + E_0} = \frac{1}{\sqrt{E_2}}(QE_2 + E_1 - u), \quad (E_2 > 0). \tag{60}$$

Hence, it follows that

$$Q = \frac{u^2 - 2E_1u + D}{2E_2u}, \quad D = E_1^2 - E_0E_2 > 0. \tag{61}$$

Consequently, (57) transforms to the system

$$\frac{du}{\sqrt{\Phi(u)}} = \varepsilon A_1 dt,$$
$$\Phi(u) = -(u^4 + \alpha_3u^3 + \alpha_2u^2 + \alpha_1u + \alpha_0), \tag{62}$$

$$\frac{dl}{dt} = \theta_1 + \varepsilon\left(W_0 + W_1u + \frac{W_2}{u} + \frac{W_3}{v_1 - u} + \frac{W_4}{u - v_2}\right),$$

$$\frac{dq}{dt} = \theta_2 - \theta_1 + \varepsilon\left(S_0 + \frac{S_1}{v_1 - u} + \frac{S_2}{u - v_2} + \frac{S_3}{u - v_3} + \frac{S_4}{u - v_4}\right). \tag{63}$$

The quantities A_1, α_k, W_k, S_k, and ν_k are given in Appendix B. The polynomial $\Phi(u)$ from (62) can be represented as

$$\Phi(u) = (u_3 - u)(u - u_4)(u - u_1)(u - u_2), \quad (64)$$

whose roots u_k ($k = 1, 2, 3, 4$) were determined by Ferrari's method and are given in Appendix B. These roots and the quantities ν_k satisfy the conditions

$$\nu_1 > u_3 > u > u_4 > \nu_2 > 0 > \nu_3 > u_1 > u_2 > \nu_4. \quad (65)$$

Therefore, integrating Eq. (62) yields (Gradshteyn and Ryzhik 1971)

$$\varepsilon A_1(t - t_0) = \int_u^{u_3} \frac{d\xi}{\sqrt{\Phi(\xi)}} = \frac{2}{\sqrt{(u_3 - u_1)(u_4 - u_2)}} F(\varphi, k), \quad (66)$$

where $F(\varphi, k)$ is an elliptic integral of the first kind. In addition, we have

$$\varphi = \arcsin\sqrt{\frac{(u_4 - u_2)(u_3 - u)}{(u_3 - u_4)(u - u_2)}}, \quad k = \sqrt{\frac{(u_3 - u_4)(u_1 - u_2)}{(u_3 - u_1)(u_4 - u_2)}}. \quad (67)$$

If we use the Jacobi elliptic functions, then we have, in view of (67),

$$\sin\varphi = \mathrm{sn}\, w, \quad w = B_1(t - t_0), \quad B_1 = \frac{\varepsilon}{2} A_1 \sqrt{(u_3 - u_1)(u_4 - u_2)}, \quad (68)$$

which gives

$$u = \frac{u_3(u_4 - u_2) + u_2(u_3 - u_4)\mathrm{sn}^2 w}{u_4 - u_2 + (u_3 - u_4)\mathrm{sn}^2 w}. \quad (69)$$

The last equality can be used to determine the variable Q from (61). Next, using Eqs. (66) and (68), we can represent the solution of the system (63) as (Gradshteyn and Ryzhik 1971; Sikorskiĭ 1936; Zhuravskiĭ 1941)

$$l = l_0 + (\theta_1 + \varepsilon I_0)t + \varepsilon \sum_{n=1}^{4} I_n \Pi(\varphi, s_n, k),$$
$$q = q_0 + (\theta_2 - \theta_1 + \varepsilon J_0)t + \varepsilon \sum_{n=1}^{4} J_n \Pi(\varphi, \gamma_n, k), \quad (70)$$

where

$$\Pi(\varphi, w_n, k) = \int_0^w \frac{dw}{1 + w_n \mathrm{sn}^2 w}, \quad w_n = \{s_n, \gamma_n\} \quad (n = 1, 2, 3, 4) \quad (71)$$

is an elliptic integral of the third kind, and the coefficients I_0, J_0, I_n, and J_n, as well as the parameters s_n and γ_n ($n = 1, 2, 3, 4$), are provided in Appendix B. Consequently, the solution to the systems of equations (62) and (63) for Q, l, and q can be represented by Eqs. (59), (61), (69), and (70). Note that in practical problems, its expansion (Zhuravskiĭ 1941) can be used in place of the elliptic integral of the third kind:

$$\Pi(\varphi, w_n, k) = D_0 + \frac{1}{2}D_1 k^2 + \frac{3}{8}D_2 k^4 + \ldots + \frac{1 \cdot 3 \ldots (2s-1)}{2 \cdot 4 \ldots 2s} D_s k^{2s} + \ldots. \quad (72)$$

The quantities D_i ($i = 1, 2, \ldots$) are given in Appendix B.

Thus, the solution to the equations of perturbed motion (44), in which the perturbing function R is given by Eq. (52), can be represented as

$$x = \frac{\sqrt{\sigma}}{\sqrt{P_1 P_2}}[\bar{A}\cos l + P_2 \bar{B}\sin(l + q)], \quad \bar{A} = \sqrt{2P_2(L - Q)},$$
$$y = \frac{\sqrt{\sigma}}{\sqrt{P_1 P_2}}[P_1 A \sin l + \bar{B}\cos(l + q)], \quad \bar{B} = \sqrt{2P_1 Q}; \quad (73)$$

i.e., the solution (41) must be expressed in terms of the new variables L, Q, l, and q, which can determined from the systems of equations (62) and (63) by Eqs. (59), (61), (69), and (70), respectively.

CONCLUSION

We have considered the plane motion of a mass point inside an inhomogeneous rotating ellipsoidal body with a homothetic density distribution. The quantity ε, which characterizes the difference between inhomogeneous and homogeneous ellipsoids, was taken as a small parameter. We expanded the force function of the problem in terms of ε to within the second order inclusive, retaining the fourth-order terms with respect to the second eccentricities of the ellipsoid in question. The orbit of the unperturbed motion due to the attraction from a homogeneous ellipsoid was taken as an intermediate one. After averaging the perturbing function, in the expansion of which the terms with ε^2 and higher terms were discarded, we solved the differential equations in orbital elements. In the future, we plan to carry out qualitative studies.

ACKNOWLEDGMENTS

I wish to thank Dr. N.V. Emel'yanov for valuable advice and remarks. This study is devoted to the memory of E.P. Aksenov, a remarkable scientist and man, a

professor of Moscow State University, who formulated the problem considered here.

REFERENCES

1. V. K. Abalakin, Byull. Inst. Teor. Astron. **7**, 327 (1959).
2. G. N. Duboshin, *Celestial Mechanics: Main Problems and Methods* (Nauka, Moscow, 1975).
3. K. C. Freeman, Mon. Not. R. Astron. Soc. **133**, 47 (1966a).
4. K. C. Freeman, Mon. Not. R. Astron. Soc. **134**, 1 (1966b).
5. K. C. Freeman, Mon. Not. R. Astron. Soc. **134**, 15 (1966c).
6. I. S. Gradshteyn and I. M. Ryzhik, *Table of Integrals, Series, and Products* (Nauka, Moscow, 1971; Academic, New York, 1980).
7. C. Hunter, Mon. Not. R. Astron. Soc. **166**, 633 (1974).
8. G. G. Kuzmin, Astron. Zh. **33**, 27 (1956).
9. N. M. Matveev, *Integration of Ordinary Differential Equations* (Vysshaya Shkola, Moscow, 1967).
10. K. F. Ogorodnikov, *Dynamics of Stellar Systems* (Fizmatgiz, Moscow, 1958; Pergamon, Oxford, 1965).
11. H. Poincaré, in *Leçons sur les hypotheses cosmogoniques*, Ed. by A. Hermann *et al.* (Libraire Scientifique, Paris, 1911).
12. Yu. S. Sikorskiĭ, *Elements of Elliptic-Function Theory* (ONTI, Moscow, 1936).
13. M. F. Subbotin, *A Course on Celestial Mechanics* (Fizmatgiz, Moscow, 1941), Vol. 3.
14. P. T. de Zeeuw and D. R. Merrit, Astrophys. J. **267**, 571 (1983).
15. P. T. de Zeeuw and D. Lynden-Bell, Mon. Not. R. Astron. Soc. **215**, 711 (1985).
16. P. T. de Zeeuw, Mon. Not. R. Astron. Soc. **215**, 731 (1985a).
17. P. T. de Zeeuw, Mon. Not. R. Astron. Soc. **216**, 273 (1985b).
18. P. T. de Zeeuw, R. Peletier, and M. Franx, Mon. Not. R. Astron. Soc. **221**, 1001 (1986).
19. P. T. de Zeeuw and C. M. Carollo, Mon. Not. R. Astron. Soc. **281**, 1333 (1996).
20. F. A. Tisserand, *Traite de Mecaniques Celeste* (Gauthier-Villars, Paris, 1891), Vol. 2.
21. P. Stäckel, Math. Ann. **35**, 91 (1890).
22. P. Stäckel, *Über die integration der Hamilton-Jacobischen Differential Gleichung mittelst Separation der Variabeln* (Habilitationsschraft, Halle, 1891).
23. A. M. Zhuravskiĭ, *Handbook on Elliptic Functions* (Akad. Nauk SSSR, Moscow, 1941).

APPENDIX A

$$X_0 = U[1 + U^2E_{01}\nu + U^4E_{02}\nu^2],$$

$$X_1 = \frac{U^3}{3}[1 + U^2E_{11}\nu + U^4E_{12}\nu^2],$$

$$X_2 = \frac{U^3}{3}[1 + U^2E_{21}\nu + U^4E_{22}\nu^2],$$

$$X_3 = \frac{U^3}{3}[1 + U^2E_{31}\nu + U^4E_{32}\nu^2],$$

$$E_{01} = -\frac{1}{6}(\lambda_0^2 + \mu_0^2),\ E_{02} = \frac{1}{40}(3\lambda_0^4 + 2\lambda_0^2\mu_0^2 + 3\mu_0^4),$$

$$E_{11} = -\frac{3}{10}(3\lambda_0^2 + \mu_0^2),\ E_{12} = \frac{9}{56}(5\lambda_0^4 + 2\lambda_0^2\mu_0^2 + \mu_0^4),$$

$$E_{21} = -\frac{3}{10}(\lambda_0^2 + 3\mu_0^2),\ E_{22} = \frac{9}{56}(\lambda_0^4 + 2\lambda_0^2\mu_0^2 + 5\mu_0^4),$$

$$E_{31} = -\frac{3}{10}(\lambda_0^2 + \mu_0^2),\ E_{32} = \frac{3}{56}(3\lambda_0^4 + 2\lambda_0^2\mu_0^2 + 3\mu_0^4),$$

$$Y_0 = 1 - \frac{1}{6}(\lambda_0^2 + \mu_0^2)\nu + \frac{1}{40}(3\lambda_0^4 + 2\lambda_0^2\mu_0^2 + 3\mu_0^4)\nu^2,$$

$$Y_1 = \frac{1}{3}\left[1 - \frac{3}{10}(3\lambda_0^2 + \mu_0^2)\nu + \frac{9}{56}(5\lambda_0^4 + 2\lambda_0^2\mu_0^2 + \mu_0^4)\nu^2\right],$$

$$Y_2 = \frac{1}{3}\left[1 - \frac{3}{10}(\lambda_0^2 + 3\mu_0^2)\nu + \frac{9}{56}(\lambda_0^4 + 2\lambda_0^2\mu_0^2 + 5\mu_0^4)\nu^2\right],$$

$$Y_3 = \frac{1}{3}\left[1 - \frac{3}{10}(\lambda_0^2 + \mu_0^2)\nu + \frac{3}{56}(3\lambda_0^4 + 2\lambda_0^2\mu_0^2 + 3\mu_0^4)\nu^2\right],$$

$$V_{01} = \frac{G\rho_0}{3}\left[1 - \frac{3}{10}(3\lambda_0^2 + \mu_0^2)\nu + \frac{9}{56}(5\lambda_0^4 + 2\lambda_0^2\mu_0^2 + \mu_0^4)\nu^2\right],$$

$$V_{02} = \frac{G\rho_0}{3}\left[1 - \frac{3}{10}(\lambda_0^2 + 3\mu_0^2)\nu + \frac{9}{56}(\lambda_0^4 + 2\lambda_0^2\mu_0^2 + 5\mu_0^4)\nu^2\right],$$

$$R_1 = -\frac{G\rho_1}{5C^2}\left[1 - \frac{5}{14}(5\lambda_0^2 + \mu_0^2)\nu + \frac{5}{72}(35\lambda_0^4 + 10\lambda_0^2\mu_0^2 + 3\mu_0^4)\nu^2\right],$$

$$R_2 = -\frac{G\rho_1}{5C^2}\left[1 - \frac{5}{14}(\lambda_0^2 + 5\mu_0^2)\nu + \frac{5}{72}(3\lambda_0^4 + 10\lambda_0^2\mu_0^2 + 35\mu_0^4)\nu^2\right],$$

$$R_3 = -\frac{G\rho_1}{5C^2}\Big[1-\frac{5}{14}(3\lambda_0^2+3\mu_0^2)\nu + \frac{5}{24}(5\lambda_0^4+6\lambda_0^2\mu_0^2+5\mu_0^4)\nu^2\Big],$$

$$R_4 = -\frac{G\rho_2}{7C^4}\Big[1-\frac{7}{18}(7\lambda_0^2+\mu_0^2)\nu + \frac{7}{88}(63\lambda_0^4+14\lambda_0^2\mu_0^2+3\mu_0^4)\nu^2\Big],$$

$$R_5 = -\frac{G\rho_2}{7C^4}\Big[1-\frac{7}{18}(\lambda_0^2+7\mu_0^2)\nu + \frac{7}{88}(3\lambda_0^4+14\lambda_0^2\mu_0^2+63\mu_0^4)\nu^2\Big],$$

$$R_6 = -\frac{G\rho_2}{7C^4}\Big[1-\frac{7}{18}(5\lambda_0^2+3\mu_0^2)\nu + \frac{35}{88}(7\lambda_0^4+6\lambda_0^2\mu_0^2+3\mu_0^4)\nu^2\Big],$$

$$R_7 = -\frac{G\rho_2}{7C^4}\Big[1-\frac{7}{18}(3\lambda_0^2+5\mu_0^2)\nu + \frac{35}{88}(3\lambda_0^4+6\lambda_0^2\mu_0^2+7\mu_0^4)\nu^2\Big],$$

$$\theta_1^2 = \frac{1}{2}(w^2-\sqrt{w^4-4g_1^2g_2^2}),$$

$$\theta_2^2 = \frac{1}{2}(w^2+\sqrt{w^4-4g_1^2g_2^2}),\quad w^2 = 4m^2+g_1^2+g_2^2,$$

$$P_1 = \frac{g_1^2-\theta_1^2}{2m\theta_1} = \frac{2m\theta_1}{g_2^2-\theta_1^2},$$

$$P_2 = \frac{\theta_2^2-g_2^2}{2m\theta_2} = \frac{2m\theta_2}{\theta_2^2-g_1^2},\quad \sigma = \frac{2m}{\theta_2^2-\theta_1^2},$$

$$\xi_1 = \frac{\sigma^2}{8P_1^2P_2^2} \times[3\chi P_2^2R_1+3\chi P_1^2R_2-4P_1P_2(\chi+3P_1P_2)R_4],$$

$$\xi_2 = \frac{P_2\sigma^2}{8P_1^2P_2^2}[3P_2(2P_1P_2-1) + 3P_1^3(2-P_1P_2)R_2+2P_1(\chi+3P_1P_2)R_4],$$

$$\xi_3 = \frac{\sigma^2}{8P_1^2}[3R_1+3P_1^4R_2+2P_1^2R_4],$$

$$\chi = 1-4P_1P_2+P_1^2P_2^2,$$

$$\eta_1 = \frac{\sigma^2}{2P_1\sqrt{P_1P_2}}[3P_2R_1-3P_1^3R_2-P_1(1-P_1P_2)R_4],$$

$$\eta_2 = \frac{\sigma^2}{2P_2\sqrt{P_1P_2}}[3P_2^3R_1-3P_1R_2+P_2(1-P_1P_2)R_4],$$

$$\zeta_1 = -\frac{\sigma^2}{4P_1P_2}[3P_2^2R_1+3P_1^2R_2-(\chi+8P_1P_2)R_4],$$

$$E_2 = (\eta_2-\eta_1)^2-8\zeta_1^2+8\zeta_1\xi_1,$$

$$E_1 = L[\eta_1(\eta_2-\eta_1)+4\zeta_1^2+8\zeta_1\xi_2],$$

$$E_0 = \eta_1^2L^2+8\zeta_1(\xi_3L^2-c_1),$$

$$a_0 = -(\xi_1+2\xi_2+2\xi_3)L-\frac{L}{8\zeta_1}(\eta_1^2+\eta_2^2),$$

$$a_1 = -\xi_1-2\xi_2-\frac{1}{8\zeta_1}(\eta_2^2-\eta_1^2),$$

$$a_2 = (\xi_1+2\xi_2+\xi_3)L^2-c_1+\frac{\eta_2^2L^2}{8\zeta_1},$$

$$b_0 = (\xi_1+2\xi_2)L+\frac{L}{8\zeta_1}(\eta_2^2-\eta_1^2),$$

$$b_1 = \xi_3L^2-c_1+\frac{\eta_2^2L^2}{8\zeta_1},\quad b_2 = -a_2.$$

APPENDIX B

$$A_1 = \mp\frac{N}{8\zeta_1\sqrt{E_2}},\quad \alpha_k = -\frac{N_k}{N^2},\quad (k=0,1,2,3),$$

$$N^2 = 16\zeta_1^2+d_2^2,\quad N_3 = 32\zeta_1^2d_3-4d_2d_1,$$

$$N_2 = -32\zeta_1^2(D+2E_2E_1L+2E_1^2)-4d_1^2-2Dd_0d_2,$$

$$N_1 = 4D(8\zeta_1^2d_3-d_0d_1),\quad N_0 = -D^2(16\zeta_1^2+d_0^2),$$

$$d_0 = \eta_2-\eta_1-\pm\sqrt{E_2},\quad d_1 = E_2\eta_1L-E_1(\eta_2-\eta_1),$$

$$d_2 = \eta_2-\eta_1+\mp\sqrt{E_2},\quad d_3 = E_2L+2E_2,$$

$$W_0 = -(\xi_1+2\xi_2+2\xi_3)L+\frac{E_1}{E_2}(\xi_1+2\xi_2) -\frac{1}{8E_2\zeta_1}[(\eta_1^2+\eta_2^2)LE_2\mp\eta_2LE_2\sqrt{E_2}+(\eta_1^2-\eta_2^2)E_1],$$

$$W_1 = -\frac{1}{16E_2\zeta_1}[(\eta_2+\eta_1)d_2+8\zeta_1(\xi_1+2\xi_2)],$$

$$W_2 = -\frac{D}{16E_2\zeta_1}[(\eta_2+\eta_1)d_0 + 8\zeta_1(\xi_1+2\xi_2)],$$

$$W_{k+2} = \frac{1}{8\zeta_1(\nu_1-\nu_2)}(f_2\nu_k^2 + f_1\nu_k - Df_2),$$
$$(k = 1, 2),$$

$$S_0 = (\xi_1+2\xi_2)L + \frac{L(\eta_2+\eta_1)}{8\zeta_1}d_2, \quad S_k = -W_{k+2},$$
$$(k = 1, 2),$$

$$S_{k+2} = \frac{(-1)^k}{8\zeta_1}\frac{1}{\nu_4-\nu_3}(h_2\nu_{k+2}^2 + h_1\nu_{k+2} - Dh_2),$$
$$(k = 1, 2).$$

The coefficients ξ_1, …, ζ_1, E_0, E_1, and E_2 are given in Appendix A. In addition,

$$f_2 = \eta_2 L \mp \sqrt{E_2},$$
$$f_1 = 16E_2\zeta_1[(\xi_1+2\xi_2+\xi_3)L^2 - c_1] + 2E_2\eta_2^2L^2,$$

$$h_2 = \eta_1 L \mp \sqrt{E_2}, \quad h_1 = 16E_2\zeta_1(\xi_3 L^2 - c_1) + 2E_2\eta_1^2L^2,$$

$$\nu_{1,2} = E_1 + E_2 L \pm \sqrt{E_2}\sqrt{E_2L^2 + 2E_1L + E_0},$$

$$\nu_{3,4} = E_1 \pm \sqrt{E_0E_2}, \quad E_0E_2 > 0,$$

$$u_{1,2} = \frac{1}{2}(-k_1 \pm \sqrt{k_1^2 - 4k_0}),$$

$$u_{3,4} = \frac{1}{2}(-e_1 \pm \sqrt{e_1^2 - 4e_0}),$$

$$e_1 = \frac{\alpha_3}{2} - \sqrt{p_2}, \quad e_0 = \frac{y_1}{2} - \frac{p_1}{2\sqrt{p_2}},$$

$$k_1 = \frac{\alpha_3}{2} + \sqrt{p_2}, \quad k_0 = \frac{y_1}{2} + \frac{p_1}{2\sqrt{p_2}},$$

$$p_2 = \frac{\alpha_3^2}{4} - \alpha_2 + y_1, \quad p_1 = \frac{\alpha_3}{2}y_1 - \alpha_1, \quad p_0 = \frac{1}{4}y_1^2 - \alpha_0.$$

Here, y_1 is one of the real roots of the cubic equation

$$y_1^3 - \alpha_2 y_1^2 + (\alpha_1\alpha_3 - 4\alpha_0)y_1 - \alpha_3^2\alpha_0 + 4\alpha_0\alpha_2 - \alpha_1^2 = 0$$

or $p_1^2 - 4p_0p_2 = 0$.

In addition, the following conditions are satisfied:

$$\alpha_1 < 0, \quad \alpha_3 > 0, \quad \alpha_0 > 0, \quad \alpha_2 > 0, \quad k_1 > k_0 > e_0 > 0,$$

$$e_1 < 0, \quad e_1^2 - 4e_0 > 0, \quad k_1^2 - 4k_0 > 0, \quad p_2 > 0,$$

$$s_1 = \frac{u_4-u_3}{u_4-u_2}, \quad s_2 = s_1\frac{u_2}{u_3}, \quad s_3 = \gamma_1, \quad s_4 = \gamma_2,$$

$$1 + s_n > 0, \quad \gamma_n = s_1\frac{\nu_n - u_2}{\nu_n - u_3},$$

$$u_2 < u_1 < u_4 \le u < u_3, \quad 1 + \gamma_n > 0, \quad n = 1, 2, 3, 4,$$

$$I_0 = W_0 + W_1u_2 + \frac{W_2}{u_2} + \frac{W_3}{\nu_1-u_2} + \frac{W_4}{u_2-\nu_2},$$

$$J_0 = S_0 + \frac{S_1}{\nu_1-u_2} + \sum_{n=2}^{4}\frac{S_n}{u_2-\nu_n},$$

$$M = \frac{\pm\sqrt{E_2}(u_3-u_2)}{\sqrt{(u_3-u_1)(u_4-u_2)}}\frac{1}{E_2N},$$

$$I_1 = M[(\eta_2+\eta_1)d_2 + 8\zeta_1(\xi_1+2\xi_2)],$$

$$I_2 = M\frac{D}{u_2u_3}[(\eta_2+\eta_1)d_0 + 8\zeta_1(\xi_1+2\xi_2)],$$

$$I_{k+2} = \frac{2E_2M}{\nu_1-\nu_2}\frac{1}{(\nu_k-u_2)(\nu_k-u_3)}(f_2\nu_k^2 + f_1\nu_k - Df_2),$$

$$J_k = -I_{k+2}, \quad (k = 1, 2),$$

$$J_{n+2} = (-1)^n\frac{2E_2M}{\nu_4-\nu_3}\frac{1}{(\nu_{n+2}-u_2)(\nu_{n+2}-u_3)}$$
$$\times(h_2\nu_{n+2}^2 + h_1\nu_{n+2} - Dh_2),$$
$$(n = 1, 2).$$

The quantities W_k, S_k and f_k, h_k (k = 1, 2) were defined above.

$$D_0 = \frac{1}{\sqrt{1+w_n}}\arctan(\sqrt{1+w_n}\tan\varphi), \quad T_0 = \varphi,$$

$$1 + w_n > 0, \quad w_n = \{s_n, \gamma_n\}, \quad D_{s+1} = \frac{1}{w_n}(T_s - D_s),$$

$$T_{s+1} = \frac{2s+1}{2s+2}T_s - \frac{1}{2s+2}\cos\varphi\sin^{2s+1}\varphi.$$

Translated by A. Kozlenkov

Astronomy Letters, Vol. 27, No. 2, 2001, pp. 65–73. Translated from Pis'ma v Astronomicheskiĭ Zhurnal, Vol. 27, No. 2, 2001, pp. 83–93.

Nuclear Activity of NGC 4151 as Inferred from *UBVRI* Observations in 1989–2000

V. T. Doroshenko[1]*, V. M. Lyuty[1], N. G. Bochkarev[1], V. V. Vlasyuk[2], V. P. Mikhaĭlov[2], O. I. Spiridonova[2], K. N. Grankin[3], O. V. Ezhkova[3], and S. Yu. Mel'nikov[3]

[1] *Sternberg Astronomical Institute, Universitetskiĭ pr. 13, Moscow, 119899 Russia*
[2] *Special Astrophysical Observatory, Russian Academy of Sciences, Nizhniĭ Arkhyz, Stavropol kraĭ, 357147 Russia*
[3] *Ulugbek Astronomical Institute, Academy of Sciences of Uzbekistan, Astronomicheskaya ul. 33, Tashkent, 700052 Uzbekistan*

Received July 20, 2000

Abstract—We present our broadband *UBVRI* observations of the nucleus of the Seyfert galaxy NGC 4151 from 1989 until 2000 at three astronomical observatories: the Crimean Station of the Sternberg Astronomical Institute, the Special Astrophysical Observatory in the Caucasus, and the Maidanak Observatory of the Ulugbek Astronomical Institute in Uzbekistan. All data have been reduced to a single system and are given for an $A = 27''.5$ aperture. Regular *R* and *I* observations show that the pattern of optical variability is the same in all bands; the relative variability amplitude decreases from *U* to *V*, but it is even slightly larger in *R* than in *V*. The variability amplitude of the component fluctuating on time scales of several months is proportional to the *UBV* flux from the component varying on times scales of several years. The correlation between the slow and rapid components significantly weakens in the red, and no correlation has been found between the flux from the slow component and the amplitude of the rapid component in *R*. The color characteristics correspond to the recombination radiation from an optically thick plasma beyond the Balmer limit. © *2001 MAIK "Nauka/Interperiodica".*

Key words: *active galactic nuclei, quasars, and radio galaxies*

INTRODUCTION

The Seyfert galaxy NGC 4151 is one of the most interesting and best studied galaxies with active nuclei. Substantial nuclear variability of NGC 4151 has been found in the entire electromagnetic spectrum. Since much observational data are available on NGC 4151, this galaxy is used to test various theoretical models. It is therefore of great interest to systematically supplement the existing database with new observations.

Over the last 30 years, many observations of the NGC 4151 nucleus have been carried out with a *UBV* photometer at the Crimean Station of the Sternberg Astronomical Institute (SAI). Here, we present our magnitude estimates for this galaxy not only in *UBV*, but also in the near infrared (Johnson's *RI* bands) made in 1989–1999 at three observatories: the Crimean Station of the SAI (below called Crimea for short), the Maidanak Observatory of the Ulugbek Astronomical Institute in Uzbekistan (Maidanak), and the Special Astrophysical Observatory in the Northern Caucasus (SAO). All data were reduced to a single system. We briefly describe the telescopes and photometers used during the observations, CCD image processing techniques, and our results. We also analyze these observations.

* E-mail address for contacts: doroshen@sai.crimea.ua

OBSERVATIONS

Most of the data in the wavelength range 3500 to 7000 Å with broadband filters were obtained by using photometers with photomultipliers as the detectors. However, the wide use of CCD-based solid-state light detectors in astronomical observations has allowed the photometric variability of extragalactic objects to be investigated not only with relatively small telescopes (D = 40–60 cm), but also over a broader spectral range up to 10 000 Å. With the application of CCD detectors, it has become possible to obtain reliable results for objects fainter than $14–15^m$, which seemed problematic when using photoelectric methods of observations.

Crimea

The Crimean observations before 1997 had been carried out with a photon-counting *UBV* photometer attached to a 60-cm Zeiss telescope in an instrumental system close to Johnson's standard photometric system [see Lyuty and Doroshenko (1999) for details].

A photometer with a thermoelectrically cooled ST-6 375×242 CCD camera was put into operation in 1997. The final image scale on the detector with a reducing lens is $1''.8$ per pixel. The instrumental field of view is $9'.5 \times 7'.2$. The photometer is equipped with broadband filters that reproduce a *UBVRI* system close to Johnson's standard photometric system.

1063-7737/01/2702-0065$21.00 © 2001 MAIK "Nauka/Interperiodica"

Maidanak

The observations at the High-Altitude Maidanak Observatory in Uzbekistan were performed with two 60-cm Zeiss reflectors and a 48-cm reflector (AZT-14). All three telescopes were equipped with identical pulse-counting photometers. The detector was a photomultiplier (FEU-79). The measurements were made with standard *UBVR* filters in Johnson's system. The working apertures were 24″.2, 27″.5, and 26″ in diameter for the two Zeiss-600 and AZT-14 telescopes, respectively. In order to determine the atmospheric extinction coefficients and the color coefficients of transformation to Johnson's standard photometric system, we observed about ten standard stars from the list of Landolt (1983) on each night. The photometric reduction was performed by using the procedures developed by Nikonov (1976). The observational errors were no larger than $0^m.035$ in *U* and no larger than $0^m.015$ in *B*, *V*, and *R*.

SAO

The need for photometric studies of active extragalactic objects at SAO at a heavy workload of the 1-m telescope stimulated the creation of a photometric complex based on the Zeiss-600 telescope, which had been rarely used before 1996. The properties of this telescope in combination with stringent requirements for the guiding quality necessitated the creation of an automatic photometer with off-axis guiding and a telescope control system that would allow automatic telescope guiding during an exposure. Such a photometric complex had been constructed by mid-1997. Using a liquid-nitrogen-cooled low-noise 1040 × 1160 CCD detector in combination with the ability to take exposures up to 30–40 min without any deterioration of the image quality because of guiding allowed stable direct images with a magnitude limit up to 22^m to be obtained and $18–19^m$ objects to be photometered with a $0^m.05$ accuracy (Amirkhanyan *et al.* 1997).

The detector image scale is 0″.45 per pixel, and the full instrumental field of view is 7′.5 × 8′.5. A small-sized CCD array is used as the guider detector; it is sensitive enough to perform reliable guiding with $10–11^m$ stars at a mean integration time of 2–3 s. Guiding stars are chosen in a ~1° field by using a two-coordinate slide in polar coordinates.

In order to speed up the signal readout from the detector and to reconcile the pixel resolution with the seeing, we used a procedure for the signal addition on the detector by pairs in each coordinate during our observations. As a result, the data sampling was 0″.9 per pixel, in good agreement with the mean seeing (1″.5–2″.5).

The photometer is equipped with a set of broadband *BVRI* filters. The instrumental photometric system differs only slightly from Johnson–Cousins' international system used in CCD photometry. We derived equations for transformation of the instrumental system to the international system by observing several star fields with measured *UBVRI* magnitudes for many stars.

Apart from the objects under study, we took exposures of the bright dawn and dusk sky and frames with only an electronic zero and dark current during our CCD observations.

DATA REDUCTION TECHNIQUE

The procedure for reducing the photoelectric observations performed over almost half a century is standard and requires no special explanation.

The reduction technique for CCD observations differs markedly from the methods of reducing photoelectric observations. However, stable image processing methods have also been developed over the ten years of using CCD detectors in astronomy, which have some peculiarities at each observatory, though. We processed our CCD images by using the software developed at SAO. Its main features were described by Vlasyuk (1993).

Primary Data Reduction

The primary image processing involves subtracting a dark frame from the original image averaged over several integrations and dividing the result by an image with a uniformly illuminated field. These procedures enable us to remove most of the so-called "hot spots," i.e., pixels with an enhanced thermal charge generation, and to allow for a nonuniform detector sensitivity from pixel to pixel. Uniformly illuminated fields in each of the bands can be produced both by integrating the signal from a sufficiently bright dusk or predawn sky and from a uniformly illuminated screen in the tower.

In general, the sky-background nonuniformity in the preprocessed images does not exceed a few percent and mainly results from stray light around bright stars and in the photometer itself. For the required accuracy of photometrically measuring the object under study and reference stars to be achieved, these deviations must be eliminated. To this end, we broke down the entire image into 5–7″ fragments and estimated the local background in them. The possible additional contribution from field objects to a fragment is inferred from the statistical properties of its signal. If the inference is positive, the current fragment is excluded from the subsequent analysis. This procedure yields a compressed image with "clean" background values and with values marked as "polluted." Smoothing this image and filling the "polluted" values by fitting the adjacent "clean" values yield a fairly smooth image. Using the bilinear interpolation method, we reconstruct the array of the original size from this compressed image, which is assumed to be the true background image. Using adjustment parameters, such as, for example, the size of the original fragment and the deviation level in a statistical analysis, allows us to cope with residual back-

ground nonuniformities. When extended sources whose images occupy much of the frame (as, for example, NGC 4151) are measured, the part occupied by the galaxy image is separated from the frame and is considered "polluted" (in the above terminology), while the smoothed background is constructed from the remaining part of the image, as described above.

CCD Photometry of Objects

The choice of method for photometric measurements of the objects under study was determined by two factors: the need to measure both extended and starlike objects and the need to allow for the possible distortions of the true values due to cosmic-ray particle hits and residual detector defects.

We used the method that proved to be good in photographic data reduction after slightly adjusting the basic parameters. It is based on signal integration in annuli of increasing size with a fixed center at the barycenter of the measured object. By analyzing the distribution of values in each annulus, we can identify and remove distorted values. The integration procedure in increasing annuli terminates when the total flux, which is compared with the dispersion of the background values near the measured object, does not increase in the aperture. Having analyzed the brightness distribution in the annuli, apart from the object's total flux and sizes, we determined its accurate coordinates, shape, and fluxes in the apertures chosen. The procedures described above are applied both to the sources under study and to the reference objects used for photometric calibration.

Calibration of the Instrumental System

As was already mentioned above, in order to convert the instrumental *ubvri* system for CCD detectors to Johnson's ($UBVR_JI_J$) or Cousins' (R_CI_C) standard international system, star fields with small angular sizes containing a sufficient number of stars with good photometric measurements should be observed.

In Crimea, we used the open cluster M 67 for this purpose, which was observed on five nights during 1998–1999. The seeing on different nights ranged from $1\farcs5$ to $3''$. In the observed $4' \times 4\farcm5$ region, we measured ~20 stars of different spectral types and different brightness from $V = 9\fm70$ to $V = 14\fm34$. We estimated the standard *UBVRI* magnitudes of these stars by averaging data from several published sources (Johnson and Sandage 1955; Eggen and Sandage 1964; Schild 1983, 1985; Joner and Taylor 1990; Chevalier and Ilovaisky 1991; Gilliland *et al.* 1991; Montgomery *et al.* 1993; Anupama *et al.* 1994). Since the methods of differential photometry are mainly used to process CCD frames, we measured cluster stars relative to one of the stars at the frame center when calibrating the system. We sought for a linear relation by least squares:

$$\Delta V_{BV} = C_1\Delta v + C_2\Delta(b-v),$$
$$\Delta V_{VR} = C_1\Delta v + C_2\Delta(v-r),$$
$$\Delta(B-V) = C_1\Delta(b-v),$$
$$\Delta(U-B) = C_1\Delta(u-b),$$
$$\Delta(V-R) = C_1\Delta(v-r),$$
$$\Delta(V-I) = C_1\Delta(v-i).$$

The broadband *R* and *I* filters used in Crimea reproduce Johnson's system better. Since the *R* and *I* magnitudes of stars in many published sources are given in Cousins' system, they were first reduced to Johnson's system by using equations from Landolt (1983). As a result, we obtained the following equations for the transformation of instrumental magnitudes to Johnson's standard system:

$$\Delta V_{bv} = 0.987[0.005]\Delta v + 0.083[0.019]\Delta(b-v),$$
$$\Delta V_{vr} = 0.984[0.005]\Delta v + 0.088[0.018]\Delta(v-r),$$
$$\Delta(B-V) = 0.777[0.012]\Delta(b-v),$$
$$\Delta(U-B) = 0.995[0.047]\Delta(u-b),$$
$$\Delta(V-R_J) = 0.809[0.016]\Delta(v-r),$$
$$\Delta(V-I_J) = 1.050[0.008]\Delta(v-i).$$

Here, *ubvri* and *UBVRI* refer to instrumental magnitudes and to the standard system, respectively. The errors in the coefficients are given in square brackets.

The *BVRI* calibration of the SAO CCD photometer differs only in details. For example, the star fields in the clusters NGC 2419, NGC 4147, NGC 7006, and M 92 were used for calibration. According to these observations, the instrumental photometric system differs from Johnson (*BV*)–Cousins' (*RI*) international system by no more than 5–7%.

RESULTS

Thus, all observations at the three observatories (the Crimean Station of the SAI, SAO, and the Maidanak Observatory) and the subsequent data reduction yielded several series of internally homogeneous *UBVRI* magnitude estimates for the nuclear region of NGC 4151. Our next step was to obtain a single data series as homogeneous as possible. The point is that the apertures used during the Maidanak, SAO, and Crimean measurements were slightly different. Consequently, the actual contribution of the galaxy's stellar radiation to each of these series was different, which made the combined series in each band inhomogeneous. In addition, despite the reduction of all instrumental photometric systems to Johnson's standard system, some differences remained in practice. This could also result in inhomogeneity of the combined data series. So, we

reduced the problem of producing a homogeneous *UBV* series to calculating the coefficients of linear regression between the Crimean series as the most complete and homogeneous one, on the one hand, and all the remaining series, on the other hand. The magnitudes were first transformed to fluxes. The most reliable data intercalibration is made if there are many common dates of observations between different observatories.

We encountered some difficulties when matching the *R* fluxes, because there were large breaks in the Maidanak observations started in 1989 and because the Crimean and Caucasian *R* observations began only in 1997 and 1998, respectively. On the other hand, the galaxy's mean brightness varied nonlinearly in 1989–1999, and, consequently, a linear interpolation could not be directly used to join these data. To combine them, we used the *R* measurements during 1989–1996 published by Merkulova and Metik (1993, 1995, 1996) and unpublished data on the continuum flux near $H\alpha$ in 1991–1998, which were kindly made available to us by S.G. Sergeev. These two series helped us combine all *R* observations into a single series. From tactical considerations (because systematical observations of this galaxy will also be subsequently carried out in Crimea), we took the observations at the Crimean Station of the SAI with the $A = 27''.5$ aperture as the basis.

In the *I* band, we have only CCD observations at the Crimean Station of the SAI (December 1997–October 1999) and the published observations by Merkulova and Metik from February 1989 until June 1996. However, these two series cannot be unambiguously joined, because they do not coincide in time.

The nightly mean combined *UBVRI* magnitudes of NGC 4151 in the $A = 27''.5$ aperture are given in the table[1]. The observatories are abbreviated as follows: SAIp and SAIc for the Crimean photoelectric and CCD observations, respectively; and Mdn and SAO for the Maidanak photoelectric and SAO CCD observations, respectively.

ANALYSIS

Figure 1 shows the *UBVRI* light curves of NGC 4151 as observed from 1989 until early 2000. We see that, in 1989–1996, the nuclear brightness rose against the background of significant variations whose amplitude reached $0^m.8$ in *U*, $0^m.5$ in *B*, and $0^m.3$ in *VRI* during some events (on time scales of several months). After 1996, the brightness started to gradually decline together with shorter time variations of approximately the same amplitude as that during the brightening. The entire episode of brightness rise and decline in 1989–2000 [called cycle B by Lyuty and Doroshenko (1999)] appears as an extraordinary event against the background of previous (cycle A) photoelectric observations of the galactic nucleus, which are shown for *U* in Fig. 2 for comparison. We see from Figs. 1 and 2 that the nuclear brightness in all bands is currently approaching its minimum value during the lowest activity in 1985–1989. The preceding activity cycle lasted much longer (>20 years), though its amplitude was much smaller than that of cycle B (1989–2000). Although the light curves in all bands are similar, note that the total amplitude of the slow component (in magnitudes) in *R* is larger than that in *V*. Since the number of *I* observations is insufficient, we cannot infer the total variability amplitude in this band.

For the brightness of the variable nuclear source itself to be analyzed, the contribution of the stellar radiation within the $A = 27''.5$ aperture must be eliminated. In *UBV*, we used the magnitude estimates for the stellar component from Lyuty and Doroshenko (1999) obtained from multiaperture photometry with $A = 27''.5$: $U_g = 12^m.99$, $B_g = 12^m.91$, and $V_g = 11^m.99$. To estimate the stellar contribution in *R* and *I*, we used multiaperture data from McAlary *et al.* (1983) and determined the magnitudes of the galaxy's stars with $A = 27''.5$: $R_c = 11^m.45 \pm 0^m.12$ and $I_c = 10^m.91 \pm 0^m.12$. A comparison of the *R* surface brightness distribution deduced from multiaperture observations with the surface brightness distribution measured from CCD observations (De Robertis *et al.* 1998) revealed excellent agreement between these distributions. Having subtracted the corresponding stellar fluxes from the observed fluxes in $A = 27''.5$, we obtained the variability of the central nuclear source in pure form.

Figure 3 shows temporal variations in the *UBVR* fluxes from the central source. The minimum fluxes from the nucleus are ~6–8 mJy in all *UBVR* bands. The maximum *UBV* fluxes are about 95–80 mJy; the peak *R* fluxes are considerably higher. The jaggedness of the light curve on its ascending and descending branches is virtually the same. In late 1999, the *U* and *B* fluxes almost reached their 1989 levels. However, the nucleus had not yet faded to its minimum level in *R*.

The assertion that the light curves for the nuclei of Seyfert galaxies exhibit at least two types of variability, a slow variability component on time scales of several years and a rapid component in the form of outbursts lasting for several months, has been universally accepted. Almost the entire history of research on the nuclear variability of Seyfert galaxies is associated with efforts to understand the relationship between these components. Do they differ in physical nature (in that case, there is no relationship between them) or are these variability components related (in that case, they may belong, for example, to the same source)?

Lyuty and Doroshenko (1999) assumed the light variations in the slow component (on time scales of several years) to be associated with the state of the accretion disk. If the more rapid light variations (on time scales of several months) are also associated with the processes in this disk, then the amplitude of the

[1] The table is published in electronic form only and is accessible via ftp cdsarc.u-strasbg.fr/pub/cats/J (130.79.128.5) or http://cdsweb.u-strasbg.fr/pub/cats/J.

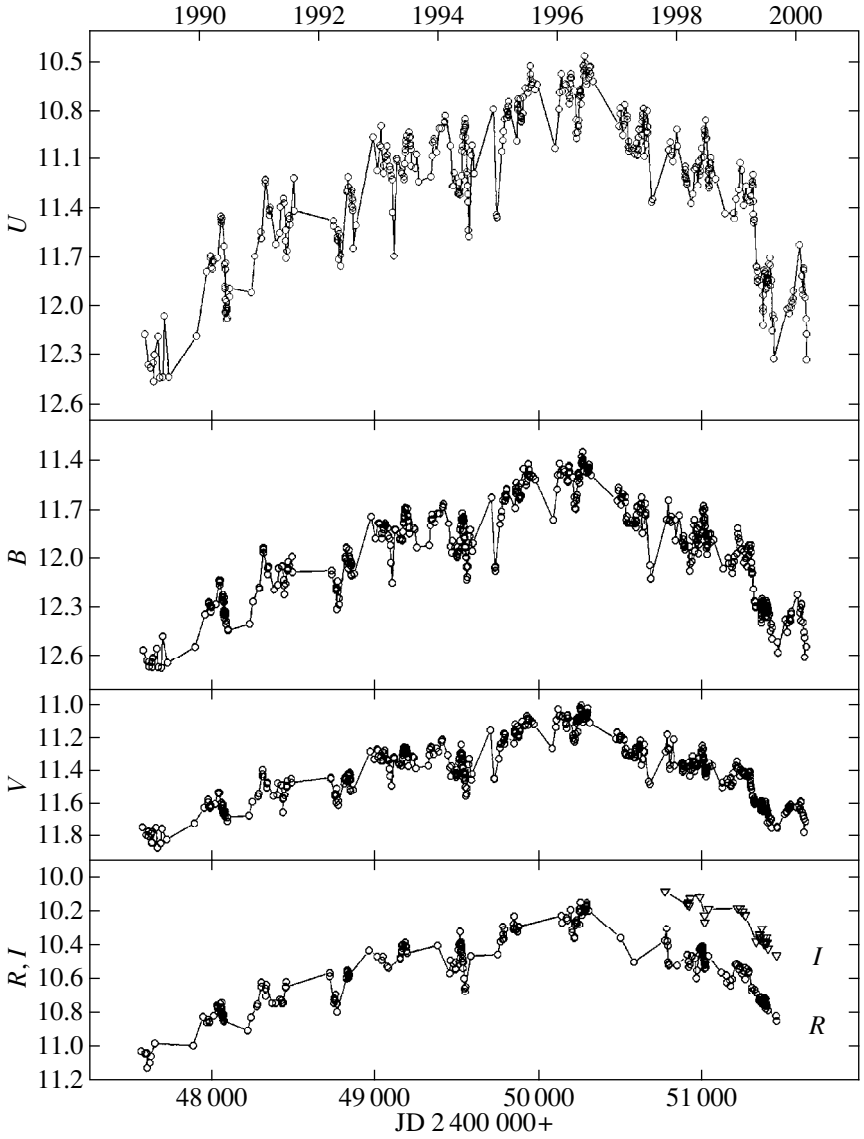

Fig. 1. *UBVRI* light curves of NGC 4151 in 1989–2000 with an $A = 27''.5$ aperture.

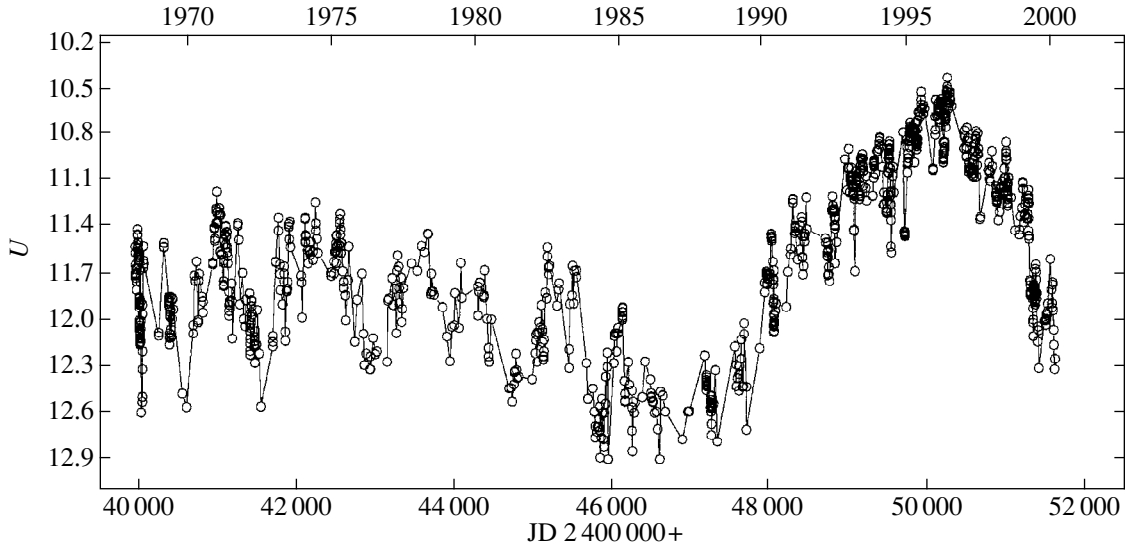

Fig. 2. Combined *U* light curve of NGC 4151 in 1968–2000 with $Å = 27''.5$.

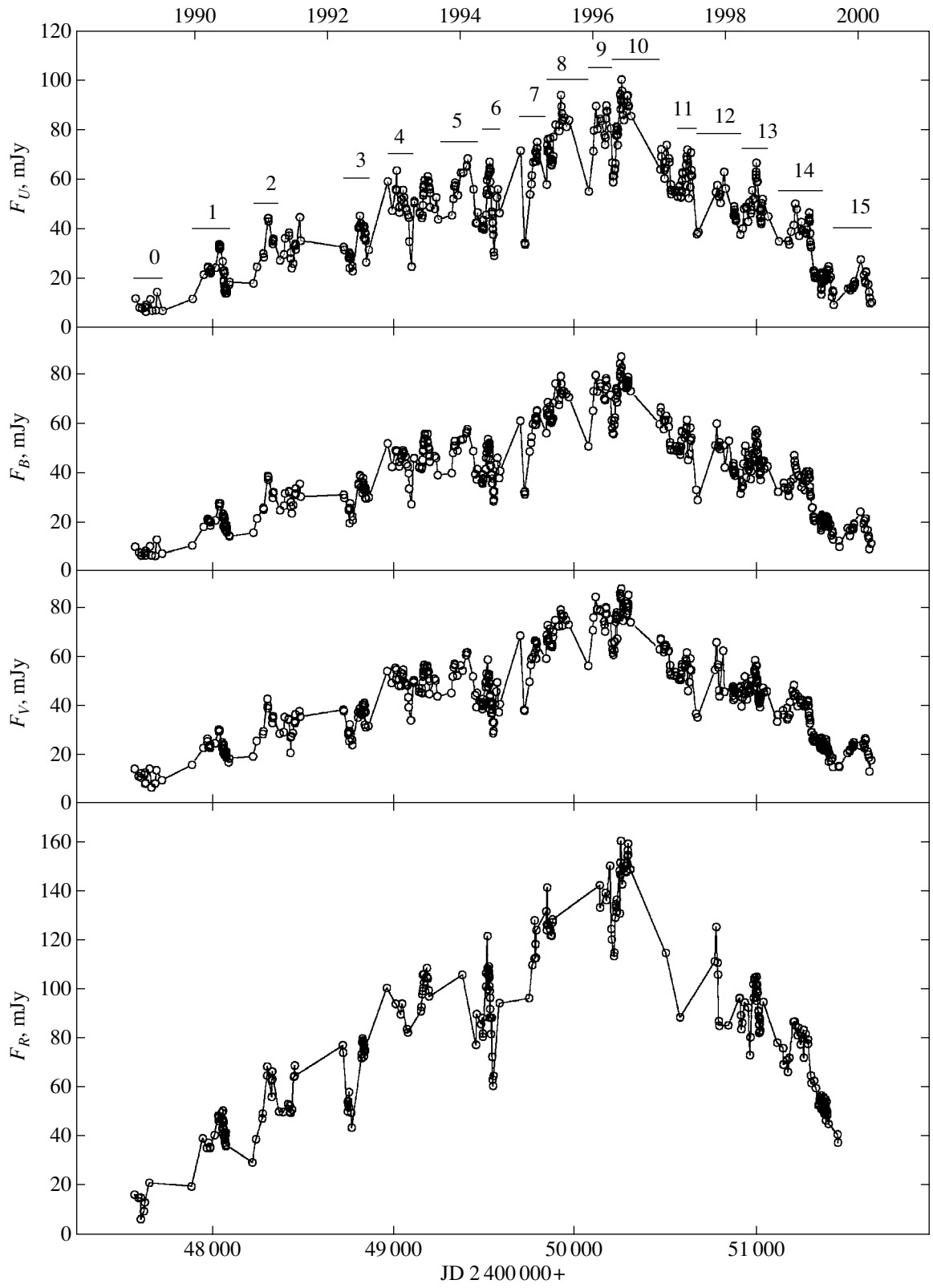

Fig. 3. *UBVR* light curves of the variable source in 1989–2000. The flux in the corresponding band is along the vertical axis. The intervals for individual events analyzed in the text with event numbers are indicated by horizontal bars.

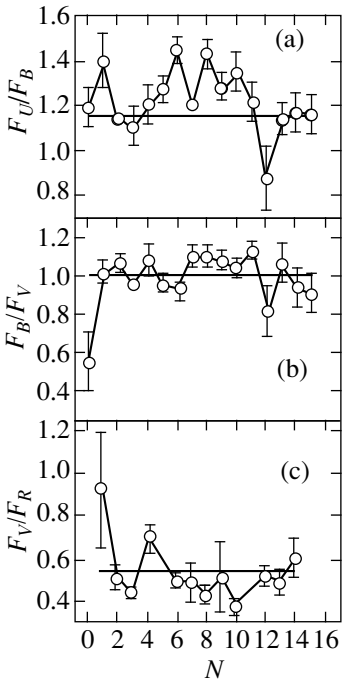

Fig. 4. Linear regression parameter a for the fluxes in two adjacent bands for individual events: (a) for the regression equation $F_U = aF_B + b$, (b) for the regression F_B/F_V, and (c) for the regression F_V/F_R. The event number is along the horizontal axis. The corresponding parameters averaged over the entire data set are indicated by dashed lines.

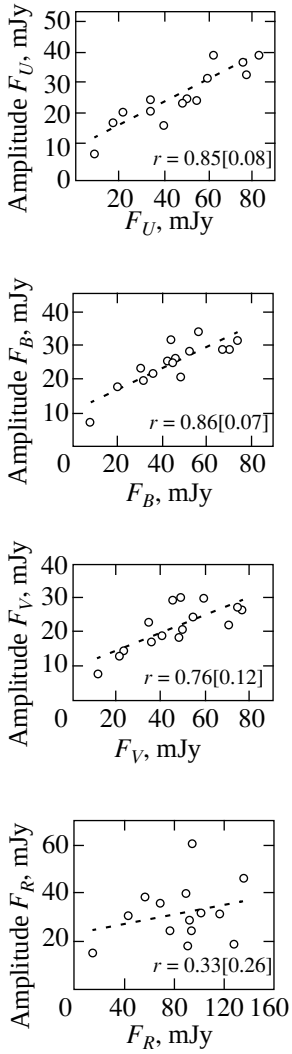

Fig. 5. Correlation between the variability amplitude during each individual event and the mean flux for *UBVR* (r is the correlation coefficient with its error).

more rapid variability can correlate with the brightness of the slow component. In order to test this assumption, we selected 16 small outbursts at different phases of the 11-year "superoutburst." The time intervals of these individual events are marked in the *U* light curve of the nucleus in Fig. 3 (from $N = 0$ to $N = 15$). For these events, we estimated the mean fluxes and variability amplitudes and analyzed flux–flux diagrams in all bands.

Our analysis of the flux–flux diagrams for individual events in the variable source over the entire period since 1989 shows (Fig. 4) that, within the limits of the observational errors, the slopes of the regression lines F_U/F_B, F_B/F_V, and F_V/F_R for all events are close to the mean value, with the possible exception of some events in *U* on the ascending branch of the light curve. This implies that, when the brightness changes from one event to another, the spectral energy distribution of the central variable source is generally constant in the *UBVR* range. Some difference between the free and zero terms in the regression equations is most likely attributable to small errors in the contribution of the underlying galaxy (from 2 to 19% for the bands from *U* to *R*).

On the other hand, the amplitude of outbursts on time scales of several months (in mJy) in *UBV* was found to correlate well with the mean flux during outburst: the brighter the nucleus, on the average, the more intense are its outbursts. This is not the case in *R*, as shown in Fig. 5. We cannot reach any definitive conclusions regarding the behavior in *I*, because the number of observations is insufficient. The coefficients of correlation between the amplitude and the mean flux during outbursts for *UBVR* are 0.85 ± 0.08, 0.86 ± 0.07, 0.76 ± 0.12, and 0.33 ± 0.26, respectively. Such an analysis for cycle A in *UBV* for 14 events on the same time scale revealed a correlation between the mean fluxes and amplitudes of outbursts in *U* ($r = 0.76 \pm 0.12$) and a less significant correlation in *B* and *V* ($r = 0.66 \pm 0.16$ and $r = 0.68 \pm 0.16$, respectively). It should be noted that the total amplitude of the slow variations in cycle A is half that in cycle B. On the one hand, this may be the reason why this correlation is less pronounced in *BV*, but, on the other hand, there may also be other objective factors that cause the correlation between the outburst amplitude and the mean flux during outburst to

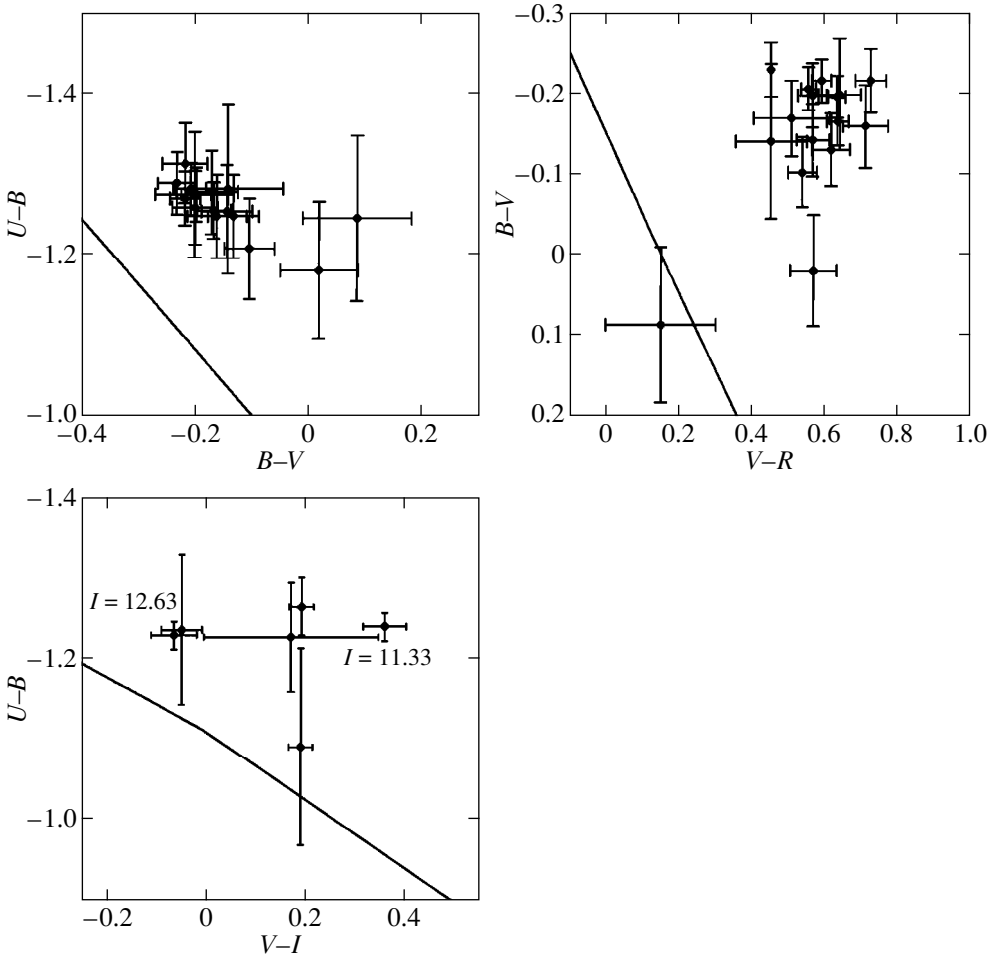

Fig. 6. (*U–B*)–(*B–V*) and (*B–V*)–(*V–R*) diagrams for the mean values during each event. The (*U–B*)–(*V–I*) diagram was constructed for six different *I* brightness states when the *I* brightness changed from $I = 11\overset{m}{.}20$ to $I = 13\overset{m}{.}13$ during 1997–2000. The solid line refers to synchrotron radiation.

gradually weaken from *U* to *V*. The flux fluctuations on time scales of several months appear to be actually related in some way to the slow (on time scales of several years) *UBV* flux variations.

Note that Lyuty and Oknyanskij (1987) previously found a similar correlation in *U* for cycle A while investigating outbursts with amplitudes $\Delta U > 0\overset{m}{.}3$. They also concluded that, the higher the mean level of the slow component, the larger the outburst amplitude in *U*; i.e., the outburst amplitude is modulated by the phase of the slow variations. Our data independently confirm this correlation in *U* for cycle A. For cycle B, it is seen in *UB* and *V*. However, a gradual weakening of this correlation from *U* to *V* and the absence of any correlation in *R* may imply that a different factor, which breaks the detected correlations for *UBV*, begins to dominate as one goes to the red spectral range. Such a factor can be the presence of another independent variable source, which shows up precisely in the near infrared and whose existence was hypothesized by Lyuty *et al.* (1998).

For the 14 events of cycle B under consideration, we constructed two-color (*U–B*)–(*B–V*) and (*B–V*)–(*V–R*) diagrams. The interstellar extinction toward and inside the galaxy was discussed by Lyuty and Doroshenko (1999), who assumed it to be $A_v = 1^m$. We corrected the colors for this extinction when constructing the two-color diagrams. Since our *I* observations are few, we combined the *I* magnitudes into six groups in order of declining brightness and included the corresponding *U–B* and *V–I* colors in the (*U–B*)–(*V–I*) diagram. The diagrams are shown in Fig. 6. It follows from an analysis of the diagrams that the points corresponding to the colors of the NGC 4151 nucleus lie above the line for synchrotron radiation and a blackbody. A comparison of these diagrams with the diagrams for different types of radiation for Chalenko (1999) leads us to conclude that the colors of the NGC 4151 nucleus most likely correspond to the radiation from an optically thick plasma beyond the Balmer limit.

CONCLUSION

We have presented our observations of the nucleus of the Seyfert galaxy NGC 4151 from 1989 until 2000

at three astronomical observatories: the Crimean Station of the SAI, the Special Astrophysical Observatory in the Northern Caucasus, and the Maidanak Observatory of the Ulugbek Astronomical Institute in Uzbekistan. All data were reduced to a single system and are given for an $A = 27''.5$ aperture. As a result, we were able to obtain a homogeneous 10-year-long series of *UBVRI* magnitude estimates for the nucleus. Adding *RI* observations shows that the pattern of optical variability in all bands is the same; the relative variability amplitude decreases from *U* to *V*, but it is larger in *R* than in *V*. The variability amplitude of the component fluctuating on times scales of several months is proportional to the *UBV* flux from the component varying on time scales of several years. The correlation between the slow and rapid components significantly weakens in *R*, in which no correlation was found between the flux from the slow component and the amplitude of the rapid component. The color properties of the radiation correspond to the recombination radiation from an optically thick plasma beyond the Balmer limit. This is consistent with the previous assumption (Lyuty and Doroshenko 1999) that the increase in optical luminosity of the nucleus from 1989 until 1996 resulted from an increase in the size of the accretion disk around a massive black hole at the center of NGC 4151. The fact that some peculiar features in the behavior of the variable source (for example, the absence of any correlation between the variability amplitude of the fluctuating component and the flux from the slow component) show up in *R* may be attributable to the effect of an intermediate source, which manifests itself in the wavelength range 0.5–1 μm. This source was investigated by Lyuty *et al.* (1998).

ACKNOWLEDGMENTS

We wish to thank S.G. Sergeev (Crimean Astrophysical Observatory, Ukraine), who provided data on the continuum near $H\alpha$, which helped us to tie together the observations made at different observatories. We also wish to thank S.D. Yakubov, L.N. Berdnikov, M.A. Ibragimov, and V.B. Kondrat'ev for help with the Maidanak observations. This study was supported in part by the INTAS Foundation (grant no. 96-0328) and the Russian Foundation for Basic Research (project no. 97-02-17 625).

REFERENCES

1. V. R. Amirkhanyan, N. A. Vikul'ev, V. V. Vlasyuk, and D. A. Stepanyan, Otchet SAO (1997), 38 (1998).
2. G. C. Anupama, A. K. Kembhavi, T. P. Prabhu, *et al.*, Astron. Astrophys., Suppl. Ser. **103**, 315 (1994).
3. N. N. Chalenko, Astron. Zh. **76**, 529 (1999) [Astron. Rep. **43**, 459 (1999)].
4. C. Chevalier and S. A. Ilovaisky, Astron. Astrophys., Suppl. Ser. **103**, 225 (1991).
5. M. M. de Robertis, K. Hayhoe, and H. K. C. Yee, Astrophys. J., Suppl. Ser. **115**, 163 (1998).
6. O. J. Eggen and A. R. Sandage, Astrophys. J. **140**, 130 (1964).
7. R. I. Gilliland, T. M. Brown, D. K. Duncan, *et al.*, Astron. J. **101**, 541 (1991).
8. H. L. Johnson and A. R. Sandage, Astrophys. J. **121**, 616 (1955).
9. M. D. Joner and B. J. Taylor, Publ. Astron. Soc. Pac. **102**, 1004 (1990).
10. A. U. Landolt, Astron. J. **88**, 439 (1983).
11. V. M. Lyuty and V. T. Doroshenko, Pis'ma Astron. Zh. **25**, 403 (1999) [Astron. Lett. **25**, 341 (1999)].
12. V. M. Lyuty and V. L. Oknyanskij, Astron. Zh. **64**, 465 (1987) [Sov. Astron. **31**, 245 (1987)].
13. V. M. Lyuty, O. G. Taranova, and V. I. Shenavrin, Pis'ma Astron. Zh. **24**, 243 (1998) [Astron. Lett. **24**, 199 (1998)].
14. Ch. W. McAlary, R. A. McLaren, R. J. McGonegal, and J. Maza, Astrophys. J., Suppl. Ser. **52**, 341 (1983).
15. N. I. Merkulova and L. P. Metik, Izv. Krym. Astrofiz. Obs. **87**, 135 (1993).
16. N. I. Merkulova and L. P. Metik, Izv. Krym. Astrofiz. Obs. **90**, 178 (1995).
17. N. I. Merkulova and L. P. Metik, Astron. Astrophys. Trans. **10**, 295 (1996).
18. K. A. Montgomery, L. A. Marschall, and K. A. Janes, Astron. J. **106**, 181 (1993).
19. V. B. Nikonov, Izv. Krym. Astrofiz. Obs. **54**, 3 (1976).
20. R. E. Schild, Publ. Astron. Soc. Pac. **95**, 1021 (1983).
21. R. E. Schild, Publ. Astron. Soc. Pac. **97**, 824 (1985).
22. V. V. Vlasyuk, Astrofiz. Issled. (St. Petersburg) **36**, 107 (1993).

Translated by V. Astakhov

Astronomy Letters, Vol. 27, No. 2, 2001, pp. 74–80. Translated from Pis'ma v Astronomicheskiĭ Zhurnal, Vol. 27, No. 2, 2001, pp. 94–100.

A Photometric Study of the Polar Ring Galaxy UGC 5600

G. M. Karataeva[1]*, V. A. Yakovleva[1], V. A. Hagen-Thorn[1], and O. V. Mikolaĭchuk[2]

[1] *Astronomical Institute, St. Petersburg State University, Bibliotechnaya pl. 2, Petrodvorets, 198904 Russia*
[2] *Sterlitamak Teachers' Pedagogical Institute, Sterlitamak, Russia*

Received November 10, 1999; in final form, July 6, 2000

Abstract—We analyze our BVR_c photometry for UGC 5600, a candidate polar ring galaxy, obtained with the 6-m telescope. We have confirmed the existence of an inner polar ring and show that the outer ring-shaped structure represents spiral arms; i.e., UGC 5600 belongs to the rare class of gas-rich spiral galaxies with inner polar rings. © *2001 MAIK "Nauka/Interperiodica".*

Key words: *galaxies, groups and clusters of galaxies, intergalactic gas*

INTRODUCTION

In the catalog of polar ring galaxies (Whitmore *et al.*, 1990), the peculiar galaxy UGC 5600 was included in group B, composed of the most likely candidates for polar ring galaxies. Its main body is an amorphous $40'' \times 30''$ disk surrounded by an outer clumpy ring seen almost face-on. It is noted in the catalog that there is a narrow inner polar ring in a direction perpendicular to the major axis. The distance to the galaxy is 37.6 Mpc (for $H_0 = 75$ km s^{-1} Mpc^{-1}); the scale corresponding to this distance is 0.18 kpc in $1''$.

UGC 5600 is a member of a double system (VV 330). Its companion, the galaxy UGC 5609, lies at a distance of $1'.4$ (~15 kpc in projection onto the plane of the sky) to the southeast and has a radial velocity differing by ~100 km s^{-1} (de Vaucouleurs *et al.* 1991; RC3).

Spectroscopic observations (Reshetnikov and Combes 1994) show that the inner and outer rings are rich in gas. Along an axis close to the major axis of the inner ring, the emission lines extend to a distance of 6 kpc; the changes in radial velocity can be explained by rotation of the gaseous component around the galaxy's major axis. The radial-velocity curve along the major axis is complex in structure. The emission spectrum of the nuclear region in UGC 5600 is characteristic of giant H II complexes.

Since this galaxy has not been photometrically studied in detail, we have included it in our program of observations of polar ring galaxies under way at the Astronomical Institute of St. Petersburg State University.

* E-mail address for contacts: narka@gong.astro.spbu.ru

OBSERVATIONS AND DATA REDUCTION

Our photometric observations of UGC 5600 were preformed with the 6-m Special Astrophysical Observatory (SAO) telescope in Johnson's *B* and *V* and Cousins's R_c bands. A log of observations is given in Table 1. In all cases, the seeing was ~$2''$.

The detectors were two CCD arrays. The 1996 image was obtained using a K983 530×580 CCD (pixel size 18×24 μm) with a readout noise of 12–20 e$^-$. The pixel angular size was $0''.15 \times 0''.20$, and the field of view was $1'.3 \times 2'.0$. The 1997–1998 observations were carried out using an ISD017A 1050×1170 CCD array (pixel size 16×16 μm, or $0''.14 \times 0''.14$ in angular units) with a readout noise of 7 e$^-$. During each night, we observed standard stars from the lists by Landolt (1983) and Smith *et al.* (1991) for calibration. Mean transparency coefficients for the SAO were used to correct magnitudes for the atmosphere.

The observations were reduced at the Astronomical Institute of St. Petersburg State University using the ESO-MIDAS software package.

We added up the images in each of the color bands and used only the three total images in the subsequent analysis.

RESULTS AND DISCUSSION

The General Photometric Structure

A reproduction of the *B*-band image for the galaxy is shown in Fig. 1. The galaxy's main body, $40'' \times 30''$ in size, is surrounded by a broad outer ring. The inner boundary of the ring is blurred, whereas its outer boundary is sharp, as clearly seen in the photometric profiles along the major (Fig. 2) and minor (Fig. 3) axes

1063-7737/01/2702-0074$21.00 © 2001 MAIK "Nauka/Interperiodica"

Table 1. Observational data

Date	Band	Exposure, s	*z*, deg
Apr. 23, 1996	*V*	600	46
Feb. 4, 1997	*B*	400	35
	B	400	35
	V	600	35
	V	600	35
	R_c	600	35
June 24, 1998	*B*	600	56
	V	600	56
	R_c	300	56

Table 2. Basic parameters of UGC 5600

Distance	37.6 Mpc (0.18 kpc in 1″)
E_{B-V} (RC3)	0.00
B_t	14.45
V_t	13.87
$(R_c)_t$	13.35
$(B–V)_t$	0.58
$(V–R_c)_t$	0.52
$M_{0,B}$	–18.8
Main body: disk	
μ_0	19.7 *m* (arcsec)$^{-2}$
h	1 kpc
Outer ring: spiral arms	
$\overline{\mu}_B$	24.5 *m* (arcsec)$^{-2}$
B–V	0.3–0.4

(in both cases, the profiles were constructed by averaging within 1″). The outer size of the ring along its major axis (based on the $26^m/\square''$ isophote) is 80″, and its width is 15″–18″. The ring structure is clumpy, but the brightness differences are modest. The mean *B* surface brightness of the ring is $24\overset{m}{.}5/\square''$.

Structural features of the galaxy's main body are better seen on isophotes (Fig. 4). Since the structure of the galaxy is almost the same in all color bands, we consider only *B*-band isophotes.

The inner isophotes have a fairly regular elliptical shape with slight distortions on their southern side approximately to a surface brightness of $22\overset{m}{.}2/\square''$. Between the $22\overset{m}{.}2/\square''$ and $23\overset{m}{.}1/\square''$ isophotes, the brightenings attributable to the inner ring are observed in the east–west direction roughly parallel to the minor axis. (Note that a fairly red foreground star distorting the isophotes is projected onto the ring at a distance of 10″ to the west of the nucleus.) A more detailed analysis of the galaxy's image with different contrast levels shows that the brightenings can be traced up to the outer ring; they are lost further out. However, a brightening, which may be an extension of the ring, is observed in the western part at a distance of 20″.

For isophotes fainter than $23\overset{m}{.}5/\square''$, the axial ratio *b*/*a* of the ellipses inscribed in the isophotes increases (0.75 instead of 0.65), and the position angle of the ellipse major axis decreases (–10° instead of 0°). The changes clearly stem from the fact that these parameters characterize different structures (the main body and the outer ring) at different distances. Basic characteristics of UGC 5600 are listed in Table 2.

Integrated Characteristics

The galaxy's total asymptotic apparent magnitudes were determined by multiaperture photometry. We plotted the curves of brightness rise, which agree with the standard aperture relations for Scd galaxies from RC3. The following integrated characteristics were obtained for UGC 5600: $B_t = 14.45 \pm 0.1$, $(B–V)_t = 0.58 \pm 0.1$, $(V–R_c)_t = 0.52 \pm 0.1$. Our B_t is larger than that in RC3 ($B_t = 14.19$), but agrees well with that in UGC ($B_t = 14.4$). According to RC3, there is no Galactic interstellar extinction. The derived total colors of UGC 5600 are slightly redder than the mean colors for Scd galaxies, although this difference, given the error in the total color, is unlikely to be statistically significant. If, nevertheless, the reddening is assumed to be due to internal extinction in the galaxy, then the extinction in the *B* band is ~0.4, and we obtain $M_{0,B} = –18.8$ for the galaxy's absolute magnitude, typical of late-type spirals.

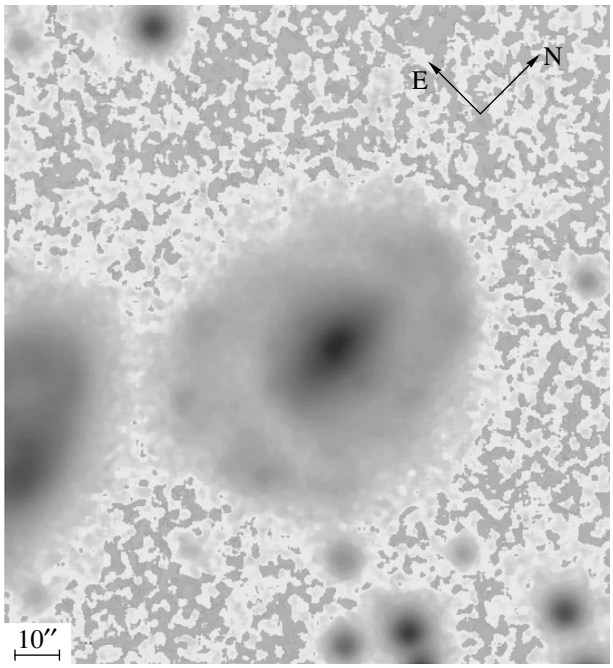

Fig. 1. A reproduction of the *B*-band image for UGC 5600.

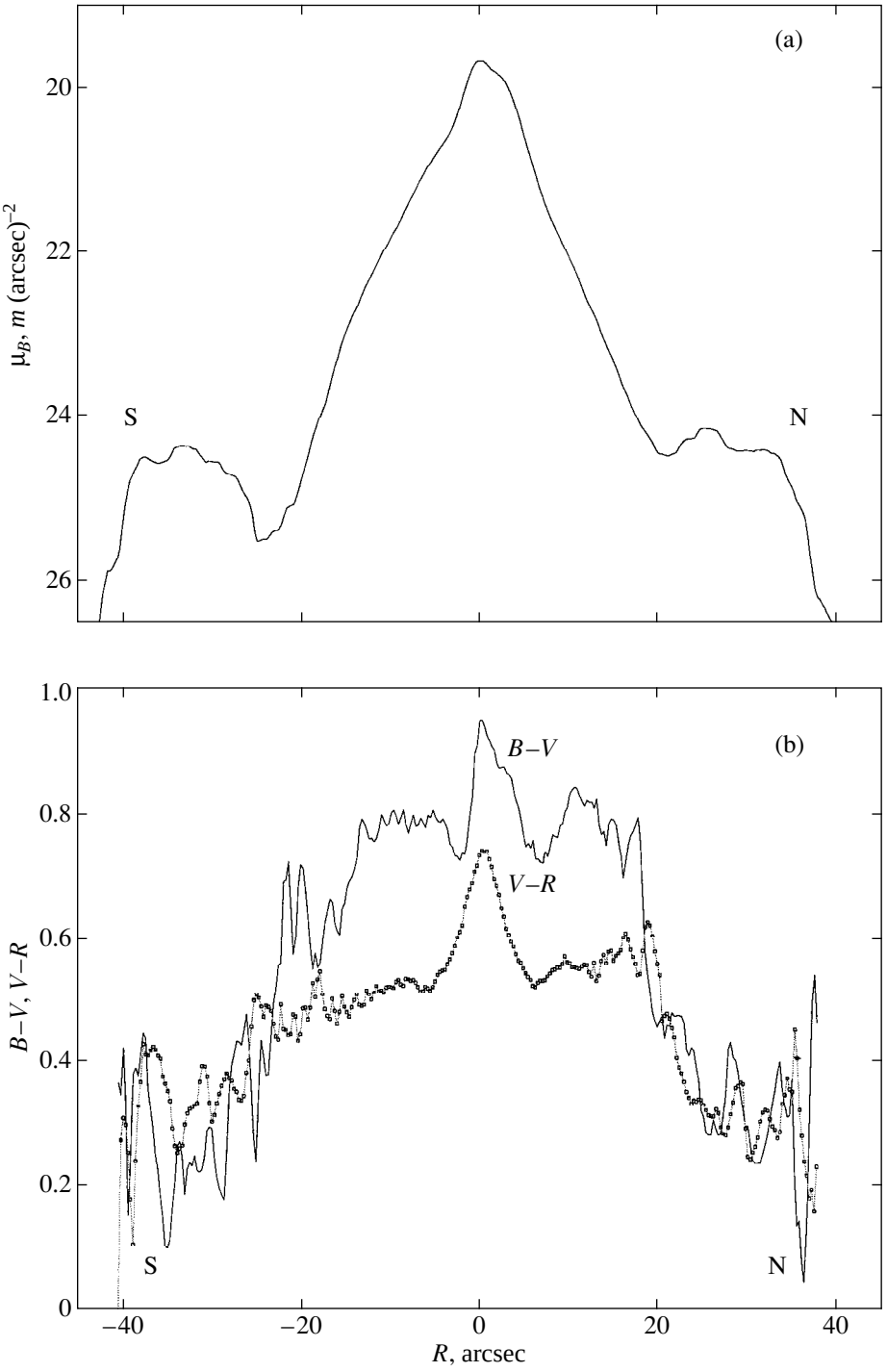

Fig. 2. The brightness (a) and color (b) distributions along the major axis.

The Brightness and Color Distributions

The photometric profiles of the galaxy's main body provide evidence for the absence of a bulge. In Fig. 5, the profile along the major axis is represented by a disk with the parameters $\mu_0 = 19.7$ m (arcsec)$^{-2}$ and $h = 5''$ (~1 kpc). The central brightness exceeds the mean for normal galaxies, $\mu_0 = 21.7$ m (arcsec)$^{-2}$ (Simien and de Vaucouleurs 1986), but is not unusual for interacting galaxies.

The blue regions at a distance of 5″ on both sides of the nucleus, to the south and to the north, are the most remarkable feature of the color distribution in UGC 5600 (see Fig. 6, which shows the B–V distribution). They are also clearly seen in Fig. 2 (especially in B–V). This

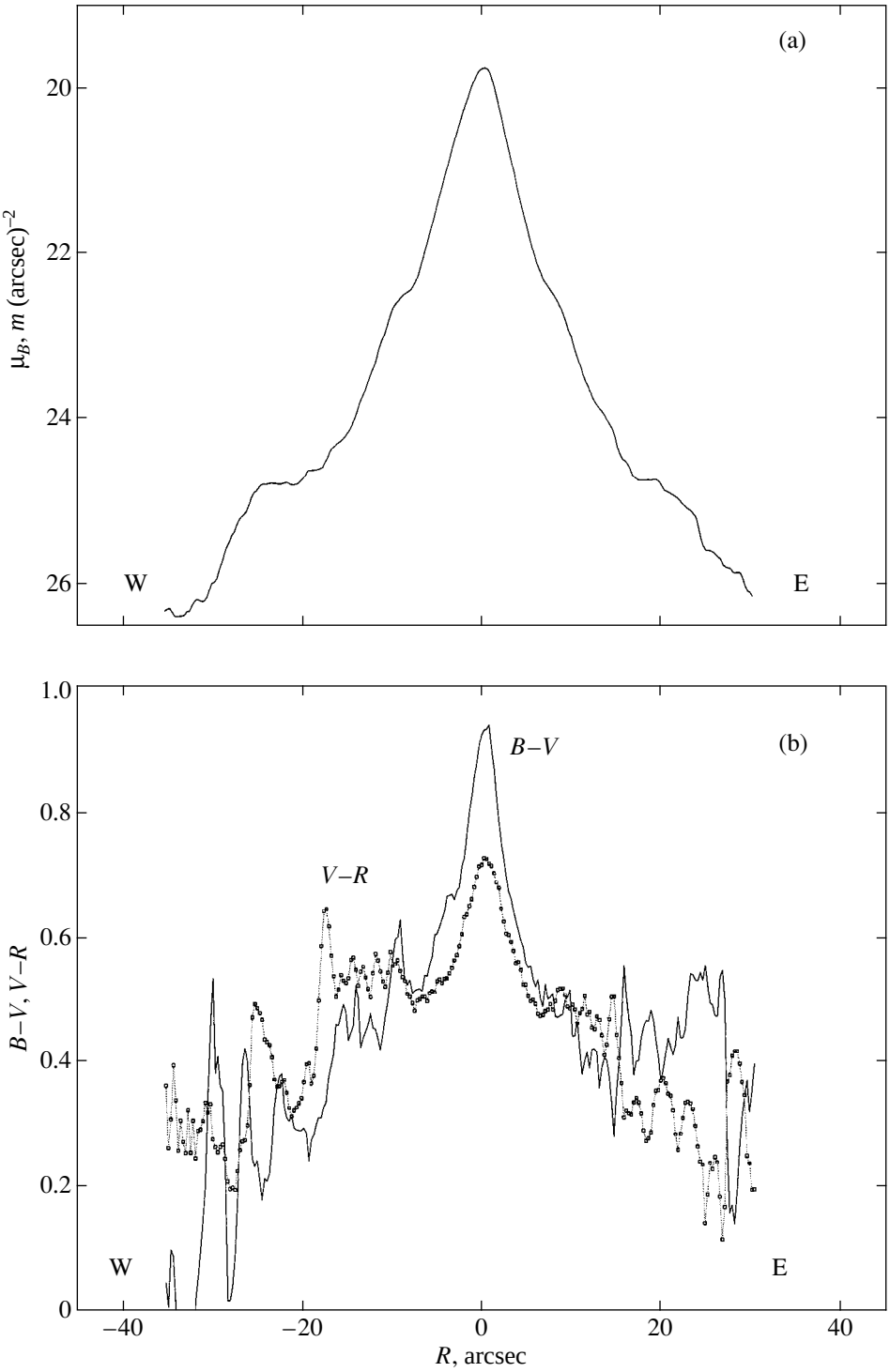

Fig. 3. The brightness (a) and color (b) distributions along the minor axis.

is evidently a manifestation of the blue inner ring, which is observed not exactly edge-on. The band is narrower and has sharp edges to the south of the nucleus and broader and more blurred to the north. We can assume that the blue ring is projected onto the red body of the galaxy to the north of the nucleus and is seen through the galaxy to the south, so that some features are blurred. That the internal extinction in UGC 5600 is modest follows from the two-color diagrams in Fig. 7: they do not show any noticeable elongation along the reddening line (several points in the lower right corner of Fig. 7a represent the nucleus itself, where redder

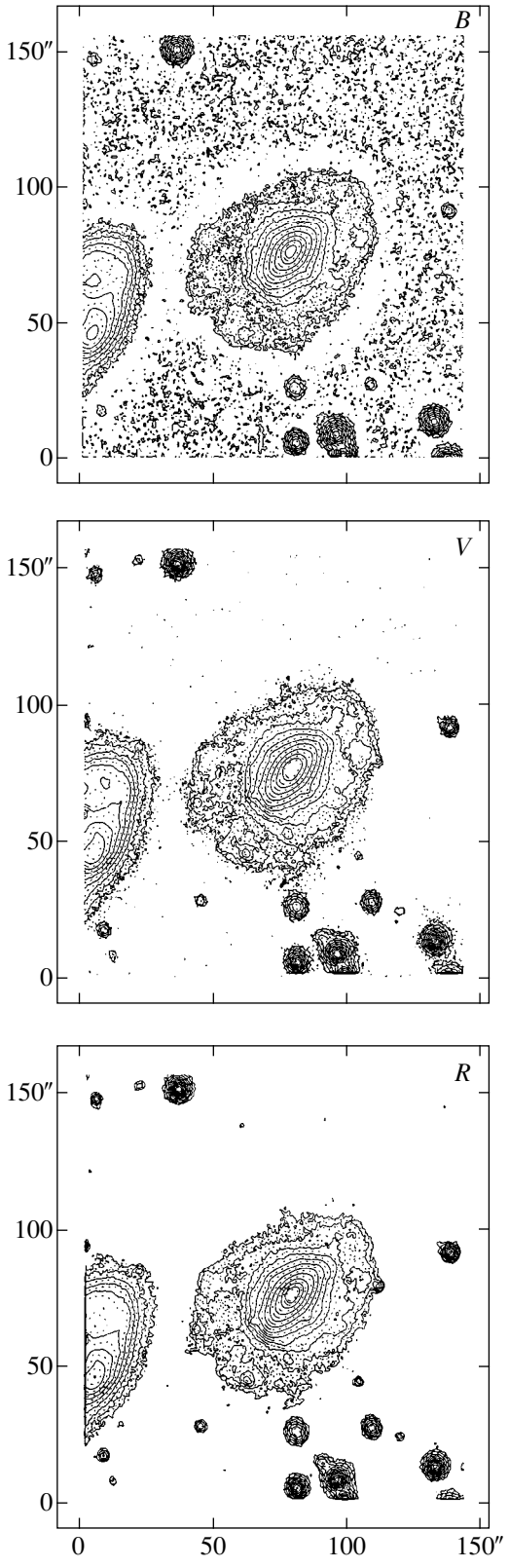

Fig. 4. The galaxy's isophotes in three bands at $0^m.3/\square''$ intervals. The ranges in the bands are from $20^m.1/\square''$ to $25^m.5/\square''$ in *B*; from $19^m.6/\square''$ to $25^m.6/\square''$ in *V*; and from $18^m.6/\square''$ to $25^m.2/\square''$ in *R*.

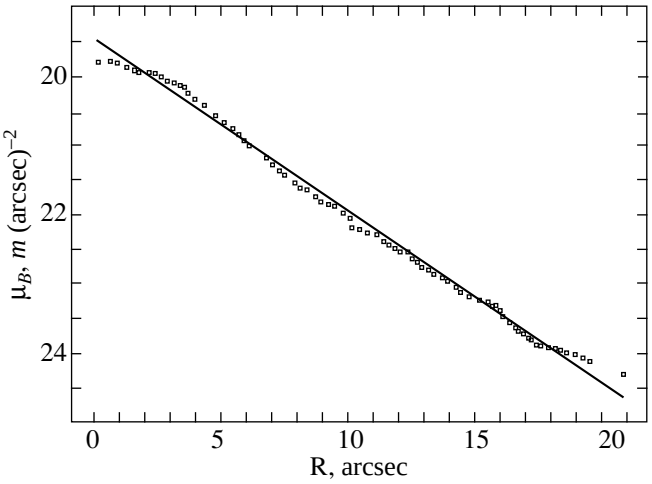

Fig. 5. Representation of the galaxy's profile along the major axis (dots) by a disk (solid line).

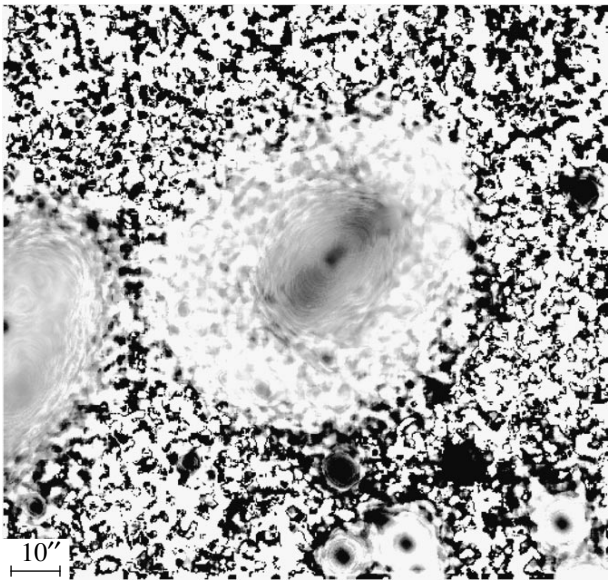

Fig. 6. The *B*–*V* distribution over the galaxy (the larger the color index, the darker the shading).

stars may concentrate). The blue color of the inner ring is also confirmed by the fact that the observed color in the regions corresponding to the isophote swellings due to the inner ring is bluer than that in the adjacent regions to the south and to the north.

In Fig. 7, the data for the galaxy's central part (Fig. 7a) and for the outer ring (Fig. 7b) are plotted separately to emphasize the differences between the diagrams. Since the brightness of the outer ring is low, the errors in the colors are large, causing a considerable scatter of points in Fig. 7b. Nevertheless, we can assert that the outer ring is the galaxy's bluest region. The mean color in this ring matches the colors of the spiral arms ($B–V = 0.3–0.4$). A comparison of Figs. 1 and 6 shows that the color variations have nothing to do with the clumpy structures in

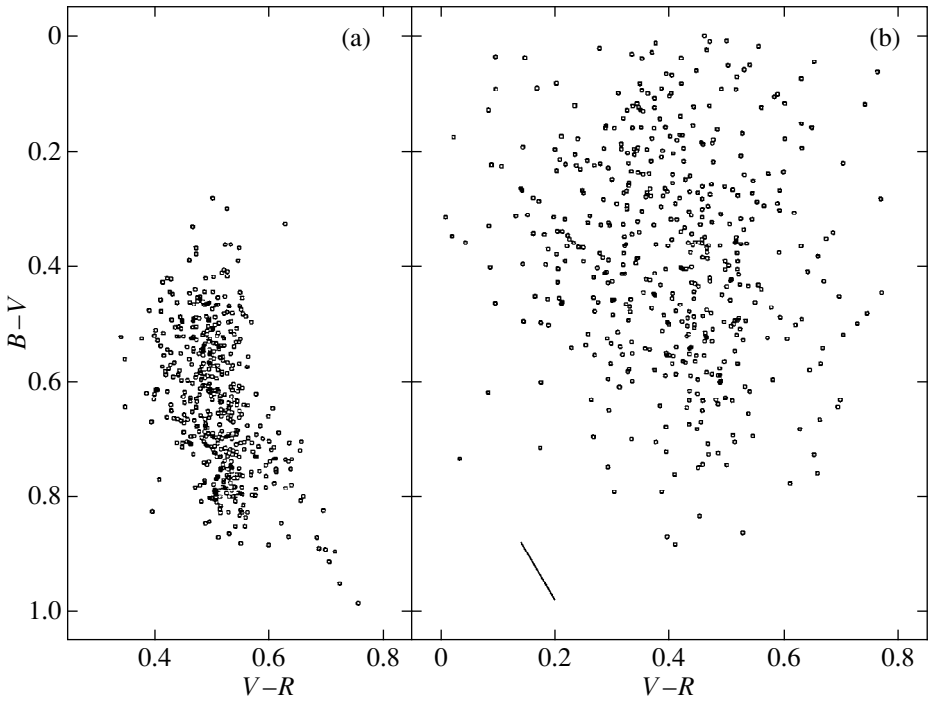

Fig. 7. Two-color diagrams (a) for the galaxy's central region and (b) for the outer ring (the direction of the reddening line is indicated by the segment).

the ring. The latter can be explained by the fact that the brightness rise in some regions of the outer ring is most likely due to fluctuations in stellar density.

A more detailed study of the outer structure indicates that this is probably not a ring, but spiral arms. To increase the contrast of these features, we subtracted the galaxy's disk contribution from the original image in the region of surface brightness higher than $\mu\ 22\overset{m}{.}2/\square''$ by using our values for the disk parameters and data on the galaxy's flattening. Figure 8 shows the brightness distribution in the residual image. In this figure, the structures resembling two arms wound counterclockwise around the galaxy's main body show up more clearly. One of them begins from its southwestern part, and the other begins from the northeastern part.

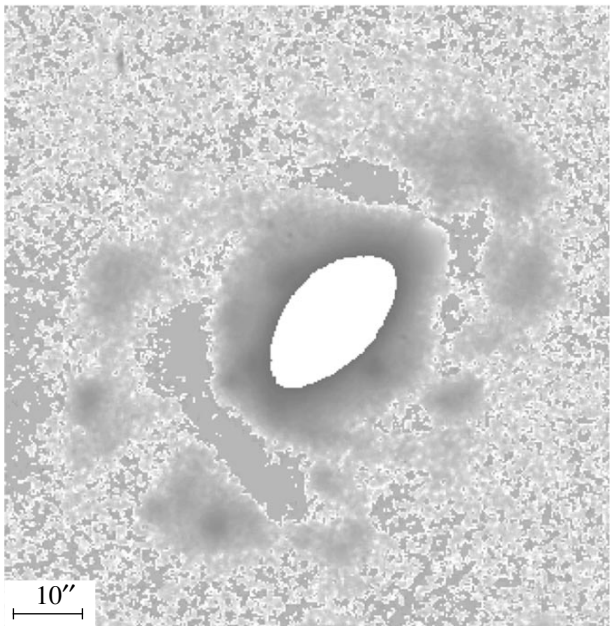

Fig. 8. The *B*-band brightness distribution with the contribution from the galaxy's disk subtracted.

CONCLUSION

Our photometric study has shown that UGC 5600 is most likely a dust-poor late-type spiral. The inner ring is apparently a polar ring seen at an angle to the plane of the sky; it is projected onto the main body on the northern side and is seen through it on the southern side. A final confirmation requires data on the rotation of the stellar component in the galaxy's main body. The presence of a polar ring in the late-type spiral, which, according to spectroscopic observations, is rich in gas, comes as a surprise. Classical polar-ring galaxies usually belong to the S0 type.

ACKNOWLEDGMENTS

We are grateful to the 6-m telescope Committee for allocating observing time and to the staff of the Special Astrophysical Observatory for assistance in the obser-

vations. This study was supported in part by the Federal Program “Astronomy” and the Russian Foundation for Basic Research (project no. 94-02-06026-a).

REFERENCES

1. A. U. Landolt, Astron. J. **88**, 439 (1983).
2. V. P. Reshetnikov and F. Combes, Astron. Astrophys. **291**, 57 (1994).
3. F. Simien and G. de Vaucouleurs, Astrophys. J. **302**, 564 (1986).
4. R. S. Smith, B. T. Jannuzi, and R. Elston, Astrophys. J., Suppl. Ser. **77**, 67 (1991).
5. G. de Vaucouleurs, A. de Vaucouleurs, J. R. Corwin, R. J. Buta, G. Paturel, and P. Fouque, *Third Reference Catalogue of Bright Galaxies* (Springer-Verlag, New York, 1991).
6. B. C. Whitmore, R. A. Lucas, D. B. McElroy, *et al.*, Astron. J. **100**, 1489 (1990).

Translated by N. Samus’

Astronomy Letters, Vol. 27, No. 2, 2001, pp. 81–90. Translated from Pis'ma v Astronomicheskiĭ Zhurnal, Vol. 27, No. 2, 2001, pp. 101–111.

Supersonic Steady Accretion of a Rotating Cold "Iron Gas" onto a Neutron Star after Gravitational Collapse

V. S. Imshennik* and M. S. Popov

Institute of Theoretical and Experimental Physics, ul. Bol'shaya Cheremushkinskaya 25, Moscow, 117259 Russia

Received July 13, 2000

Abstract—We analytically generalize the well-known solution of steady supersonic spherically symmetric gas accretion onto a star (Bondi 1952) for an iron atmosphere with completely degenerate electrons with an arbitrary degree of relativity. This solution is used for typical physical conditions in the vicinity of protoneutron stars produced by gravitational collapse with masses $M_0 = (1.4–1.8)M_\odot$ and over a wide range of nonzero "iron gas" densities at infinity, $\rho_\infty = (10^4–5 \times 10^6)$ g cm^{-3}. Under these conditions, we determine all accretion parameters, including the accretion rate, whose value is $\sim(10–50)M_\odot$ s^{-1} at $M_0 = 1.8M_\odot$ (it is a factor of 1.7 lower for $M_0 = 1.4M_\odot$, because the accretion rate is exactly $\propto M_0^2$). We take into account the effect of accreting-gas rotation in a quasi-one-dimensional approximation, which has generally proved to be marginal with respect to the accretion rate. © *2001 MAIK "Nauka/Interperiodica".*

Key words: *supernovae and supernova remnants, plasma astrophysics, hydrodynamics, and shock waves*

INTRODUCTION

The problem of "iron gas" accretion onto the so-called protoneutron star produced by the gravitational collapse of a stellar iron core arose when one-dimensional hydrodynamic calculations of this process were performed. It has been found that collapse develops homologically only within the interior part of a stellar iron core with mass $M_{iFe} = (0.6–0.8)M_\odot$ (see, e.g., Nadyozhin 1998), while its remaining exterior part [with $M_{eFe} = M_{Fe} - M_{iFe} \cong (0.4–1.4)M_\odot$, because the stellar mass is taken in a wide range, $M_{Fe} = (1.2–2.0)M_\odot$] lags behind in this process and undergoes comparatively slow gas-dynamical accretion onto the protoneutron-star embryo. Accretion for the largest mass $M_{Fe} = 2M_\odot$ with neutrino energy losses was computed by Nadyozhin (1977) for neutrino-transparency conditions. He obtained a characteristic time $t_{acc} \cong 10$ s, i.e., $\dot{M} \cong 0.1M_\odot$ s^{-1}. The hydrodynamic computation itself lasted up to ~3 s. The importance of postshock accretion (a rebound shock from collapse is generated at the instant a homogeneous protoneutron-star embryo forms and generally turns into an accretion shock) was pointed out in connection with the probable formation of a black hole in the remnant of SN 1987A (Brown *et al.* 1992). Clearly, accretion can facilitate the formation of a black hole, at least by increasing the mass of the central embryo. Estimates of the various authors cited in the above paper are based on the well-known steady-state solution by Bondi (1952), because direct hydrodynamic computations of collapse extend over no more than 10 s, while the characteristic times in these estimates are considerably longer, $\sim 10^3$ s.

A similar problem of accretion of the "iron gas" left from the exterior part of a collapsing iron core also arose when rotation effects were considered. Based on a quasi-one-dimensional model, Imshennik and Nadyozhin (1992) showed that, for sufficiently rapid initial rotation of an iron core with $M_{Fe} = 2M_\odot$ and with a proper allowance for neutrino processes, an iron atmosphere with a mass of $(0.1–0.2)M_\odot$ distributed fairly uniformly over the entire cavity of the initial iron core with an outer radius $R_{Fe} = 4.38 \times 10^8$ cm, i.e., with a mean density $\rho_{eFe} \cong (5.66 \times 10^5–1.13 \times 10^6)$ g cm^{-3}, was formed. The presumed long lifetime of a binary of neutron stars, which can be produced by the fragmentation of a rapidly rotating protoneutron star with a total mass of $(1.8–1.9)M_\odot$, implies that the steady-state one-dimensional problem of "iron gas" accretion onto the more massive neutron star, whose mass is estimated to be $(1.4–1.8)M_\odot$ (Imshennik and Manukovskiĭ 2000), is of considerable interest. In this one-dimensional problem, it also makes sense to take into account rotation by using the previously developed quasi-one-dimensional model. It should be immediately noted that the analysis may be restricted to a cold (at zero temperature) "iron gas", but with an arbitrary degree of relativity of its degenerate electrons. Clearly, this problem cannot be reduced to a simple polytropic approximation with a constant adiabatic index, in which the well-known

* E-mail address for contacts: imshennik@vxitep.itep.ru

solution was obtained (Bondi 1952). Here, we nevertheless analytically generalize the latter solution, because the specific enthalpy of a completely ionized degenerate electron gas in an iron atmosphere with an arbitrary degree of relativity of its electrons is very simple in form. The ion component of the "iron gas" contributes nothing to the equation of state. Note that the type of ions or even any their mixture instead of the iron ions with $A = 56$ and $Z = 26$ considered below is of no importance for our solution.

STATEMENT OF THE PROBLEM

The System of Hydrodynamic Equations

The system of hydrodynamic equations that describes the accretion of degenerate matter onto a star with mass M_0 in the absence of radiation and without allowance for the intrinsic magnetic field and the circumstellar-matter mass compared to M_0 is

$$\frac{\partial \mathbf{V}}{\partial t} + (\mathbf{V}\nabla)\mathbf{V} = -\frac{1}{\rho}\nabla P - \left(\frac{GM_0}{r^2} - \langle E_r\rangle\right)\frac{\mathbf{r}}{r}, \quad (1)$$

$$\frac{\partial \rho}{\partial t} + \operatorname{div}\rho\mathbf{V} = 0, \quad (2)$$

$$P = P(\rho). \quad (3)$$

Here, $\langle F_r\rangle$ is the radial component of the centrifugal force averaged over the solid angle. It is given by (Imshennik and Nadyozhin 1992)

$$\langle F_r\rangle = \frac{2}{3}\frac{\omega_0^2 r_0^4}{r^3}, \quad (4)$$

where the initial angular velocity ω_0 with which all the matter far from the star rotates is constant and does not depend on angle θ, and $j_0 = \omega_0 r_0^2$ is the specific angular momentum of the matter rotating with angular velocity ω_0 on the equator.

Equations (1) and (2) can be significantly simplified, because the problem is steady state and spherically symmetric. In this case, Eqs. (1) and (2) take the form with $V_r = V$

$$V\frac{dV}{dr} = -\frac{1}{\rho}\frac{dP}{dr} - \frac{GM_0}{r^2} + \frac{2}{3}\frac{j_0^2}{r^3}, \quad (5)$$

for which

$$\frac{1}{r^2}\frac{d}{dr}(r^2\rho V) = 0. \quad (6)$$

We may write the continuity equation (6) as

$$\dot{M} = 4\pi r^2 \rho V = \text{const} \quad (7)$$

and introduce a constant $A \equiv \frac{\dot{M}}{4\pi}$, which determines the rate of gas accretion. The quantity A is the most important parameter of the problem and must be determined when solving the system of equations (5) and (7).

The Equation of State

Below, we use the equation of state for a completely degenerate (ideal) electron gas with an arbitrary degree of relativity; i.e., we imply a zero entropy of the matter composed of ^{56}Fe. The matter is considered to be completely degenerate if the following degeneracy condition (Landau and Lifshitz 1951, pp. 185–192) is satisfied:

$$T \ll \frac{(3\pi)^{2/3}}{2}\frac{\hbar^2}{k_B m_e} n_e^{2/3}. \quad (8)$$

In our case, the condition (8) is always satisfied for the following reasons. The gas temperature is moderately high far from the neutron star, $\leq 10^9$ K (Imshennik and Manukovskiĭ 2000), and the condition (8) is valid, for example, at a typical value of $\rho = 10^6$ g cm^{-3}, so $n_e = 2.80 \times 10^{29}$ cm^{-3} and, hence, $T_{\text{deg}} = 1.80 \times 10^9$ K. As the star is approached, the density of the matter rises, increasing its degeneracy temperature. Therefore, approximately the same rise in gas temperature for isoentropic compression does not affect the validity of (8) and has no significant effect on the course of accretion. Thus, the electron density in such a completely ionized iron plasma ("iron gas") is

$$n_e = \frac{\rho}{m_u}\frac{26}{56}, \quad (9)$$

where m_u is the atomic mass unit. In this case, the pressure P and specific internal energy ε are given by (Landau and Lifshitz 1951)

$$P = C\left[\xi_F\left(\frac{2}{3}\xi_F^2 - 1\right)\sqrt{1+\xi_F^2} + \operatorname{arcsinh}\xi_F\right], \quad (10)$$

$$\varepsilon = \frac{C}{\rho}\left[\xi_F(2\xi_F^2 + 1)\sqrt{1+\xi_F^2} - \operatorname{arcsinh}\xi_F\right], \quad (11)$$

where the dimensionless Fermi momentum (in units of $m_e c$) is

$$\xi_F = B\rho^{1/3}, \quad (12)$$

and the constants B and C take on the well-known values

$$B = \frac{2\pi\hbar}{m_e c}\left(\frac{39}{224\pi m_u}\right)^{1/3} = 7.792 \times 10^{-3} \text{ cm g}^{-1/3},$$

$$C = \pi m_e c^2\left(\frac{m_e c}{2\pi\hbar}\right)^3 = 1.801 \times 10^{23} \text{ g cm}^{-1} \text{ s}^{-2}.$$

It is easy to verify that the functions (10) and (11), as should be the case, satisfy the thermodynamic relation

$$P = \rho^2\frac{d\varepsilon}{d\rho}, \quad (13)$$

because the specific entropy, according to Eqs. (10) and (11), is constant and zero.

Subsequent calculations can be substantially simplified by using a simple representation of the derivatives of pressure (Imshennik and Manukovskiĭ 2000):

$$\frac{\partial P}{\partial \eta} = M\rho\frac{\partial \Phi}{\partial \eta}, \quad \Phi = \sqrt{1 + B^2\rho^{2/3}}, \tag{14}$$

where η is an arbitrary parameter, and M can be expressed in terms of the constants B and C introduced above:

$$M = \frac{8}{3}CB^3 = 2.272 \times 10^{17}\ \mathrm{cm}^2\ \mathrm{s}^{-2}.$$

We emphasize that the function Φ has the meaning of dimensionless specific enthalpy of a completely degenerate electron gas, as can be easily verified using Eqs. (10) and (11) by adding up ε and P/ρ, i.e., $\varepsilon + P/\rho = M\Phi$.

In the limiting cases, the pressure (10) for the degree of relativity $\xi_F \gg 1$ and $\xi_F \ll 1$ can be represented in a form convenient for the subsequent calculations as follows:

$$\xi_F \ll 1\text{: } P = \frac{8C}{3}\left(\frac{B^5\rho^{5/3}}{5} - \frac{B^7\rho^{7/3}}{14}\right), \tag{15}$$

$$\xi_F \gg 1\text{: } P = \frac{2C}{3}(B^4\rho^{4/3} - B^2\rho^{2/3}). \tag{16}$$

The Equation of "Iron Gas" Accretion

Let us rewrite the Euler equation (5) by using relation (14) at $\eta = r$ as

$$V\frac{dV}{dr} = -M\frac{d\Phi}{dr} - \frac{GM_0}{r^2} + \frac{2}{3}\frac{j_0^2}{r^3}, \tag{17}$$

whence the Bernoulli integral can be easily obtained. This integral, together with the continuity equation (7) and the definition of constant A, gives the system of equations that completely determines spherically symmetric steady "iron gas" accretion:

$$\frac{V^2}{2} + M\Phi = \beta + \frac{GM_0}{r} - \frac{j_0^2}{3r^2}, \tag{18}$$

$$V = \frac{A}{\rho r^2}, \tag{19}$$

where β is the integration constant, and the specific enthalpy $M\Phi$ naturally enters into the Bernoulli integral (Landau and Lifshitz 1987). The constant β is determined by the gas density for $r \longrightarrow \infty$, where $V \longrightarrow 0$. Indeed, taking $r \longrightarrow \infty$ in Eqs. (18) and (19) yields at $\rho_\infty \neq 0$

$$\beta = M\Phi_\infty = m\sqrt{1 + B^2\rho_\infty^{2/3}}. \tag{20}$$

It should be immediately noted that the inequality $\beta > M$ follows from (20). The constant β can be determined by specifying the density ρ_0 at some finite point r_0. However, we will not consider this method of determining β, because the solution becomes considerably more complicated and because the results differ only slightly from the results of the method outlined above.

Finally, we derive a general expression for the speed of sound, which is required for the subsequent analysis:

$$a^2 = \left(\frac{\partial P}{\partial \rho}\right)_S = \frac{dP}{d\rho}. \tag{21}$$

For an "iron gas," it can be uniquely represented, according to (14) at $\eta = \rho$, as a function of dimensionless specific enthalpy Φ:

$$a^2 = M\rho\frac{d\Phi}{d\rho} = \frac{M}{3}\frac{\Phi^2 - 1}{\Phi}. \tag{22}$$

THE METHOD OF SOLUTION AND RESULTS

Passage through the Speed of Sound

Following Bondi (1952), we seek the point of passage through the speed of sound (sonic point) by assuming that this passage occurs under the additional condition for the first derivatives of all quantities being equal. This condition was justified by Zel'dovich and Novikov (1971) in their qualitative analysis of the system of equations (18) and (19). Setting $V = a$ in (18) and (19) and using (22), we find that the following relations hold at the sonic point:

$$\frac{M}{6}\frac{7\Phi^2 - 1}{\Phi} = \beta + \frac{GM_0}{r} - \frac{j_0^2}{3r^2}, \tag{23}$$

$$\frac{M}{3}\frac{(\Phi^2 - 1)^4}{\Phi} = \frac{A^2B^6}{r^4}. \tag{24}$$

Here, the density ρ is expressed in terms of Φ as $\rho^2 = (\Phi^2 - 1)^3B^{-6}$, according to (14). Differentiating (23) and (24) with respect to r and eliminating the derivative $\frac{d\Phi}{dr}$ from the derived expressions and using (24) yield

$$a^2 = \frac{GM_0}{2r} - \frac{j_0^2}{3r^2}. \tag{25}$$

Note that precisely the same expression for the speed of sound at the sonic point would also be obtained for the polytropic equation of state $P = P_0\left(\frac{\rho}{\rho_0}\right)^\gamma$ for a gas (Lipunov 1987), suggesting that this solution is similar to the solution of Bondi (1952).

From (23) and (25) and using (22) for $r = r_s$, we derive the system of equations for the sonic point $r = r_s$

$$M\Phi = \beta + \frac{3GM_0}{4r_s} - \frac{j_0^2}{6r_s^2}, \tag{26}$$

$$\frac{M}{3}\frac{\Phi^2 - 1}{\Phi} = \frac{GM_0}{2r_s} - \frac{j_0^2}{3r_s^2}, \tag{27}$$

whence, after eliminating the sought-for quantity Φ, we obtain an algebraic equation for r_s:

$$\begin{aligned} 144(\beta^2 - M^2)r_s^4 + [96\beta j_0^2 - 81(GM_0)^2]r_s^2 \\ + 108 j_0^2 GM_0 r_s - 20 j_0^4 = 0. \end{aligned} \tag{28}$$

The solution of this equation for r_s with each pair of β and j_0 values in this problem is unique. It defines the constant A for the accretion rate via r_s, according to (24):

$$\begin{aligned} A = \frac{r_s^2}{B^3 M^3} \\ \times \sqrt{\left(\frac{GM_0}{2r_s} - \frac{j_0^2}{3r_s^2}\right)\left[\left(\beta + \frac{3}{4}\frac{GM_0}{r_s} - \frac{j_0^2}{6r_s^2}\right)^2 - M^2\right]^3}. \end{aligned} \tag{29}$$

The criterion for selecting the only root for r_s from (28) is discussed below.

Constraining the Angular Momentum

Note that a constraint on j_0 follows from the Bernoulli integral (18). Indeed, the left part of this equation is positive; therefore, its right part must also be greater than zero for all r, including the smallest distance $r = R$, where R is the neutron-star radius. Thus, the following inequality must hold:

$$\beta + \frac{GM_0}{R} - \frac{j_0^2}{R^2} > 0. \tag{30}$$

Since, according to (20), $\beta > M$, the maximum possible specific angular momentum of the gas at infinity $j_0^{\max}$ can be expressed as

$$j_0^{\max} = 3MR^2 + 3RGM_0. \tag{31}$$

For the inequality (30) to hold, it will clearly suffice that the specified j_0 be smaller than $j_0^{\max}$ (31).

The $j_0 = 0$ Case

If there is no rotation, Eq. (28) takes a simple form:

$$144(\beta^2 - M^2)r_s^4 - 81(GM_0)^2 r_s^2 = 0. \tag{32}$$

This equation can be easily solved, and the only physically reasonable root is

$$r_s = \frac{3GM_0}{4\sqrt{\beta^2 - M^2}}. \tag{33}$$

The accretion rate (29) then explicitly depends on β,

$$A = \frac{(GM_0)^2}{4B^3M^3}(3\sqrt{\beta^2 - M^2} + 3\beta)^{3/2}, \tag{34}$$

which follows from a substitution of r_s (33) in (29) for $j_0 = 0$.

Limiting Cases of the Equation of State

Assuming, as before, that $j_0 = 0$, we derive expressions for r_s and A in the two limiting cases of the general equation of state (10), $\xi_F \gg 1$ and $\xi_F \ll 1$, with only the first expansion terms from (15) and (16) being retained in (26) and (27). According to (15), $P = \frac{8C}{3}\frac{B^5\rho^{5/3}}{5}$ for $\xi_F \ll 1$; attempting to determine, as previously, the radius r_s of the sonic point and using the fact that $\Phi = 1 + \frac{B^2\rho^{2/3}}{2}$ in this case, we obtain the following. The radius r_s of the point of passage through the speed of sound completely drops out of the system of equations (26) and (27), which yields $\beta = M$ alone. Formula (33) is therefore inapplicable in this case, and r_s can be determined only from Eq. (28) by setting $\beta = M$ and $j_0 = 0$. Thus, we find that $r_s = 0$, and the flow is subsonic everywhere, because it is subsonic by the meaning of the boundary condition (20) when $r \longrightarrow \infty$. Note that this result is consistent with Eq. (32), which, apart from the root given by (33), has the second root $r_s = 0$. The accretion rate in this limiting case does not depend on β at all and is given by

$$A_{5/3} = \frac{(GM_0)^2}{4B^3}\left(\frac{3}{M}\right)^{3/2}. \tag{35}$$

It may be shown that in this special case, the accretion rate follows not only from the general formula (29) (at $j_0 = 0$) with a substitution of the root found $r \longrightarrow r_s = 0$, but also from formula (34), in which the other root r_s from (33) has already been substituted. This is one of the properties of the special case under consideration. According to (16), $P = \frac{2C}{3}B^4\rho^{4/3}$ in the other limiting case $\xi_F \gg 1$, and no such complications arise. As with the general equation of state and $j_0 \neq 0$, we easily find that, for $\Phi = B\rho^{1/3}$ and $\beta \gg M$ and according to (33),

$$r_s = \frac{3GM_0}{4\beta}. \quad (36)$$

We then derive from (34)

$$A_{4/3} = \frac{(GM_0)^2}{4B^3}\left(\frac{6\beta}{M^2}\right)^{3/2}; \quad (37)$$

i.e., the accretion rate exceeds $A_{5/3}$ by a factor of $\left(\frac{2\beta}{M}\right)^{3/2} \gg 1$ in this limiting case. Note that (37) closely matches Bondi's solution for $\gamma = 4/3$ (Spitzer 1981, pp. 309–311). We see from (34), (35), and (37) that the accretion rate increases with β. The value of $A = A_{5/3}$ reaches a minimum at $\beta = M$ and then increases initially according to (34) and, at large β, according to (37). This tendency is also preserved for a nonzero angular momentum j_0; only the rotation slightly slows down its growth. If one expansion term in (15) is retained, then Eq. (28) does not have any real solutions at all for $j_0 \neq 0$. This implies that, if the equation of state is $P \propto \rho^{5/3}$, then the rotation cannot be specified in the above way. This difficulty can be circumvented by retaining the second term in the expansion (15), as is done below.

Critical Radius r_c

The radius up to which the gas density is essentially constant and equal to ρ_∞ can be determined by using Eqs. (18) and (19) (Zel'dovich and Novikov 1971). Substituting (19) in (18) and assuming that $\rho = \rho_\infty$ yield the equation for r_c

$$r_c^3 - \frac{j_0^2}{3GM_0}r_c^2 - \frac{A^2}{2\rho_\infty^2 GM_0} = 0. \quad (38)$$

If $j_0 = 0$, then an exact expression for r_c can be derived from (38) by taking into account relation (34) for A:

$$r_c = \frac{3GM_0}{2\sqrt[3]{4}B^3M^2\rho_\infty^{2/3}}(\beta + \sqrt{\beta^2 - M^2}). \quad (39)$$

Since introducing the critical radius r_c allows the notion of infinity to be excluded, in a sense, this problem may be considered in a bounded region of space without taking care of other effects in this space. An analysis actually shows that the derivative $d\rho/dr$ does not become zero at $r > r_c$.

Dimensionless Equations

Before turning to numerical estimates, we transform the basic equations to dimensionless ones. Let us first consider Eq. (28), which is to be solved numerically. Clearly,

$$r_s = f(\beta, GM_0, j_0, M); \quad (40)$$

i.e., r_s can be a function of all four dimensional parameters in the derived equation. Their dimensions, including r_s, are

$$[r_s] = L, \quad [GM_0] = \frac{L^3}{T^2}, \quad [M] = [\beta] = \frac{L^2}{T^2}. \quad (41)$$

We see from the dimensional formulas (41) that only two of the four parameters have independent dimensions. Indeed, taking GM_0 and M as these two parameters, we then easily find that $[\beta] = [M]$ and $[j_0] = \frac{[GM_0]}{[M]^{1/2}}$, while $[r_s] = \frac{[GM_0]}{[M]}$. According to the elementary dimensional theory (Sedov 1957), Eq. (32) can thus be represented in dimensionless form:

$$P = f(P_1, P_2), \quad (42)$$

where $P = f, P_1, P_2$ are dimensionless quantities, which are defined according to the above dimensions as

$$f = \frac{r_s M}{GM_0}, \quad P_1 = \frac{\beta}{M}, \quad P_2 = \frac{j_0^2 M}{(GM_0)^2}. \quad (43)$$

Using the definitions (43), we can write Eq. (28) in dimensionless form as

$$144(P_1^2 - 1)f^4 + (96P_1P_2 - 81)f^2 + 108P_2 f - 20P_2^2 = 0. \quad (44)$$

Let us now make the first numerical estimates. We consider a hot neutron star (protoneutron star) with radius $R = 60$ km and mass $M_0 = 1.8M_\odot$ (or $M_0 = 1.4M_\odot$) as the accreting star. The range of P_1 is chosen from the following considerations. The parameter P_1 is always greater than unity because of the constraint $\beta > M$, but differs only slightly from unity at $\rho_\infty \leq 10^6$ g cm^{-3}. We may assume that $1 < P_1 \leq 1.268$. The parameter P_2 changes from zero at $j_0 = 0$ to $P_2^{\max}$ at $j_0 = j_0^{\max}$. According to (31), $j_0^{\max} = 6.576 \times 10^{16}$ cm^2 s^{-1} (at $M_0 = 1.8M_\odot$) or $j_0^{\max} = 5.805 \times 10^{16}$ cm^2 s^{-1} (at $M_0 = 1.4M_\odot$) for the selected neutron-star radius. Note that these maximum values correspond to our estimates of the total angular momentum $J_0 = (1.2–2.6) \times 10^{49}$ erg s for the above iron-atmosphere mass in the range $(0.1–0.2)M_\odot$. Thus, the range of P_2 is also narrow: $0 \leq P_2 \leq 0.017$ ($M_0 = 1.8M_\odot$) and $0 \leq P_2 \leq 0.022$ ($M_0 = 1.4M_\odot$). We may therefore assume that r_s and r_c cannot differ greatly from their values at $j_0 = 0$. This can serve as a criterion when choosing the roots of Eqs. (28) and (38) for a nonzero angular momentum of the gas at infinity. The smallness of P_2 implies that the rotation effect is a small correction in the problem under consideration. According

to (29), the dimensionless function f determines the accretion rate. Introducing a dimensionless parameter

$$P_3 = \frac{A^2B^6M^3}{(GM_0)^4}, \quad (45)$$

we derive from (29):

$$P_3 = f^3\left(\frac{1}{2} - \frac{P_2}{3f}\right)\left[\left(P_1 + \frac{3}{4f} - \frac{P_2}{6f^2}\right)^2 - 1\right]^3. \quad (46)$$

Using the same procedure to make Eq. (38) dimensionless yields

$$g^3 - \frac{P_2}{3}g^2 - \frac{P_3}{2(P_1^2-1)^3} = 0, \quad (47)$$

where $g = \frac{r_cM}{GM_0}$, and we took into account the obvious relation $\rho_\infty^2 = (P_1^2 - 1)^3B^{-6}$.

In order to obtain the profiles of fall velocity $V(r)$ and speed of sound $a(r)$ and the dependence $\rho(r)$, the system of equations (18) and (19) should be reduced to a single dimensionless equation. To this end, we substitute (19) in (18), use the fact that by definition $\rho^2 = (\Phi^2 - 1)^3B^{-6}$, and introduce a dimensionless independent variable $h = \frac{rM}{GM_0}$. We then find that the sought-for function Φ satisfies the following equation with the independent variable h:

$$\Phi(\Phi^2-1)^3 + \frac{P_3}{2h^4} - \left(P_1 + \frac{1}{h} - \frac{P_2}{3h^2}\right)(\Phi^2-1)^3 = 0. \quad (48)$$

This is an algebraic equation of the seventh degree whose even powers all have coefficients dependent on h, P_1, and P_2 (a dependence on P_3 also appears for a zero power of Φ), while the odd powers of Φ are constant.

The function $\Phi = \Phi(h)$ of interest can be numerically found from Eq. (48). After changing to a dimensional independent variable $r = \frac{GM_0}{M}h$, this function allows us to determine the dependence $\rho(r) = (\Phi^2 - 1)^{3/2}B^{-3}$ and then $V(r)$ from (19) and $a(r)$ from (22). We emphasize that these calculations are in no way related to the previous solution for the parameters of the sonic point, but the dimensionless parameter P_3 was taken precisely from the latter as the accretion rate.

Accretion Rate

According to Eq. (46), P_1 and P_2 determine the dimensionless radius of the sonic point f and, consequently, according to (46), the parameter P_3, i.e., the accretion rate. It is of interest to compare the accretion rates A for different general equations of state and different rotation effects. As has already been mentioned above, the polytropic case with $P \propto \rho^{5/3}$ and $j_0 \neq 0$ cannot be realized for the method of allowance for rotation under consideration. This difficulty can be overcome by assuming that the equation of state is given by the full two-term expression (15). Similar to the above procedure, we then find for the general equation of state and its limiting cases that the dimensionless radius of the sonic point f can be determined from the equation of the fourth degree

$$4P_2^2\left(\frac{1}{f}\right)^4 + 36P_2\left(\frac{1}{f}\right)^3 + (96P_1P_2 - 192P_2 + 81)\left(\frac{1}{f}\right)^2 + 432(P_1-1)\frac{1}{f} + 576(P_1-1)^2 - 288(P_1-1) = 0. \quad (49)$$

The accretion rate, as before, is given by (46). If, however, we set $P_2 = 0$ in (49), then it is easy to find that the solution of the quadratic equation without rotation is

$$f = \frac{3}{4\sqrt{P_1-1}(\sqrt{2} - 2\sqrt{P_1-1})}. \quad (50)$$

We see from (50) that the approximate equation of state (15) is applicable for $1 < P_1 < 1.5$. This result near the lower limit of P_1 matches the root (33) for the general equation of state. If, alternatively, we assume that $\xi_F \gg 1$, then it will suffice to take only the first expansion term in (16) in order to obtain A for all possible values of P_1 and P_2. In this case, the equation for the radius of the sonic point is

$$12P_1f^2 - 9f + 10P_2 = 0. \quad (51)$$

It is easy to see that (36) follows from (51) at $P_2 = 0$. The accretion rate, as before, is given by (46).

Thus, expression (46) is valid for any of the equations of state under consideration, but the values of f in (46) for each of them can be determined from the corresponding Eqs. (44), (49), and (51).

Numerical Results

We numerically solved Eqs. (44), (47), and (48), which yielded the full pattern of spherically symmetric supersonic steady "iron gas" accretion. Our main results are given in Tables 1 and 2. Note that the last two rows in both tables refer to $M_0 = 1.4M_\odot$, because the range of P_2 is extended for such a neutron-star mass. The remaining dimensionless parameters in Tables 1 and 2 are the same for $M_0 = 1.8M_\odot$ and $M_0 = 1.4M_\odot$.

Below, we provide formulas for transforming the dimensionless parameters in the tables to dimensional quantities. For $M_0 = 1.8M_\odot$, they appear as

$$r_s = 1.052\times10^9 f \text{ cm}, \quad r_c = 1.052\times10^9 g \text{ cm},$$
$$r = 1.052\times10^9 h \text{ cm}, \quad A = 1.116\times10^{33}P_4^{1/2} \text{ g s}^{-1},$$
$$j_0 = 5.014\times10^{17}P_2^{1/2} \text{ cm}^2 \text{ s}^{-1}, \quad (52)$$

and slightly differently for $M_0 = 1.4M_\odot$:

$$r_s = 8.185\times10^8 f \text{ cm}, \quad r_c = 8.185\times10^8 g \text{ cm},$$
$$r = 8.185\times10^8 h \text{ cm}, \quad A = 6.753\times10^{32} P_4^{1/2} \text{ g s}^{-1},$$
$$j_0 = 3.900\times10^{17} P_2^{1/2} \text{ cm}^2 \text{ s}^{-1}. \quad (53)$$

We clearly see from Tables 1 and 2 that the accretion rate dramatically increases with ρ_∞, but the sonic point approaches the star, and the accretion region becomes more compact. At the same time, introducing an average centrifugal force reduces the accretion rate at each given density ρ_∞. However, because of the significant constraint (35), the effect of given rotation is marginal and cannot offset the rise in accretion rate due to an increase in ρ_∞; rotation has an appreciable effect only when j_0 is close to $j_0^{\max}$.

The profiles of fall velocity $V(r)$, speed of sound $a(r)$, and density $\rho(r)$ were obtained by solving Eq. (48) with specified P_1 and P_2 for all h with $R < r < r_c$. The results are presented in Figs. 1–4. Figure 1 shows the density profiles and $\Phi(r)$ for various cases of "iron gas" accretion at $P_1 = 1.19$. We see that, if the gas has an angular momentum at infinity, the density near the star is appreciably higher and exceeds the density of the gas with a zero angular momentum up to the sonic point; this difference is barely noticeable after this point. The Bernoulli integral (19) in dimensionless form can be written as

$$1 + \Phi + \frac{1}{2}\frac{P_3}{(\Phi^2-1)^3 h^4} - \frac{1}{h} + \frac{1}{3}\frac{P_2}{h^2} = P_1, \quad (54)$$

where the terms in the left part have the meaning of dimensionless enthalpy, kinetic energy, gravitational energy, and rotational energy, respectively. For the energy characterization of the contribution of rotation to the accretion solution, specific numerical values of these terms in the case $P_1 = 1.19$ under consideration (Table 2 and Figs. 1, 2) can be compared for two values of P_2: $P_2 = 0$ and $\tilde{P}_2 = 0.015$. It is natural to make this comparison at the sonic points with dimensionless coordinates $h = f$, where $f = 1.164$, $\tilde{f} = 1.141$ and $P_3 = 10.41$, $\tilde{P}_3 = 10.23$. The four corresponding terms from (54) are given in Table 3. Note that the sum of all four terms is $P_1 - 1 = 0.19$, the enthalpy at infinity. In particular, the enthalpy at the sonic point for the above two values of P_2 increased in a ratio $\Phi/(P_1 - 1)$ of 4.39 and 4.45, respectively. At the same time, the kinetic, gravitational (in magnitude), and rotational energies account for 0.258 and 0.257, 1.030 and 1.037, and a mere 0.005 of this enthalpy, respectively. The energy effect of rotation at the sonic point is less than 1%. We may also compare the rotation velocity $V_\varphi = j_0/r$ with the fall velocity $V_f = M^{1/2}P_3^{1/2}(\Phi^2 - 1)^{-3/2}f^{-2}$, so that $V_\varphi/V_f \cong 0.163$.

Table 1. Basic dimensionless parameters f, P_3, and g for our numerical solutions at $R = 60$ km and $\rho_\infty = 10^4$ g cm^{-3} ($P_1 = 1.014$) versus P_2

P_2	f	P_4	g
0	4.469	2.785	39.647
0.0001	4.468	2.785	39.647
0.001	4.465	2.785	39.643
0.005	4.452	2.781	39.628
0.01	4.435	2.777	39.609
0.012	4.428	2.775	39.601
0.015	4.418	2.773	39.589
0.017	4.411	2.771	39.581
0.02	4.401	2.769	39.570
0.022	4.394	2.767	39.562

Table 2. Same as Table 1 for $\rho_\infty = 5.66\times10^5$ g cm^{-3} ($P_1 = 1.190$)

P_2	f	P_4	g
0	1.164	10.410	4.174
0.0001	1.164	10.409	4.174
0.001	1.162	10.398	4.172
0.005	1.156	10.350	4.166
0.01	1.149	10.290	4.159
0.012	1.146	10.266	4.156
0.015	1.141	10.230	4.151
0.017	1.138	10.204	4.148
0.02	1.133	10.170	4.144
0.022	1.130	10.144	4.140

Figure 1 also shows the density profiles for the free fall of a gas both with and without an angular momentum. These solutions can be easily obtained from the Bernoulli integral for a zero enthalpy of the matter and zero fall velocity at infinity in Eqs. (18) and (19):

$$V = \sqrt{\frac{2GM_0}{r} - \frac{2}{3}\frac{j_0^2}{r^2}}, \quad \rho = \frac{A}{Vr^2}. \quad (55)$$

For a comparison with the accretion solutions under consideration, it would be natural to use the same accretion rates A in (55).

Figure 2 shows the $V(r)$ and $a(r)$ profiles for a gas with a zero angular momentum. We clearly see the sonic point after which the accretion becomes supersonic. The fall velocity near the star continues to increase. Also shown in the figure is the profile of the gas fall velocity, which is higher than the accretion velocity everywhere and exceeds it by a factor of a mere 1.051 at $r = R = 60$ km. Figure 3 presents the $V(r)$ and $a(r)$ profiles for a gas with an angular momentum that is sufficiently close the maximum possible value. The principal difference between Figs. 3 and 2 is

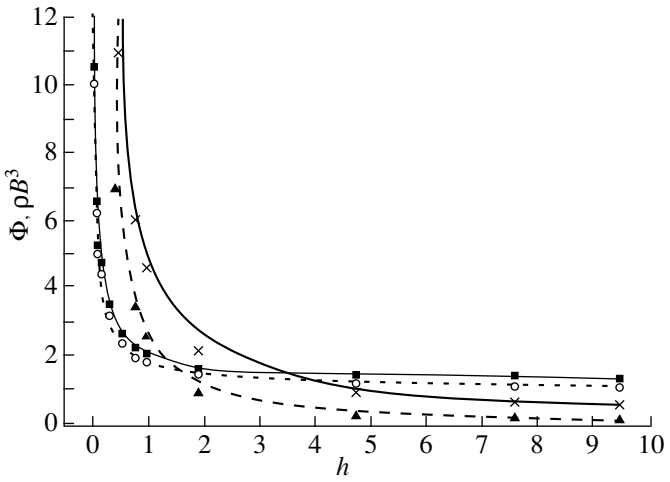

Fig. 1. The profiles of dimensionless density ρB^3 and enthalpy Φ for an "iron gas" in the general case of accretion described by (18) and (19) and for a free fall with various rotation effects at $P_1 = 1.190$ (cf. Table 2). The thin solid line and squares represent the Φ profile for the general case of accretion at $P_2 = 0$ and 0.015, respectively; the dotted line and circles represent the Φ profile for a free fall at $P_2 = 0$ and 0.015; the heavy solid line and crosses represent the ρB^3 profile for the general case of accretion at $P_2 = 0$ and 0.015; and the dashed line and triangles represent the ρB^3 profile for a free fall at $P_2 = 0$ and 0.015.

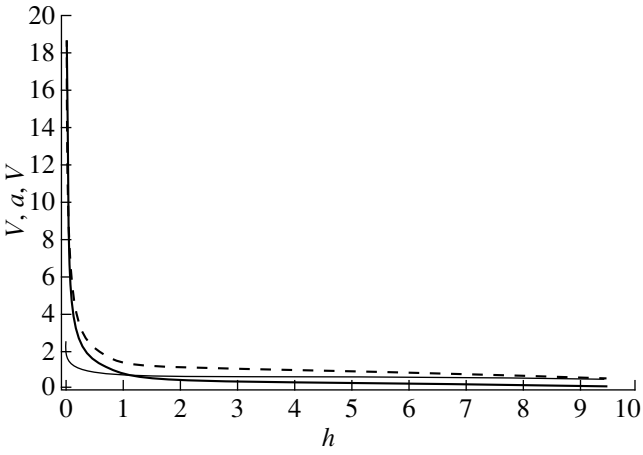

Fig. 2. The profiles of fall velocity V (heavy solid line) and speed of sound a (thin solid line) for an "iron gas" in the general case of accretion and the profile of fall velocity V for an "iron gas" in the case of a free fall (dashed line) when the gas has a zero angular momentum at infinity $P_2 = 0$ for $P_1 = 1.190$ and $P_3 = 10.41$ (cf. Table 2). The units of measurement for the velocities are $[V] = [a] = [V] = M^{1/2}$.

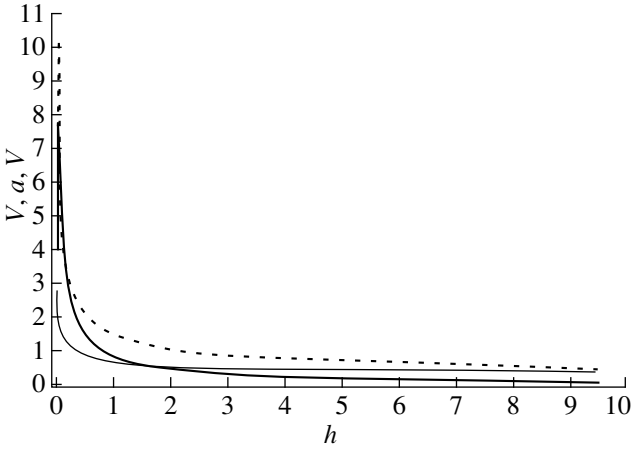

Fig. 3. Same as Fig. 2 for $P_2 = 0.015$ and $P_3 = 10.23$.

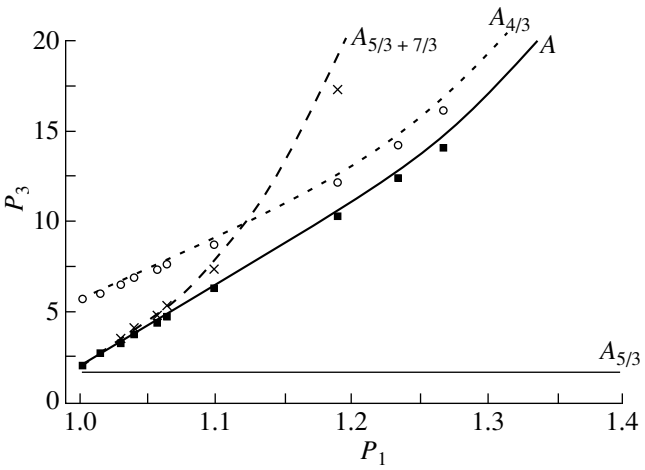

Fig. 4. Parameter P_3, which determines the accretion rate, versus P_1 for the rotation parameter $P_2 = 0$ (lines) and 0.015 (symbols) for various equations of state. A is the accretion rate for the general equation of state (10) (heavy solid line and squares), $A_{5/3}$ is the accretion rate for the equation of state $P \propto \rho^{5/3}$ (thin solid line), $A_{4/3}$ is the accretion rate for the equation of state $P \propto \rho^{4/3}$ (dotted line and circles), and $A_{5/3+7/3}$ is the accretion rate for the equation of state (15) (dashed line and crosses).

observed near the star. The gas fall velocity decreases sharply in this region, with the speed of sound increasing slightly more rapidly than that in Fig. 2 because of the rise in density. The sharp and nonmonotonic decrease in fall velocity near the star can be explained by the strong effect of the average centrifugal force at small r, which decelerates the falling gas while increasing the density of the gas itself (see Fig. 1).

In Fig. 4, accretion rate (or, more precisely, P_3) is plotted against P_1 and P_2 (the two main parameters of the problem), which determine the entire gas flow, for various equations of state. We see that the accretion rate considerably increases with P_1 for all equations of state, except, of course, the special case of $P \propto \rho^{5/3}$. Figure 4 also shows that a nonzero angular momentum of the gas reduces, though only slightly, the accretion rate for all equations of state, except the same special case of $P \propto \rho^{5/3}$. As would be expected, the equations of state (15) and (16) approximate well the general equation of state at low (small P_1) and high (large P_1) densities ρ_∞, respectively. It should be emphasized that only the general equation of state (10) can describe the entire accretion

Table 3. Dimensionless terms of the Bernoulli integral at the sonic point with and without rotation (example)

P_2	Φ	$\frac{1}{2}\frac{P_3}{f^4(\Phi^2-1)^3}$	$-\frac{1}{f}$	$\frac{1}{3}\frac{P_2}{f^2}$	f
0	0.834	0.215	−0.859	0	1.164
0.015	0.845	0.217	−0.876	0.004	1.141

Table 4. Accretion rate versus initial densities ρ_∞ without rotation

P_1	ρ_∞, g cm^{-3}	P_3	$A/A_{4/3}$	$\dot{M} = 4\pi A$, $M_\odot$ s^{-1} ($M_0 = 1.8M_\odot$)
1.014	10^4	2.785	0.445	11.724
1.040	5×10^4	3.946	0.510	13.955
1.063	10^5	4.882	0.548	15.522
1.190	5.66×10^5	10.410	0.677	22.665
1.268	10^6	14.466	0.725	26.718
1.666	5×10^6	45.459	0.854	47.362

process, for the gas fall is accompanied by a rise in gas density. All in all, Fig. 4 may be considered as a dependence of the maximum accretion rate on the gas density at infinity ρ_∞ in the limiting case of a zero entropy. Clearly, the disregarded nonzero-temperature effects reduce the accretion rate. In addition, Fig. 4 shows what equation of state can describe an "iron gas" as a function of ρ_∞, which mainly determines ρ.

CONCLUSION

Table 4, which gives accretion rates over a wide range of possible initial densities ρ_∞ from 10^4 to 5×10^6 g cm^{-3} in the iron atmosphere of a protoneutron star without rotation ($j_0 = 0$), shows that steady accretion proceeds at a high rate, at least about $1M_\odot$ in 0.1 s. The rotation that we took into account above could be considered as an obstacle to accretion, but, as we see from Tables 1 and 2 [for the characteristic values of P_1 corresponding to $\rho_\infty = 10^4$ g cm^{-3} (Table 1) and $\rho_\infty = 5.66\times10^5$ g cm^{-3} (Table 2)], it is marginal: the accretion rate decreases as $P_3^{1/2}$ from 0.3% (Table 1) to 1.3% (Table 2) at an almost maximum possible value of $P_2 = 0.022$. We emphasize that a reduction in accretion rate due to nonrelativistic effects in "iron gas" electrons compared to the well-known estimate based on Bondi's formula, to which the above asymptotic of $A_{4/3}$ corresponds, plays no significant role either. However, because of this reduction, the accretion velocity at the sonic point is almost half the free-fall velocity (see Figs. 2, 3).

Thus, according to our solutions, the lifetime of a protoneutron-star iron atmosphere is short for spherically symmetric steady accretion, despite the centrifugal force impeding the accretion. Nevertheless, the important question as to the time scales on which our steady-state solution is established should be analyzed. The calculated parameters f and g, even for $\rho_\infty = 5.66\times10^5$ g cm^{-3}, primarily suggest that the region of the steady-state solution far exceeds in characteristic size the cavity of the initial stellar iron core, according to relations (52). We obtain $r_s = 1.18\times10^9$ cm and $r_c = 4.39\times10^9$ cm for the above density, while the cavity radius is $R_{Fe} = 4.38\times10^8$ cm. In other words, the steady-state solution does not fit into the core cavity, and, therefore, cannot be established even on time scales $t_s \cong \frac{r_s}{V_s} \cong \frac{1.2\times10^9}{4.8\times10^8} \sim 3$ s and $t_c \cong \frac{r_c}{V_c} \sim 12$ s. However, a toroidal equilibrium iron atmosphere can be formed (given the rotation effects) on these time scales, which was considered in detail by Imshennik and Manukovskiĭ (2000). It lies within the iron-core cavity, and the rotational effects in it at a given total angular momentum $J_0 \cong (1–5)\times10^{49}$ erg s completely balance the iron atmosphere with the general equation of state of a completely ionized and degenerate electron gas.

The additional condition for the derivatives of the fall velocity and of the speed of sound being equal at the sonic velocity used here, which is equivalent to the condition for the derivative of the Mach number being zero, should also be further analyzed. As our calculations of the flow itself show, this condition is consistent with our computational data (see Figs. 2, 3) not only in parameters of the sonic point, but also in the fact that the $V(r)$ and $a(r)$ curves are in contact at the sonic point (of course, in a qualitative sense). Our technique allows the complex procedure of seeking for the unique solution (Spitzer 1981) to be avoided for the complex equation of state that we used.

ACKNOWLEDGMENTS

We wish to thank K.V. Manukovskiĭ for taking an active part in discussions.

REFERENCES

1. H. Bondi, Mon. Not. R. Astron. Soc. **112**, 195 (1952).
2. G. E. Brown, S. W. Bruenn, and J. S. Wheeler, Comments Astrophys. **16**, 153 (1992).
3. V. S. Imshennik and K. V. Manukovskiĭ, Pis'ma Astron. Zh. **26**, 917 (2000) [Astron. Lett. **26** (12), 788 (2000)].
4. V. S. Imshennik and D. K. Nadyozhin, Pis'ma Astron. Zh. **18**, 195 (1992) [Sov. Astron. Lett. **18**, 79 (1992)].

5. L. D. Landau and E. M. Lifshitz, *Fluid Mechanics* (Nauka, Moscow, 1986; Pergamon, New York, 1987).
6. L. D. Landau and E. M. Lifshitz, *Statistical Physics* (GITTL, Nauka, Moscow, 1951; Pergamon, Oxford, 1980).
7. V. M. Lipunov, *Astrophysics of Neutron Stars* (Nauka, Moscow, 1987).
8. D. K. Nadyozhin, Astrophys. Space Sci. **51**, 283 (1977).
9. D. K. Nadyozhin, Surv. High Energy Phys. **11**, 121 (1998).
10. L. I. Sedov, *Similarity and Dimensional Methods in Mechanics* (GITTL, Moscow, 1957; Academic, New York, 1959).
11. L. Spitzer, Jr., *Physical Processes in Interstellar Medium* (Wiley, New York, 1978; Mir, Moscow, 1981).
12. Ya. B. Zel'dovich and I. D. Novikov, *Gravitational Theory and Stellar Evolution* (Nauka, Moscow, 1981).

Translated by V. Astakhov

Astronomy Letters, Vol. 27, No. 2, 2001, pp. 91–94. Translated from Pis'ma v Astronomicheskiĭ Zhurnal, Vol. 27, No. 2, 2001, pp. 112–116.

Oscillatory Propagation of an Ionization–Shock Front

K. V. Krasnobaev*

Moscow State University, Vorob'evy gory, Moscow, 119899 Russia

Received June 7, 2000

Abstract—Based on numerical simulations, we show that the oscillatory propagation of a plane-parallel ionization-shock front is possible for a typical dependence of the interstellar-medium cooling function on density and temperature. In this case, the oscillation amplitude of the shock position in the presence of an ionization front can be several times larger than its value for a single shock wave. The variations in neutral and ionized gas velocities attributable to oscillations are comparable in order of magnitude and agree with the random velocities observed in H II regions. © *2001 MAIK "Nauka/Interperiodica".*

Key words: *interstellar medium, H II regions, shock waves, ionization fronts, instability*

INTRODUCTION

In the literature, much attention is currently given to shock stability under conditions of strong radiative cooling of the postshock gas. The interest in this problem stems from the numerous astrophysical phenomena characterized by the propagation and interaction of radiative shock waves (supernova remnant expansion, interactions of stellar winds with circumstellar gas, and accretion flows).

A linear analysis and direct numerical calculations by Langer *et al.* (1981), Chevalier and Imamura (1982), Imamura *et al.* (1984), and Strickland and Blondin (1995) indicate that plane one-dimensional shocks can be unstable in a gas with radiative cooling if the increase in cooling rate with temperature behind the shock front is not too rapid. In this case, finite-amplitude oscillations in the shock position arise at the nonlinear stage of instability development. Such an effect also takes place in the presence of a magnetic field (Kimoto and Chernoff 1997) and when the postshock flow is spherically symmetric (Walder and Follini 1996).

However, the above results refer to the stability of single shock waves, whereas actual flows often include a set of discontinuities (shock wave, tangential discontinuity, ionization and photodissociation fronts, etc.). We therefore consider below the possibility of oscillatory propagation of a shock wave–ionization front system (ionization–shock front), which is typical of expanding H II regions. Our goal is to determine the effect of an ionization front (I-front) and the form of the cooling function on the perturbation amplitude and spectrum, as well as to estimate the possible contribution of oscillations to the observed gas velocity variations in H II regions.

STRUCTURE OF THE POSTSHOCK FLOW IN A GAS WITH RADIATIVE COOLING AND THE INSTABILITY DEVELOPMENT MECHANISM

The general pattern of variations in postshock gas parameters with allowance for radiative cooling is well known (see, e.g., the monograph by Baranov and Krasnobaev 1977): a zone of dramatic increase in density ρ and decrease in temperature T and particle velocity u at a relatively modest increase in pressure p (relaxation zone) immediately follows an adiabatic discontinuity.

Nevertheless, to determine the relaxation-zone size L_c and the distribution of gas-dynamical quantities inside this zone requires analyzing the flow properties in more detail.

Let us consider a plane one-dimensional unsteady gas motion with volume heat losses through radiative cooling. The system of equations for this motion is

$$\begin{gathered}\frac{\partial\rho}{\partial t}+\frac{\partial\rho u}{\partial x}=0,\\ \frac{\partial u}{\partial t}+u\frac{\partial u}{\partial x}+\frac{1}{\rho}\frac{\partial p}{\partial x}=0,\\ \frac{\partial}{\partial t}\left(\frac{1}{\gamma-1}\frac{p}{\rho}\right)+u\frac{\partial}{\partial x}\left(\frac{1}{\gamma-1}\frac{p}{\rho}\right)+\frac{p}{\rho}\frac{\partial u}{\partial x}=-\frac{\Lambda}{\rho},\\ p=\frac{\rho kT}{\mu m_{\mathrm{H}}},\end{gathered}\qquad(1)$$

where t and x are the time and spatial coordinate, respectively; $\gamma = 5/3$ is the adiabatic index; Λ is the amount of energy lost by a unit gas volume per unit time through radiative processes; k is the Boltzmann

* E-mail address for contacts: vkkaor22@mtu-net.ru

constant; μ is the mean molecular weight of gas particles, which below is taken to be unity unless specified otherwise; and m_H is the hydrogen atomic mass. Next, we assume that $\Lambda = \Lambda(\rho, T)$; for typical interstellar conditions, we can also assume that $\Lambda = \rho^2\varphi(T)$ (Kaplan and Pikel'ner 1979) and that $\varphi(T)$ is proportional to the cooling efficiency (Bochkarev 1992).

Let the shock coordinate in a steady state, when $\partial/\partial t = 0$, be $x_s = 0$ and the parameters of the incoming homogeneous flow be ρ_0, u_0, T_0, $M_0^2 = \rho_0 u_0^2/\gamma p_0$ at $x < 0$. We denote the corresponding quantities immediately behind the adiabatic discontinuity by ρ_s, u_s, T_s, and M_s. We can then easily estimate L_c from the energy equation (Strickland and Blondin 1995)

$$L_c = \frac{kT_s}{m_H}\frac{\rho_s u_s}{\Lambda(\rho_s, T_s)}. \quad (2)$$

We see from (2) that, if the characteristic cooling time L_c/u_s increases with shock velocity (i.e., with T_s), an excess (relative to the steady state corresponding to the changed discontinuity velocity) pressure arises behind the discontinuity. Having reflected from the boundary of the region occupied by a dense cold gas, this pressure perturbation is capable of accelerating the shock front further (Strickland and Blondin 1995). Of course, this instability mechanism is efficient only in the presence of a sufficiently sharp transition zone between the heated and cold gas. The variations of ρ, u, and T in this zone can be easily determined by numerically integrating the system of equations (1), which reduces to a system of ordinary differential equations for steady motion. However, let us derive an approximate analytic dependence of ρ, u, and T on x, which is especially useful in selecting parameters of numerical simulations for the oscillatory propagation of a shock wave or a set of discontinuities with the relaxation zone. For this purpose, we take into account the fact that, as was mentioned above, the pressure change in the relaxation zone is not too large, and, to a first approximation, we can assume that $p = p_s = \text{const}$ at all $x > 0$. We then derive the following equation for $T(x)$ from (1):

$$\frac{\gamma L_c}{\gamma - 1}\left(\frac{T}{T_s}\right)^2\frac{d}{dx}\left(\frac{T}{T_s}\right) = -\frac{\varphi(T)}{\varphi(T_s)}. \quad (3)$$

Integrating (3) yields

$$\frac{x}{L_c} = -\frac{\gamma}{\gamma - 1}\int_1^{T/T_s}\frac{\varphi(T_s)}{\varphi(T)}\left(\frac{T}{T_s}\right)^2 d\left(\frac{T}{T_s}\right). \quad (4)$$

Relation (4) allows us to determine the value of $x = x_c$ at which the postshock gas temperature is equal to T_0, and further cooling is insignificant (x_c is often taken as the exact coordinate of the relaxation-zone boundary). Specifically, for a power law $\varphi(T) \propto T^\alpha$, we find that

$$\frac{x_c}{L_c} = \frac{\gamma}{\gamma - 1}\frac{1}{3 - \alpha}\left[1 - \left(\frac{T_0}{T_s}\right)^{3-\alpha}\right]. \quad (5)$$

Formula (5) clearly gives a slightly overestimated value of x_c. However, it differs from the results of numerical calculations only slightly in the α range –1/2 to 1/2 of interest. The existence (at $x \approx x_c$) of a narrow zone with steep T, ρ, and u gradients when $M_0 \gg 1$ predicted by relation (4) is also corroborated by calculations.

EFFECTS OF THE COOLING EFFICIENCY ON SINGLE-SHOCK OSCILLATIONS

The nonlinear stage of perturbation development was extensively studied by Strickland and Blondin (1995) for $\varphi \propto T^\alpha$ and $0 \le \alpha \le 1$. Instability manifested itself at sufficiently large M_0 for $\alpha \le 0.75$. Kimoto and Chernoff (1997) used a more complex form of the cooling function, including negative α, when taking into account a magnetic field. However, their calculations were mainly applied to the dynamics of supernova remnants, so the shock velocity was 150–240 km s^{-1} and the cooling was disregarded if $T \le 2 \times 10^4$ K. However, the shock velocity is ~10–20 km s^{-1} and $T_0 \sim 10^2$ K when H II regions expand. Naturally, the temperature dependence of the cooling efficiency is also different. Therefore, before considering the motion of an ionization–shock front, we turn to our calculations of the propagation of a single shock in the circumstellar gas.

The calculations were performed by using a monotonic difference scheme of the second approximation order. An adaptive movable grid was used to increase the calculation accuracy in the vicinity of $x \approx x_c$. The cooling was assumed to be insignificant if $T < T_0$. However, for convenience of calculations, we assumed that the ambient temperature could not fall below T_0.

We performed a test calculation with parameters close to those used by Strickland and Blondin (1995): $\alpha = 0.0$ and $M_0 = 40$. At the initial instant of time, an impermeable wall was placed in the flow behind the shock at a distance $x = 0.08L_c$. Figure 1 plots $x_s(t)$ (below, x_s and t are given in units of L_c and L_c/u_0, respectively). We can see that, despite some differences in the statement of the boundary conditions, the oscillation amplitude and period satisfactorily agree with those obtained previously by different methods (Imamura *et al.* 1984; Wolf *et al.* 1989; Strickland and Blondin 1995).

As applied to the expansion of H II regions, let us consider the temperature dependence of the cooling function, which corresponds to the well-known (below denoted by φ_{ism}) cooling efficiency of the interstellar medium [see, e.g., the monographs by Kaplan and Pikel'ner (1979), Spitzer (1981), and Bochkarev (1992)].

The function φ_{ism} is characterized by the presence of a plateau at temperatures slightly lower than 10^4 K and by a sharp decrease with decreasing temperature at $T \le$

10^3 K. Consequently, one might expect the oscillations in shock front position to have a fairly large amplitude only if the shock velocity (and, hence, T_s) is high enough. In this case, T_s, of course, cannot exceed the values corresponding to the sharp rise in φ_{ism} at $T \geq 10^4$ K due to the excitation of the hydrogen second level.

This assumption is corroborated by direct calculations. The function φ_{ism} was chosen according to data from the monograph of Spitzer (1981) and was interpolated by using a Lagrange polynomial. The degree of ionization of the gas incident on the shock front was taken to be 10^{-2}. The calculated $x_s(t)$ is shown in Fig. 2 for $u_0 = 10$ and 17 km s^{-1} (T_s are 2.33×10^3 and 6.74×10^3 K, respectively; $M_0 = 10$). We can see that the oscillation amplitude considerably increases when T_s lies in the φ_{ism} plateau region.

It should be noted that the curves in Fig. 2 were constructed by using "soft" boundary conditions at $x \approx 10L_c$. The initial conditions were the same as those in Strickland and Blondin (1995), but the "compression" coefficient along the x coordinate was taken to be 0.95.

IONIZATION–SHOCK FRONT OSCILLATIONS

Comparing the perturbation amplitudes and spectra of $x_s(t)$ in Figs. 1 and 2, we can easily see how significant the conditions of pressure-wave reflection from the boundaries of the region occupied by a dense cold gas are. Thus, the ionization front located at some distance from the shock can appreciably affect the oscillation characteristics. A linear analysis of the interaction between a shock wave–ionization front system and an inhomogeneous interstellar medium (Krasnobaev *et al.* 1994) also points to a similar possibility.

Let, as above, $x_s(0) = 0$ in an unperturbed state and the I-front coordinate be $x_I(0) = L$. We assume that, at the initial instant of time, the front velocities are the same, the plasma behind the I-front is completely ionized (i.e., $\mu = 1/2$) and transparent to the ionizing radiation, and its motion is isothermal.

Since the ionization front is considered as a discontinuity, it is convenient to change to new variables ξ, τ in (1): $t = \tau$ and $x = \xi + x_I(t) - x_I(0)$. The ionization front coordinate in ξ, τ variables is fixed. This allows us to use the above method of calculation (only the ordinary conditions of passage through the I-front, which is assumed to be a D-type front, are added).

As our calculations indicate, the effect of the I-front on the behavior of $x_S(t)$ and $x_I(t)$ is largely determined by the separation L between the fronts at the initial instant of time. This effect is illustrated by Fig. 3, which shows the positions of the shock and ionization fronts for L equal to 1.05 and 1.15. In this case, we used the same initial and boundary conditions as those in Fig. 2: $u_0 = 17$ km s^{-1} and $M_0 = 10$. The ratio of the neutral and ionized gas densities λ at $t = 0$ is taken to be 80.

A comparison of the curves in Figs. 2 and 3 indicates that the presence of an I-front can increase the

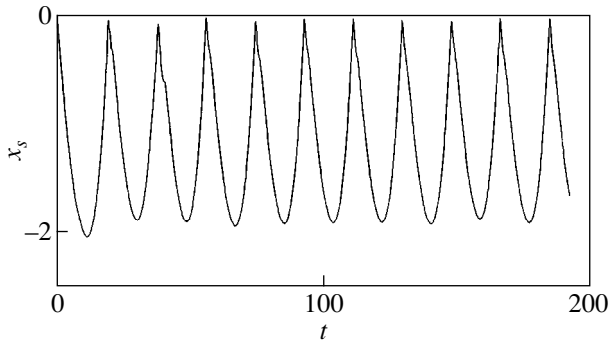

Fig. 1. The $x_s(t)$ curve in the case of a supersonic onflow on the wall.

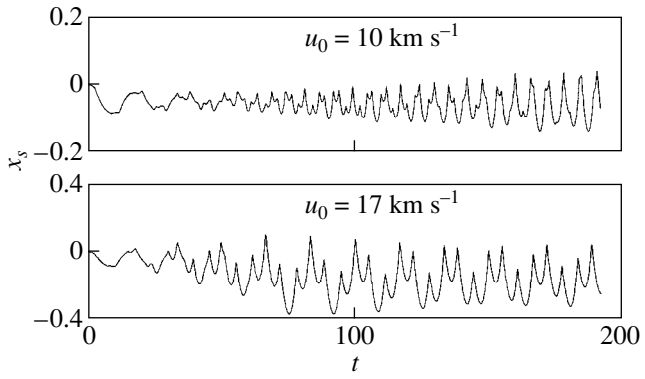

Fig. 2. Oscillations in the position of a single shock.

oscillation amplitude severalfold. Waves with periods close to the main period (according to the classification of the linear theory, the main period is approximately equal to $21L_c/u_0$) are generated when the shock velocity is such that T_s lies in the φ_{ism} plateau region. As follows from the curves in Fig. 2, the higher frequency components dominate in the front oscillation spectrum at lower T_s. Another important feature of the motion is that the variations in neutral (u_n) and ionized (u_i) gas velocities are of approximately the same order of magnitude, with the variations for u_n being even slightly larger than those for u_i (Fig. 4 shows u_n and u_i in the immediate vicinity of the ionization front at $L = 1.15$; the remaining parameters are the same as those in Fig. 3). We emphasize that $u_i/u_n = \lambda \gg 1$ in an unperturbed flow.

Thus, despite the fairly complex form of the cooling function, the oscillatory propagation of an ionization–shock front can take place for typical conditions in the interstellar medium.

DISCUSSION AND CONCLUSIONS

It is well known that to maintain the observed random motions in H II regions requires an energy input from external sources. These can be produced, in particular, by gas outflow from neutral condensations, stellar wind outflow, and the development of some instability. Our results are therefore of considerable interest,

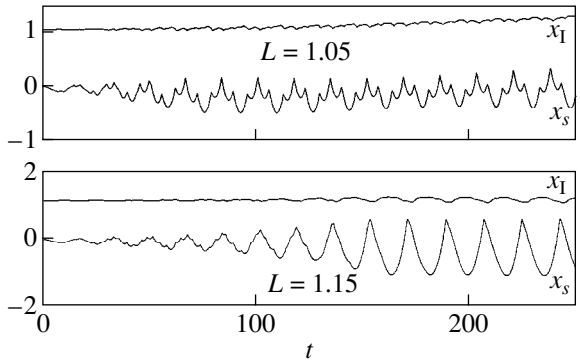

Fig. 3. Shock $x_s(t)$ and ionization $x_I(t)$ front coordinates versus time.

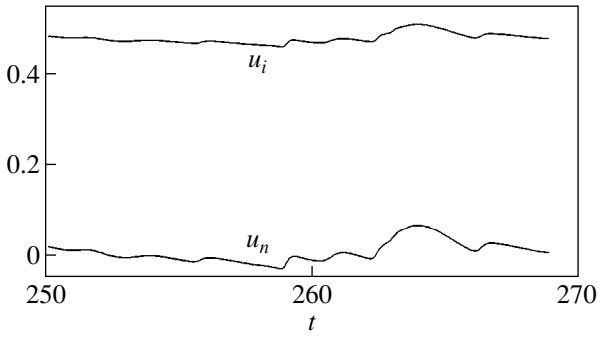

Fig. 4. Temporal variations in neutral and ionized gas velocities (in units of u_0) on both sides of the ionization front.

because acoustic (or weak shock) waves can be generated in H II regions.

Let us estimate the characteristic scales of the perturbations produced by ionization–shock front oscillations and the amplitude of velocity variations by using the results of our calculations. For $\varphi = \varphi_{ism}$, $u_0 = 17$ km s^{-1}, and $M_0 = 10$, we then obtain $L_c \approx 1.2 \times 10^{18}\, m_H/\rho_0$. The corresponding lengths of the waves penetrating into H II regions are about $10L_c$ or smaller, and the velocity deviations from the mean are 1 km s^{-1}, in agreement with velocity-dispersion observations in H II regions (although higher random velocities are also observed). Thus, the H II region boundary can serve as the source of turbulent motions both in the ionized gas and in the neutral gas compressed by a shock wave.

In conclusion, we note that it makes sense to further generalize the flow model used above. Thus, the fact should be taken into account that the ionization- and shock-front velocities slightly differ for expanding H II regions, whereas they were assumed to be equal in our calculations. A change in plasma ionization composition under the effect of energetic photons leaving the H II region, whose mean free path in a neutral gas exceeds the ionization-front thickness, can also affect the oscillation characteristics. The establishment of thermal and ionization balance near the I-front can also have a significant effect (Krasnobaev and Tarev 1997).

In general, our calculations lead us to the following conclusions.

(1) The oscillatory propagation of an ionization–shock front is possible for a typical dependence of the cooling function for the interstellar medium on density and temperature.

(2) At the saturation stage, the characteristic perturbation scale and amplitude are determined by wave interference in the layer between the fronts. In this case, the oscillation amplitude of the shock position in the presence of an I-front can increase severalfold and be comparable to the cooling zone size.

(3) The variations in neutral and ionized gas velocities attributable to oscillations are of the order of the observed random velocities. Thus, the ionization–shock front instability can be considered as one of the turbulization mechanisms for H II regions.

REFERENCES

1. V. B. Baranov and K. V. Krasnobaev, *Hydrodynamic Theory of Cosmic Plasma* (Nauka, Moscow, 1977).
2. N. G. Bochkarev, *Foundations of the Physics of Interstellar Medium* (Mosk. Gos. Univ., Moscow, 1992).
3. R. A. Chevalier and J. N. Imamura, Astrophys. J. **261**, 543 (1982).
4. J. N. Imamura, M. T. Wolff, and R. H. Durisen, Astrophys. J. **276**, 667 (1984).
5. S. A. Kaplan and S. B. Pikel'ner, *Physics of Interstellar Medium* (Nauka, Moscow, 1979).
6. P. A. Kimoto and D. F. Chernoff, Astrophys. J. **487**, 728 (1997).
7. K. V. Krasnobaev, N. E. Sysoev, and V. Yu. Tarev, in *Nuclear Physics, Physics of Cosmic Radiation, Astronomy* (Mosk. Gos. Univ., Moscow, 1994), p. 222.
8. K. V. Krasnobaev and V. Yu. Tarev, Astron. Zh. **74**, 671 (1997) [Astron. Rep. **41**, 594 (1997)].
9. S. H. Langer, G. Chanmugam, and G. Shaviv, Astrophys. Lett. **245**, 23 (1981).
10. L. Spitzer, Jr., *Physical Processes in Interstellar Medium* (Wiley, New York, 1978; Mir, Moscow, 1981).
11. R. Strickland and J. M. Blondin, Astrophys. J. **449**, 727 (1995).
12. R. Walder and D. Follini, Astron. Astrophys. **315**, 265 (1996).
13. M. T. Wolff, J. H. Gardner, and K. S. Wood, Astrophys. J. **346**, 833 (1989).

Translated by Yu. Safronov

Astronomy Letters, Vol. 27, No. 2, 2001, pp. 95–98. Translated from Pis'ma v Astronomicheskiĭ Zhurnal, Vol. 27, No. 2, 2001, pp. 117–121.

Infrared Speckle Interferometry of Eleven Binaries Using a Bispectral Analysis

I. I. Balega[1]*, Yu. Yu. Balega[1], K.- H. Hofmann[2], and G. Weigelt[2]

[1] *Special Astrophysical Observatory, Russian Academy of Sciences, Nizhniĭ Arkhyz, Stavropol kraĭ, 357147 Russia*
[2] *Max-Planck-Institut für Radioastronomie, Bonn, 53121 Germany*

Received July 5, 2000

Abstract—Infrared speckle-masking observations of eleven binary systems with the 6-m Special Astrophysical Observatory telescope are presented. A resolution of 43 mas in *J* (1.25 μm) and 76 mas in *K* (2.2 μm) has been achieved in reconstructed images. Accurate magnitude differences, separations, and position angles have been determined for all the resolved binaries. The pair HR 1071 with an abnormally low lithium abundance is considered in more detail. © *2001 MAIK "Nauka/Interperiodica".*

Key words: *binaries, speckle interferometry*

INTRODUCTION

Speckle interferometry allows one to significantly increase the angular resolution and accuracy of binaries' measurements and to fill the gap between spectroscopic and visual pairs. The most interesting binaries with rapid orbital motion are regularly observed interferometrically with the world's largest telescopes. However, most of the results are currently published with a ±180° uncertainty in the position angle and are not accompanied by relative photometry of the components. At the same time, speckle masking (Weigelt 1977; Lohmann *et al.* 1983; Hofmann and Weigelt 1986) provides a means for obtaining the real images of multiple stars and, hence, eliminates the position-angle uncertainty and makes it possible to estimate the magnitude difference.

Below, we present the first results of our image reconstruction by speckle masking for eleven binary systems observed with the 6-m telescope in the infrared. The diffraction-limited resolution for a 6-m aperture was achieved for all the binaries studied.

OBSERVATIONS AND DATA REDUCTION

We obtained speckle data with the 6-m telescope in April and October 1996 and in October 1997. Speckle interferograms were taken through infrared *J*, *H*, and *K* filters with the following central wavelengths and halfwidths: 1238/276 nm (*J*), 1613/304 nm (*H*), 2165/328 nm (*K′*), and 2191/411 nm (*K*). The detector was a NICMOS-3 camera (a 256 × 256 HgCdTe array sensitive in the range 1 to 2.5 μm with a frame rate of 2 s^{-1}). The detector pixel size corresponds to 15 mas in *J*, 20 mas in *H* and *K′*, and 31 mas in *K*. The field of view is 3.″8, 5.″1, 5.″1, and 7.″9 in *J*, *H*, *K′*, and *K*, respectively. During our observations, we estimated the seeing corrected for low-frequency fluctuations to be in the range 0.″9 to 1.″9 (FWHM). From 150 to 780 speckle interferograms were taken for each object with exposures from 50 to 300 ms.

The images were reconstructed with a diffraction-limited resolution by speckle masking. The sequence of image-reconstruction steps was described by Hofmann *et al.* (1995). The bispectrum of each frame consisted of 30–100 million pixels. No image postprocessing was performed; we achieved a diffraction-limited resolution of 43 mas in *J*, 57 mas in *H*, and 76 mas in *K*.

The geometric calibration was based on observations of binaries with accurately determined relative positions: Kui 8 and 15, as well as ADS 3734, 11 558, 12 239, 14 575, 7704, 8708, 10 184, and 10 850. Data on these pairs were taken from the Washington Visual Double Star Catalog (Worley and Douglas 1997). The scale calibration error is ±0.2%. Intensity ratios, separations, and position angles for the components were estimated from measurements of the objects' visibility function by least squares. The visibility function of an object is the average power spectrum of speckle interferometry (Labeyrie 1970) divided by the atmospheric transfer function, which can be determined from observations of a star unresolvable by the telescope.

RESULTS AND DISCUSSION

Our measurements of the relative positions and magnitude differences for eleven binaries are presented in the table. The first three columns contain, respectively, the Washington Catalog numbers (Worley and

* E-mail address for contacts: balega@sao.ru

Astrometry and photometry for the observed binaries

Coordinates (2000)	Name/catalog	Discoverer	Epoch 1990+	θ, deg	σ_{θ°	ρ, mas	σ_ρ, mas	Δm	$\sigma_{\Delta m}$	Band
03337+5752	HR 1071	CHR 117	6.750	274.1	1.0	136.5	2.0	0.45	0.18	*J*
			7.808	287.0	1.5	126.1	2.0	0.10	0.20	*K*'
03448+4602	GL 150.2	Bag 8	6.750	92.2	1.0	243.7	1.5	1.67	0.12	*J*
04044+2406	36 Tau A	McA 13	7.808			UR				*K*'
04063+1952	BD+19662	Bag 4	7.808	*276.9	2.0	58.2	4.0	0.57	0.30	*K*'
04356+1010	88 Tau A	CHR 18	7.791	134.0	1.0	211.4	2.5	1.29	0.12	*K*'
			7.791	134.3	1.0	209.9	2.5	1.37	0.15	*H*
	88 Tau B		7.791			UR				*K*'
15521+1043	GL 600	Bag 7	6.260	68.4	1.0	115.3	2.0	0.20	0.14	*K*
16584+3943	BD+393062	Cou 1289	6.260	246.7	1.5	117.9	3.0	0.66	0.20	*K*
18001+8000	41 Dra	Bag 6	6.260	321.1	1.0	111.3	1.5	0.47	0.12	*K*
			6.747	325.3	1.0	108.6	1.5	0.51	0.12	*K*
			6.747	325.0	1.0	109.1	1.5	0.46	0.12	*K*'
			6.747	325.2	1.0	108.3	1.5	0.63	0.14	*J*
19391+7625	GL 765.2	Mlr 224	7.789	303.3	1.0	165.7	1.5	0.42	0.20	*K*'
			7.789	303.0	1.0	165.9	1.5	0.47	0.20	*J*
21118+5959	ADS 14749	Stf 2780	7.789	214.5	1.0	1023.9	3.0	1.32	0.12	*H*
			7.789	214.6	1.0	1026.0	3.0	1.06	0.12	*K*'
	ADS 14749A	McA 67	7.789	*158.1	2.0	37.8	3.0	0.51	0.30	*H*
22388+4419	ADS 16138	Ho 295	6.750	135.4	2.0	46.7	2.0	0.30	0.14	*J*

Douglas 1997) or coordinates for the epoch 2000, the star names or cataloged numbers, and the discoverers. The fourth column gives the epochs of observations, in fractions of a Bessel year. The next four columns list the measured position angles θ, angular separations ρ, and the corresponding errors. The magnitude differences and errors are given in the next two columns. When determining the total error, we took into account the reconstruction and calibration errors. The retained ±180° position-angle uncertainty for very close pairs is marked by an asterisk. Finally, the last column lists the filters used. The note "UR" is used for unresolved stars. Comments to some measurements are given below. The images reconstructed with a diffraction-limited resolution by speckle interferometry and bispectral estimation are shown in the figure.

CHR 117. This lithium-poor star belonging to the old disk population was studied in detail by McAlister *et al.* (1992). Based on eight speckle observations of the pair, they determined a preliminary orbit with a period of 13.8 years. Recently, Soederhjelm (1999) has proposed a new orbit solution based on the same ground-based speckle data and Hipparcos astrometric measurements. Since the solution was obtained for a fixed mass ratio, the total error of the orbital elements is too large for a detailed astrophysical analysis of the binary. Our *J* and *K*' measurements of the pair, which almost complete a full orbital ellipse, confirm a small magnitude difference between the components (mean $\Delta m = 0.30$), as suggested by McAlister *et al.* (1992) using *V* speckle measurements. Given these new data, the adjusted orbital elements for CHR 117 are very close to the solution of Soederhjelm (1999); only the period can be determined more accurately: $P = 14.46 \pm 0.07$ years. Therefore, Soederhjelm's parallax and sum of masses for this binary may be considered to be realistic enough.

McAlister *et al.* (1992) discussed an interesting question of the lithium deficiency in the spectrum of CHR 117. The constant magnitude difference over a wide spectral range leads us to conclude that the pair's components are of approximately the same spectral type. It is therefore unlikely that the rise in continuum due to the presence of a companion with the resulting decrease in line equivalent width could be responsible for the low Li abundance. Because of the slow rotation of both components (5 km s^{-1}), the meridional circulation responsible for the mixing of stellar matter in the emitting envelope cannot be considered as a cause of the anomalous Li abundance on the stellar surface either. A plausible explanation could be a tidal interaction between the components, which enhances turbulent gas mixing accompanied by lithium destruction. Indeed, a comparison of the He, C, and N abundances in single and binary main-sequence stars reveals a correlation between chemical anomalies and the presence of a companion (Leushin 1989). The strength of anomalies depends on tidal deceleration, which is related to the separation between the components and to their evolutionary status. Whether tidal deceleration is the main mechanism of gas mixing in binary systems with separations of 4 or 5 AU, as in the case of CHR 117, can be directly determined by using spectroscopic observations.

Bag 8. The close separation between the components at a magnitude difference of 2^m could be the rea-

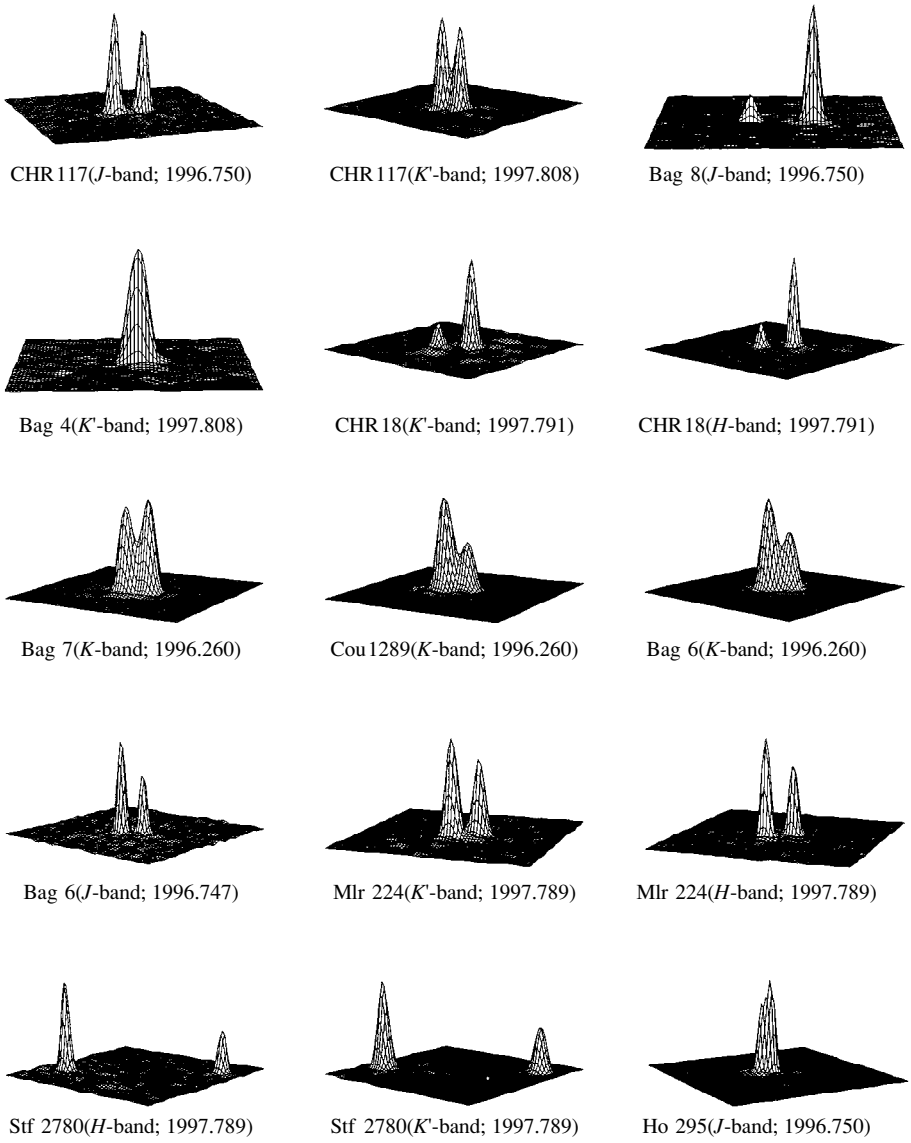

The images of binaries reconstructed with a diffraction-limited resolution by bispectral speckle interferometry. Spectral bands and epochs of observations are given in parentheses.

son why Hipparcos did not resolve this binary. Relative *J* photometry supports the assumption that the companion is a late K or early M dwarf. Since the first resolution in 1993.8, the relative motion has been too modest to determine a preliminary orbit. Conflicting data are published on the parallax of Bag 8. Balega *et al.* (1997) estimated the photometric parallax from the absolute magnitude and the components' magnitude difference to be 52 mas. The recently published Yale Catalog of Parallaxes (van Altena *et al.* 1995) gives a trigonometric parallax of 49 ± 15 mas for this star, whereas Eggen (1998) included the star in his stellar kinematic and metallicity survey in the solar neighborhood with a photometric parallax of 43 mas. However, the Hipparcos parallax is considerably smaller: 37.6 ± 1.1 mas. This discrepancy is difficult to explain even if the orbital motion in the binary system is assumed to have affected the Hipparcos determination of the star image photocenter. Over the period of the Hipparcos mission, the companion's relative motion could lead to a displacement of the image centroid by approximately 5 mas.

McA 13. During our observations, the components were too close to be resolvable with the 6-m telescope in *K*'.

Bag 4. Lunar-occultation observations yielded a magnitude difference of 0.18–0.47 in the wavelength range 500–610 nm (Schmidtke and Afrikano 1984; Evans *et al.* 1985), while our estimate in *K*' is $\Delta m = 0.57 \pm 0.30$. Assuming a total spectral type of F0 V, a visual magnitude of $8\overset{m}{.}66$, and $\Delta m = 0.4$, we roughly estimated the binary's parallax to be $\pi = 5$ mas. Based on twelve speckle measurements of the pair, we computed a preliminary circular orbit: $P = 30\overset{d}{.}68$, $T =$

1990.96, $e = 0.045$, $a = 79$ mas, $i = 128°$, $\Omega = 50°$, and $\omega = 32°$. However, we will have to wait for another ~10 years to obtain a reliable solution. It is difficult to explain why Bag 4 was not resolved with the 4-m Kitt Peak National Observatory telescope in 1991.8 and 1993.2, when the separation in the pair exceeded 60 mas (Mason 1996). This epoch of observations can be useful for improving the orbit quality.

Bag 7. The small *K* magnitude difference confirms the identification of this star with the double-lined spectroscopic pair first discovered by Tokovinin (Balega *et al.* 1991). At present, a combined speckle spectroscopic orbit with a period of 1000 days can be determined for the binary.

Cou 1289. The expected orbital period for this G0 binary lies in the range 15–40 years. The scatter of relative-position measurements is so far too large to obtain an acceptable orbit solution.

Bag 6. There is a slight discrepancy between the Hipparcos parallax of 18.8 mas and the dynamical parallax of 22.9 mas following from the orbit of Balega *et al.* (1997).

Mlr 224. A refined orbit solution for this pair with allowance for radial-velocity measurements is being prepared.

McA 67. This pair of massive B0 II stars is a member of the multiple system ADS 14 749 lying 1° from the center of the Cepheus OB2 association, which was formed during the fragmentation of a giant expanding gaseous envelope. The star is partially resolved only in *H*. From a position-angle change of ~3° in a year, one might expect the orbital period to be about 120 years. The visual companion of ADS 14 749B is unresolvable with the 6-m telescope in the infrared.

CONCLUSION

The limiting angular resolution of the 6-m telescope in the infrared *K* band (2165 nm) corresponds to the resolution of a 1.5-m telescope in the green visible band. The accuracy of determining the relative positions of components is also lower. At the same time, infrared observations of binaries can also be performed when visible interferometry becomes virtually inapplicable because of atmospheric conditions. The procedure for subtracting shifts in the image power spectrum caused by photon and detector noise simplifies significantly in the infrared. As a result, the accuracy of estimating the magnitude difference between components increases.

Currently, the interest in infrared observations of close binaries has increased due to the refinement of physical characteristics for lower-main-sequence low-mass stars and the search for brown dwarfs, which can be members of known multiple systems.

We have shown the ability of the 6-m telescope to measure the relative positions of multiple stars and the magnitude difference in the wavelength range 1.2–2.2 μm. The error of position measurements is 0.″002, and the mean photometric error is 0.15 mag.

Our data confirm the orbital parameters for the binary CHR 117 with a low lithium abundance in its spectrum (McAlister *et al.* 1992) and suggest that its anomalous chemical composition may be associated with its binary nature.

We have established a significant discrepancy between the parallax of the pair Bag 8 (GL 150.2) and the Hipparcos data.

We have estimated the orbital period *T* for the binary Bag 4 of spectral type F0 V to be ≈30 years.

ACKNOWLEDGMENTS

We wish to thank the US Naval Observatory for providing data from the Washington Visual Double Star Catalog. This study was supported in part by the Federal Program “Astronomy.”

REFERENCES

1. I. I. Balega, Yu. Yu. Balega, V. A. Vasyuk, and A. A. Tokovinin, Pis’ma Astron. Zh. **17**, 530 (1991) [Sov. Astron. Lett. **17**, 226 (1991)].
2. I. I. Balega, Yu. Yu. Balega, H. Falcke, *et al.*, Pis’ma Astron. Zh. **23**, 199 (1997) [Astron. Lett. **23**, 172 (1997)].
3. O. J. Eggen, Astron. J. **115**, 2397 (1998).
4. D. S. Evans, D. A. Edwards, M. Frueh, *et al.*, Astron. J. **90**, 2360 (1985).
5. K.-H. Hofmann and G. Weigelt, Astron. Astrophys. **167**, L15 (1986).
6. K.-H. Hofmann, W. Seggewiss, and G. Weigelt, Astron. Astrophys. **300**, 403 (1995).
7. A. Labeyrie, Astron. Astrophys. **6**, 85 (1970).
8. V. V. Leushin, Kinematika Fiz. Nebesnykh Tel **5**, 47 (1989).
9. A. W. Lohmann, G. Weigelt, and B. Wirnitzer, Appl. Opt. **22**, 4028 (1983).
10. B. D. Mason, Astron. J. **112**, 2260 (1996).
11. H. A. McAlister, W. I. Hartkopf, and B. D. Mason, Astron. J. **104**, 1961 (1992).
12. P. C. Schmidtke and J. L. Afrikano, Astron. J. **89**, 1371 (1984).
13. S. Soederhjelm, Astron. Astrophys. **341**, 121 (1998).
14. W. F. van Altena, J. T. Lee, and E. D. Hoffleit, in *The General Catalogue of Trigonometric Stellar Parallaxes* (Yale Univ. Observatory, New Haven, 1995).
15. G. Weigelt, Opt. Commun. **21**, 55 (1977).
16. C. E. Worley and G. G. Douglas, *The Washington Visual Double Star Catalog* (Publ. US Naval Observatory, Washington, 1997).

Translated by V. Astakhov

Astronomy Letters, Vol. 27, No. 2, 2001, pp. 99–107. Translated from Pis'ma v Astronomicheskiĭ Zhurnal, Vol. 27, No. 2, 2001, pp. 122–131.

Line Identification and Photometric Observations of the Future Planetary Nebula IRAS 18 062+2410 = V886 Her in 1997–1999

V. P. Arkhipova[1]*, V. G. Klochkova[2], and G. V. Sokol[1]

[1] *Sternberg Astronomical Institute, Universitetskiĭ pr. 13, Moscow, 119899 Russia*
[2] *Special Astrophysical Observatory, Russian Academy of Sciences, Nizhniĭ Arkhyz, Stavropol kraĭ, 357147 Russia*

Received April 12, 2000; in final form, August 8, 2000

Abstract—Photoelectric *UBV* observations of V886 Her in 1998–1999 have shown that the pattern of its variability is retained: irregular rapid light variations with an amplitude up to $0^m.3$ in *V* and the absence of any correlation between color and magnitude. As previously, the amplitude was at a maximum in *U*, which is most likely attributable to the variable Balmer continuum emitted by stellar wind. A high-resolution spectrum of the star is identified. The overwhelming majority of absorption lines, apart from H I and He I, belong to O II, N II, C II, and Si III. The profiles of hydrogen and helium lines are a superposition of a stellar absorption line with comparatively broad wings and a narrow strong emission feature of the envelope. The He I 5016, 5876, and 7065 Å lines have P Cyg profiles, whereas the remaining helium lines are seen in absorption. The emission spectrum of the envelope is represented by numerous permitted and forbidden lines of ionized metals and by [N II], [S II], and [O I] lines typical of planetary-nebula spectra, as well as by strong O I, N I, and Si II lines. There are no [O III] lines. The radial velocity of the system measured from photospheric absorption features is $\langle V_r$(NII, OII, CII, SiIII)$\rangle$ = +55.72 km s^{-1}, while the mean radial velocity as measured from emission features of the envelope is +50.95 km s^{-1}. The object is most likely an extremely young planetary nebula. © *2001 MAIK "Nauka/Interperiodica".*

Key words: *protoplanetary objects: photometric observations, spectra*

INTRODUCTION

The infrared source IRAS 18 062+2410 was classified as a candidate for protoplanetary objects, future planetary nebulae, in accordance with the criteria for selecting such objects by infrared color indices in the range 10–100 μm (Volk and Kwok 1989). It was optically identified with the fairly bright star SAO 85 766= HDE 341 617.

Optical photometric observations in the mid-1990s (Arkhipova *et al.* 1996, 1998) show that HDE 341 617 is presently a hot star with supergiant characteristics, exhibits light variations within a few tenths of a magnitude, and, most importantly, is evolving "before our very eyes". Available observational data indicate that over a period of 150 years (since the epoch of BD), its temperature has gradually increased, while its mean brightness has varied in accordance with the variation of bolometric correction if the star is assumed to evolve at a constant bolometric luminosity. In the Catalog of Variable Stars, IRAS 18 062+2410 was designated V886 Her.

The mass of the star was estimated by comparing observations with the theory of post-AGB stellar evolution (Blöcker 1995) to be ~0.7$M_\odot$. Calculations of the future evolution of V886 Her predict that it will become the nucleus of a young planetary nebula with a temperature of ~50 000 K in 100 years (Arkhipova *et al.* 1998).

Here, we identify lines in the spectrum of V886 Her, measure its radial velocities, and present new photoelectric *UBV* observations of the star in 1998–1999.

UBV OBSERVATIONS IN 1998–1999

As previously, we carried out our photoelectric *UBV* observations of V886 Her in 1998–1999 at the Crimean Station of the Sternberg Astronomical Institute (SAI) using a 60-cm reflector with a standard *UBV* photometer. The results are given in Table 1. Previous photometric data were published by Arkhipova *et al.* (1996, 1998). Figure 1 shows the star's light and color curves for the entire period of our observations.

The pattern of photometric variability in 1998–1999 remained as before: irregular rapid light variations with an amplitude up to $0^m.3$ in *V*, which are probably attributable to a variable mass-loss rate. There is no correlation between color and magnitude. The amplitude was at a maximum in *U*, which is most likely due to the variable Balmer continuum emitted by the wind.

* E-mail address for contacts: vera@sai.msu.ru

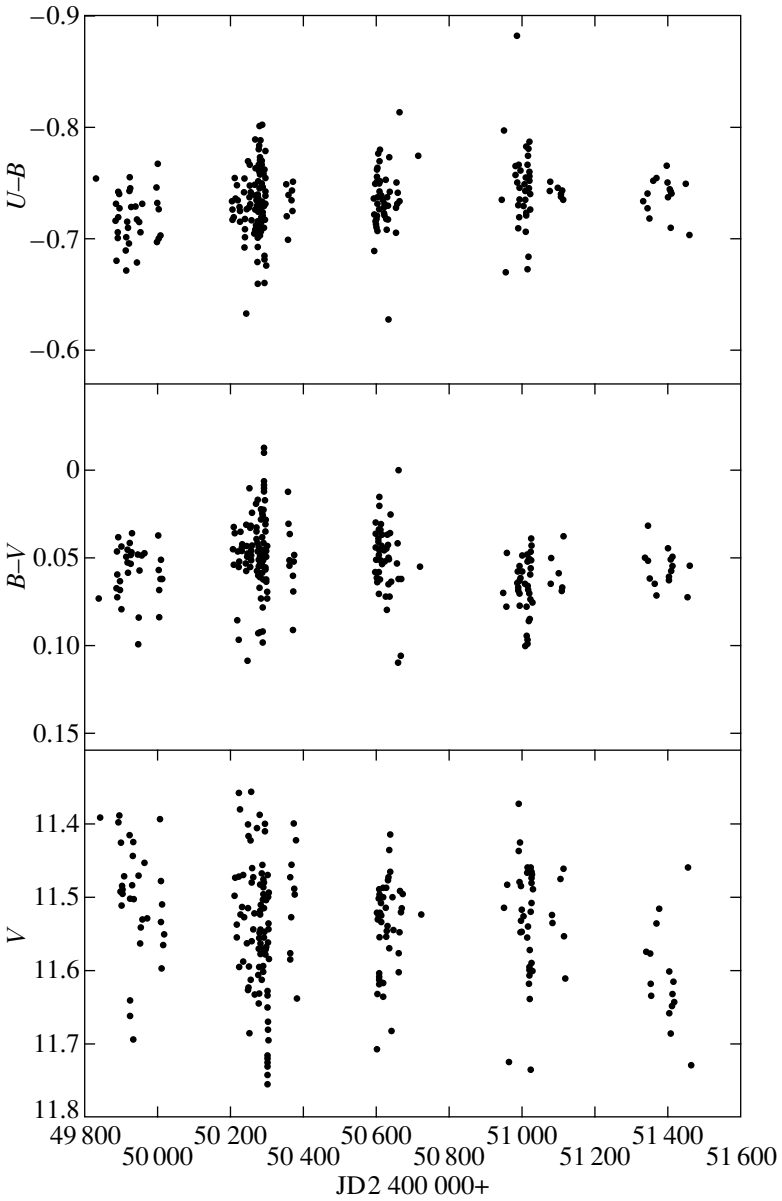

Fig. 1. *V* light and color variations in IRAS 18 062+2410 = V886 Her during 1995–1999.

LINE IDENTIFICATION

On February 26, 1997, a CCD spectrum of V886 Her was obtained at the prime focus of the 6-m Special Astrophysical Observatory (SAO) telescope with the PFES echelle spectrograph (Panchuk *et al.* 1998). The 4340–7600 Å spectrum consists of 23 echelle orders, ~200 Å long each with an overlapping of ~25 Å. The three-pixel resolution (projected entrance slit width) is ~R = 15 000.

The line spectrum of V886 Her is represented by two components: the absorption spectrum of a B1–1.5 supergiant (Arkhipova *et al.* 1998) and the rich emission spectrum of a gaseous envelope superimposed on it.

Using the tables by Moore (1945) and the Catalog of Emission Lines by Meinel *et al.* (1969), we identified lines in the spectrum of V886 Her. Lines in the wavelength range 4340–6500 Å are listed in Table 2[1]. The first column gives the instrumental wavelengths of spectral lines. They were not corrected for the shifts associated with instrumental corrections and the Earth's motion. The subscript "a" or "e" near a wavelength denotes the type of feature: absorption or emission, respectively. The second column contains identification results: the laboratory wavelengths and multip-

[1] Table 2 is published in electronic form only and is accessible via ftp at cdsarc.u–strasbg.fr/pub/cats/J (130.79.128.5) or http://cdsweb.u–strasbg.fr/pub/cats/J.

Table 1. *UBV* observations of V886 Her in 1998–1999

JD 2 400 000 +	*U*	*B*	*V*	*U–B*	*B–V*
50 949.439	10.850	11.585	11.515	−0.735	0.070
50 956.330	10.764	11.561	11.483	−0.797	0.078
50 958.325	11.103	11.773	11.726	−0.670	0.047
50 987.389	10.746	11.503	11.438	−0.757	0.065
50 988.308	10.676	11.441	11.373	−0.765	0.068
50 989.313	10.788	11.538	11.480	−0.750	0.058
50 992.387	10.747	11.498	11.427	−0.751	0.071
50 993.299	10.720	11.602	11.547	−0.882	0.055
50 993.313	10.790	11.556	11.486	−0.766	0.070
50 994.304	10.897	11.627	11.550	−0.730	0.077
50 995.322	10.903	11.613	11.550	−0.710	0.063
50 996.326	10.860	11.595	11.533	−0.735	0.062
50 997.305	10.856	11.575	11.518	−0.719	0.057
50 998.383	10.861	11.607	11.549	−0.746	0.058
51000.366	10.814	11.575	11.526	−0.761	0.049
51010.427	10.871	11.620	11.555	−0.749	0.065
51010.433	10.911	11.640	11.539	−0.729	0.101
51013.450	10.812	11.555	11.460	−0.743	0.095
51013.456	10.811	11.546	11.468	−0.735	0.078
51014.310	10.913	11.696	11.599	−0.783	0.097
51014.315	10.869	11.624	11.596	−0.755	0.100
51015.312	10.939	11.660	11.607	−0.721	0.053
51015.318	10.960	11.667	11.619	−0.707	0.048
51016.421	10.899	11.622	11.572	−0.723	0.050
51017.353	10.963	11.705	11.639	−0.742	0.066
51018.467	11.022	11.694	11.608	−0.672	0.086
51020.330	11.120	11.804	11.736	−0.684	0.068
51021.328	10.833	11.578	11.509	−0.745	0.069
51021.334	10.817	11.591	11.520	−0.774	0.071
51022.294	10.780	11.546	11.461	−0.766	0.085
51022.299	10.775	11.542	11.468	−0.767	0.074
51022.307	10.742	11.523	11.464	−0.781	0.059
51023.294	10.884	11.643	11.591	−0.759	0.052
51023.299	10.902	11.657	11.601	−0.755	0.056
51024.287	10.762	11.514	11.475	−0.752	0.039
51024.292	10.769	11.529	11.482	−0.760	0.047
51024.298	10.745	11.532	11.472	−0.787	0.060
51026.278	10.805	11.545	11.469	−0.740	0.076
51026.283	10.807	11.533	11.490	−0.726	0.043
51078.253	10.848	11.591	11.526	−0.743	0.065
51081.273	10.835	11.586	11.536	−0.751	0.050
51101.194	10.788	11.534	11.475	−0.746	0.059
51109.194	10.793	11.531	11.462	−0.738	0.069
51112.193	10.877	11.620	11.553	−0.743	0.067
51115.193	10.914	11.649	11.611	−0.735	0.038
51336.449	10.891	11.625	11.575	−0.734	0.050
51345.430	10.903	11.630	11.578	−0.727	0.052
51347.423	10.911	11.651	11.619	−0.740	0.032

Table 1. (Contd.)

JD 2 400 000 +	*U*	*B*	*V*	*U–B*	*B–V*
51351.430	10.980	11.698	11.636	−0.718	0.062
51364.354	10.850	11.602	11.537	−0.752	0.065
51370.428	10.834	11.589	11.517	−0.754	0.072
51400.381	10.882	11.647	11.602	−0.765	0.045
51402.403	10.984	11.720	11.659	−0.736	0.061
51403.278	11.000	11.750	11.687	−0.750	0.063
51407.313	10.957	11.701	11.650	−0.744	0.051
51409.302	10.981	11.691	11.633	−0.710	0.058
51411.292	10.925	11.667	11.617	−0.742	0.050
51412.292	10.960	11.699	11.644	−0.739	0.055
51452.252	10.784	11.533	11.460	−0.749	0.073
51459.214	11.082	11.785	11.730	−0.703	0.055

let numbers of the main line, as well as additional contributors, if any. A blend is denoted by "bl." The instrumental wavelengths at the edges of an echelle frame are considerably less accurate than they are in the central part because of the distortions introduced by the dispersion curve. In several cases, the accuracy reached even 0.5 Å. Lines in unfavorable portions of the frame are marked with stars (★). Some emission lines, for example, [Fe II] 4413.8, 4416.3, and 4639.7 Å, are severely distorted by the stellar O II 4414.9, 4417.0, and 4641.8 Å absorption features in their wings, which introduces an error in the wavelength of both the emission peak and the absorption-line position (Fig. 2).

SPECTRUM OF THE CENTRAL STAR

The stellar component of the V886 Her spectrum represents the spectrum of a hot B1 II supergiant with a

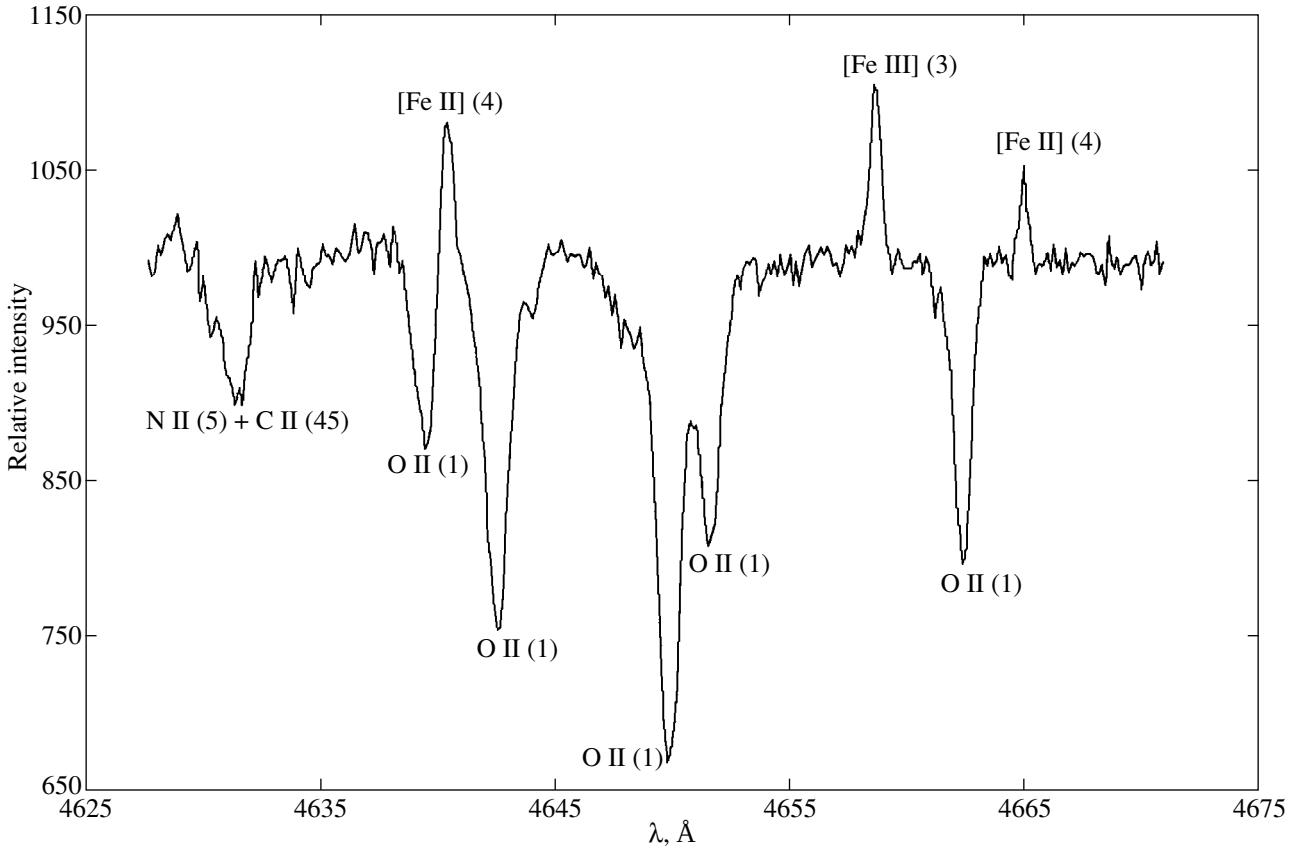

Fig. 2. The 4625–4675 Å spectrum of V886 Her.

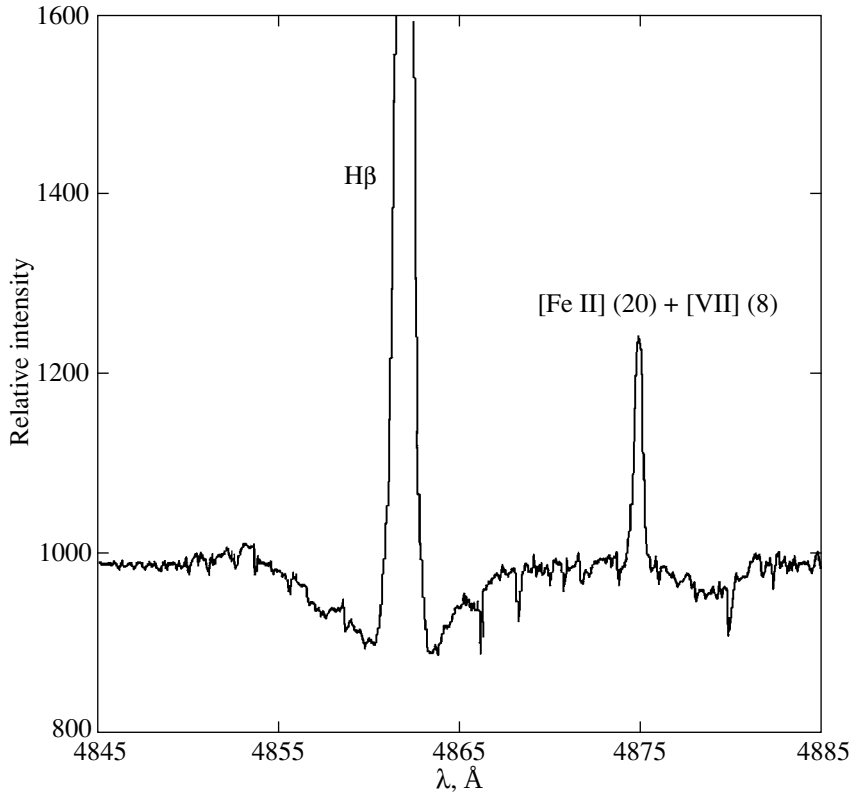

Fig. 3. The Hβ profile in the V886 Her spectrum.

temperature of ~25 000 K (Arkhipova *et al.* 1998), the future nucleus of a planetary nebula. The overwhelming majority of absorption lines in the stellar spectrum, apart from H I and He I lines, belong to O II (52 lines), N II (60 lines), C II (~30 lines), and Si III (5 lines); we also identified Mg II, Ca II, and Al III lines. There are weak Si IV, S II, C I, N I, and O I absorption features.

The hydrogen- and helium-line profiles are complex. They are a superposition of a stellar absorption line with comparatively broad wings and a narrow strong emission feature of the envelope. Figure 3 shows the Hβ profile. The width of the Hβ absorption wings points to a not-too-low value of $\log g$. The Hα line is entirely filled with emission (Fig. 4), and no absorption component is seen. An emission component is also present in Hγ. The He I 5016, 5876 (Fig. 5), and 7065 Å lines exhibit P Cyg profiles with intense emission components. The remaining helium lines at 4388, 4437, 4471, 4713, 4922, 5048, and 6678 Å are seen in absorption.

SPECTRUM OF THE ENVELOPE

Apart from hydrogen and helium lines, the emission spectrum of the envelope shows numerous metal lines. The hydrogen lines apparently have P Cyg profiles, although the emission feature dominates. For this reason, the total Hβ profile is slightly asymmetric about the central emission peak (Fig. 3). The emission spectrum of the envelope is not yet typical of even the lowest excitation planetary nebula. This is mainly because the nebular [O III] 4959, 5007 (see Fig. 6), and 4363 Å lines are absent (see Fig. 6) and because strong emission features of singly ionized metals are present.

Table 2. Mean radial velocities of V886 Her as measured from lines of various ions

Species	Emission/absorption	Number of lines	$\langle V_r \rangle$, km s^{-1}
H I	Emission Hα, Hβ, Hγ	3	51.72 ± 1.20
He I	Absorption	4	45.12 ± 1.30
He I	Emission	2	60.30 ± 1.60
N II	Absorption	8	57.18 ± 1.50
O II	Absorption	8	57.60 ± 1.50
C II	Absorption	2	52.85 ± 1.20
Si III	Absorption	4	55.60 ± 1.00
O I	Emission	2	49.19 ± 2.00
[O I]	Emission	1	52.65
N I	Emission	3	43.40 ± 5.00
Si II	Emission	4	53.00 ± 1.00
[Fe II]	Emission	28	51.81 ± 0.80
[Fe III]	Emission	2	54.22 ± 5.00
Fe II	Emission	2	51.58 ± 1.20
IS	Absorption	5	–12.55 ± 0.70

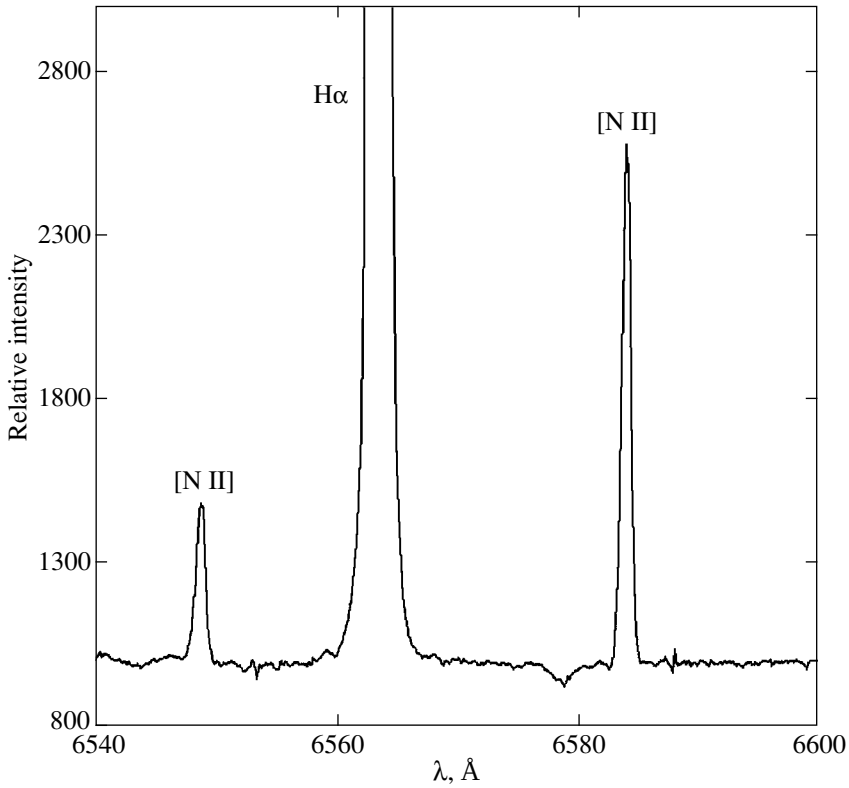

Fig. 4. The Hα profile in the V886 Her spectrum.

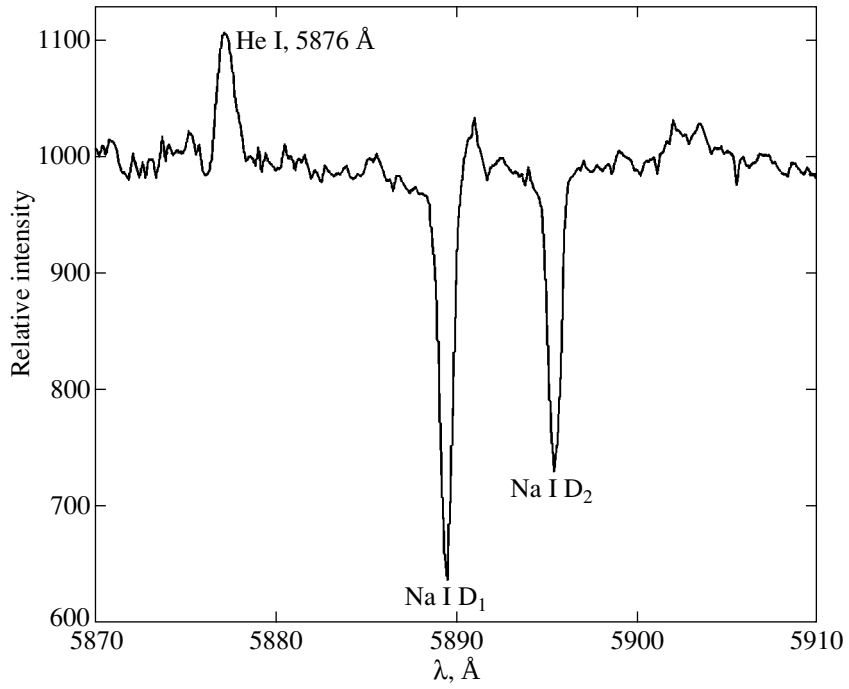

Fig. 5. The λλ5870–5910 Å spectrum of V886 Her. The Na I D_1 and D_2 and He I λ5876 Å lines are marked.

The emission spectrum of the envelope is formed by numerous permitted and forbidden lines of ionized metals [Fe II], Fe II, [Fe III] (and, possibly, Fe III), [Cr II], [Ti II], Ti II, [V II], V II, [Zr II], [Ni II], [Cu II], and [Mn II], as well as of neutral metals [Ni I], [Cr I], and [Ti I]. There are [N II], [S II], and [O I] emission features characteristic of the spectra of low-excitation planetary nebulae and strong O I, N I, and Si II emission lines.

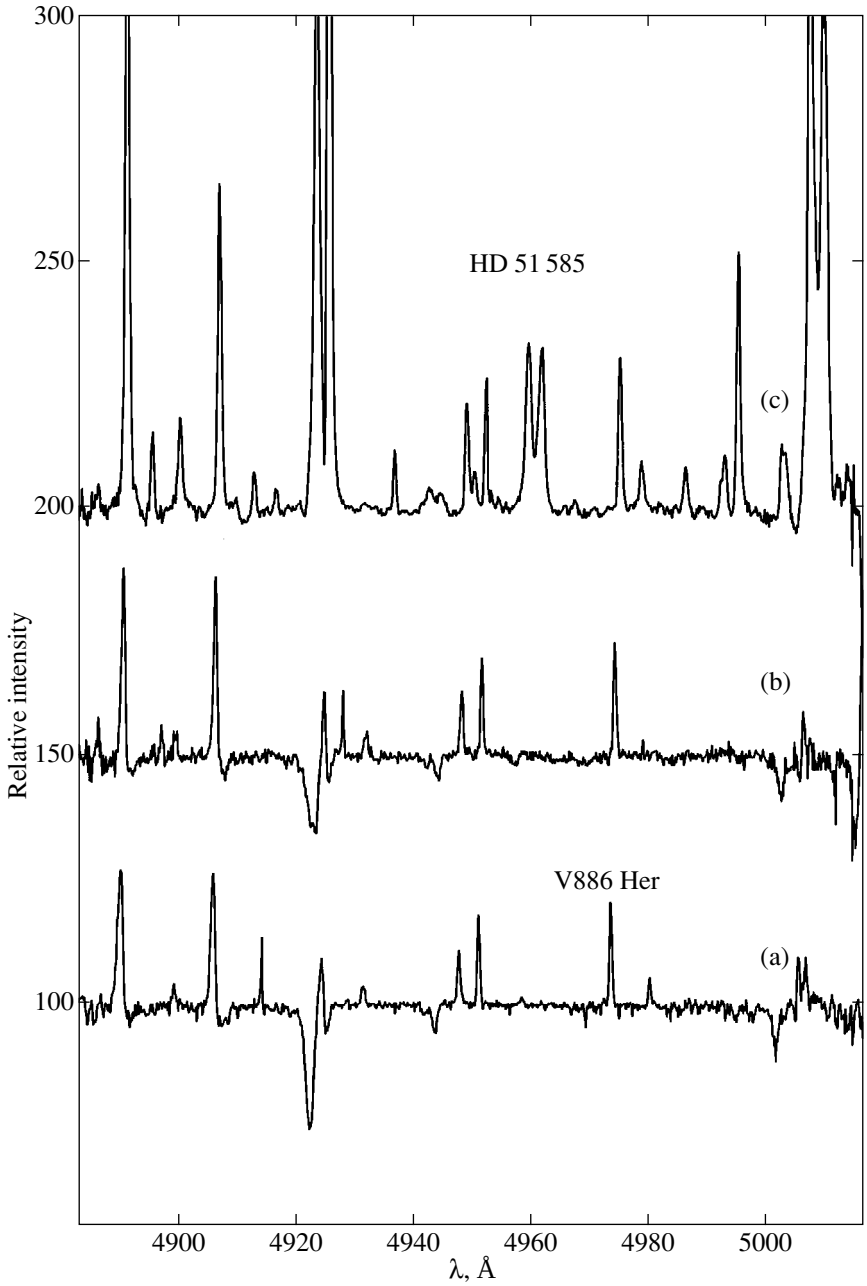

Fig. 6. The 4880–5020 Å spectra for V886 Her taken on (a) February 26, 1997, and (b) July 8, 1998, and (c) for HD 51 585.

The Na I D_1 5890 Å line has a P Cyg profile with a weak emission component and a noticeably blueshifted strong absorption component (Fig. 5).

Previously (Arkhipova *et al.* 1998), we measured the fluxes from the envelope in some emission lines in order to determine its parameters. In particular, we estimated the gas electron density and electron temperature from the measured intensity ratio of the [S II] doublet lines in the red spectral range and from the measured intensity ratio of the auroral and nebular [N II] lines, respectively. We also measured the red fluxes in the forbidden [O II] 7320–31 Å lines and the permitted O I 7002, 7254 Å and N I 7423, 7442, and 7468 Å lines.

HELIOCENTRIC RADIAL VELOCITIES OF V886 HER

Having identified the spectrum of V886 Her, we measured its radial velocities from the positions of about 100 most reliable emission and absorption lines. However, the wavelengths of some forbidden lines are not accurate enough even at present. The systematic corrections (Delta V_r – X_coord) along echelle orders

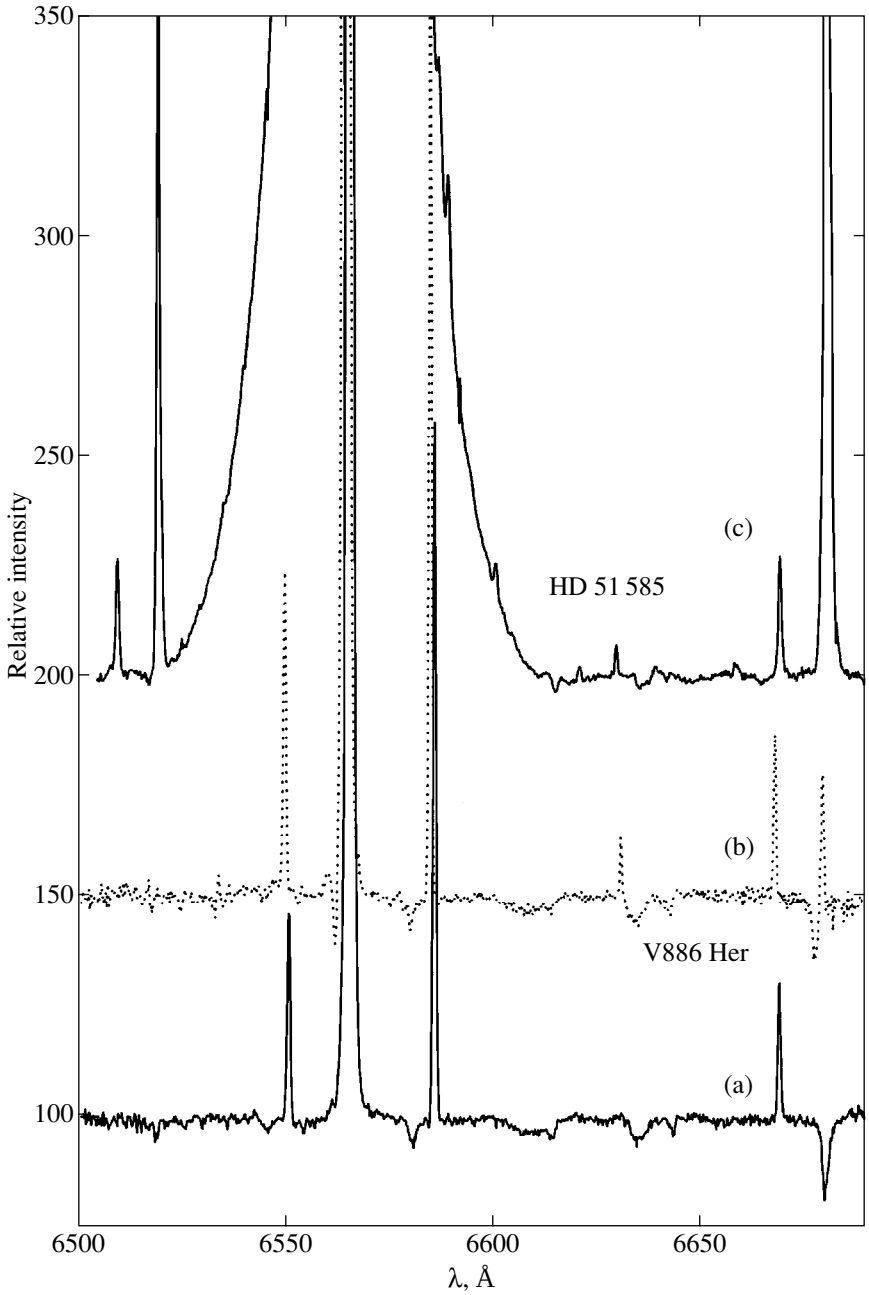

Fig. 7. The 6500–6690 Å spectra for V886 Her taken on (a) February 26, 1997, and (b) July 8, 1998, and (c) for HD 51 585. Note that a narrow absorption feature of the P Cyg profile appeared in Hα of the V886 Her envelope in 1998.

were determined from the positions of telluric lines in the spectrum and then applied.

We estimated the mean radial velocity from lines of each element at various ionization stages. The results are given in Table 2.

The mean velocity as measured from the main absorption lines is $\langle V_r$(N II, O II, C II, Si III)$\rangle = +55.72 \pm 1.60$ km s^{-1} and corresponds to the radial velocity of the star itself. The velocities measured from He I absorption lines deviate significantly (by more than 3σ) from the above value. This may be because the envelope's emission line having a P Cyg profile with its absorption component on the short-wavelength side is superimposed on the stellar absorption feature. There is excellent agreement between the mean velocities measured from H I, [Fe II], and Fe II emission lines, suggesting that they originate in the same ionization zone. The mean velocity measured from all emission lines is $\langle V_r$(H I, O I, [O I], Si II, Fe II, [Fe II], [Fe III])$\rangle = +50.95 \pm 1.54$ km s^{-1}.

The difference between the radial velocity measured from emission features of the envelope and the star's

velocity may result from the shielding of the envelope's back side by the star. This effect shows up only for an envelope radius comparable to the stellar radius.

Diffuse interstellar bands (DIBs) and intense Na I D_1 and D_2 absorption lines are clearly seen in the spectrum of V886 Her. The mean velocity of clouds on the line of sight was estimated from the 5780.41, 5797.03, 6195.95, 6203.19, and 6613.63 Å DIBs to be –12.55 km s^{-1}. The velocity measured from the Na I absorption components was found to be larger: –8.6 km s^{-1} from D_1 and –6.9 km s^{-1} from D_2. The Na I lines in the spectrum are more intense than might be expected for the estimated interstellar extinction toward V886 Her. The measured equivalent width of the D_1 line is W_λ = 0.36 Å. The color excess for IRAS 18 062+2410 is $E(B–V)$ = 0.3 (Arkhipova *et al.* 1998); the interstellar medium and the circumstellar dust envelope apparently account for 0.1 and 0.2 of this excess, respectively. It should then be recognized that there is also a circumstellar absorption component in the Na I line profile, which affects the radial-velocity determination.

COMPARISON OF V886 Her WITH HD 51585

V886 Her is similar in pattern of photometric variability and spectrum to HD 51 585 = OY Gem, another candidate for protoplanetary objects (Arkhipova 1989; Arkhipova and Ikonnikova 1992). HD 51 585 also exhibits irregular light variations caused by a variable stellar wind, which is also confirmed by variations in the Hα emission profile. There are also cold and hot dust envelopes. The spectrum of HD 51 585 contains numerous emission lines.

The spectra of V886 Her and HD 51585 in some representative wavelength ranges are compared in Figs. 6 and 7; for V886 Her, we also show the July 8, 1998, spectrum taken with the 6-m telescope (Fig. 7b). All spectra were obtained with the same observational configuration.

A detailed comparison of the spectra reveals several significant differences. First, the spectrum of the HD 51585 envelope exhibits the [O III] 4959, 5007, and 4363 Å lines (Fig. 6) and, possibly, He II lines (Jaschek *et al.* 1996). This points to a higher degree of ionization in the HD 51585 envelope than that for V886 Her and a higher temperature of the ionizing star. Observations of HD 51 585 revealed a systematic flux rise in hydrogen and helium lines, which strongly suggests the ongoing envelope ionization.

Second, no absorption lines were observed in the HD 51585 spectrum, except the absorption components of the P Cyg profiles for several emission features (Jaschek *et al.* 1996). Third, the hydrogen and helium emission lines in HD 51585 have broad wings, up to 3000 km s^{-1}, at zero Hα intensity (Swings and Andrillat 1981) (Fig. 7), suggesting a significant role of the stellar wind in forming the stellar spectrum. It may be assumed that the central star of the future planetary nebula in HD 51585 will have or already has WR characteristics. By contrast, V886 Her still has a central star with absorption lines. However, our 1998 observations of V886 Her reveal an enhancement of the emission spectrum (Figs. 6, 7). V886 Her may evolve toward the state of HD 51585.

The He I lines in the spectra of both stars have P Cyg profiles. In the later spectrum of V886 Her, this feature is considerably more pronounced than it is at an earlier time of observations. In 1998, we also see a narrow absorption component of the P Cyg profile in the Hα emission line (Fig. 7) belonging to the envelope. The intensity of emission lines in the 1998 spectrum generally increased.

Since the two stars are undoubtedly of great interest as likely representatives of the initial planetary-nebula stage, their further photometric and spectroscopic monitoring is highly desirable.

ACKNOWLEDGMENTS

V.G. Klochkova's spectroscopic study of protoplanetary nebulae with the 6-m SAO telescope was supported by the Russian Foundation for Basic Research (project no. 99-02-18339).

REFERENCES

1. V. P. Arkhipova, Pis'ma Astron. Zh. **15**, 925 (1989) [Sov. Astron. Lett. **15**, 400 (1989)].
2. V. P. Arkhipova and N. P. Ikonnikova, Pis'ma Astron. Zh. **18**, 1017 (1992) [Sov. Astron. Lett. **18**, 418 (1992)].
3. V. P. Arkhipova, N. P. Ikonnikova, V. F. Esipov, and R. I. Noskova, Pis'ma Astron. Zh. **22**, 526 (1996) [Astron. Lett. **22**, 470 (1996)].
4. V. P. Arkhipova, N. P. Ikonnikova, R. I. Noskova, *et al.*, Pis'ma Astron. Zh. **25**, 30 (1999).
5. T. Blöcker, Astron. Astrophys. **299**, 755 (1995).
6. C. Jaschek, Y. Andrillat, and M. Jaschek, Astron. Astrophys., Suppl. Ser. **117**, 281 (1996).
7. A. B. Meinel, A. F. Aveni, and M. W. Stockton, *Catalog of Emission Lines in Astronomical Objects* (Optical Scientific Center and Steward Observatory, Tucson, 1969).
8. Ch. E. Moore, *A Multiplet Table of Astrophysical Interest* (Princeton Univ. Observatory, 1945), No. 20.
9. V. E. Panchuk, I. D. Naĭdenov, V. G. Klochkova, *et al.*, Byull. Spets. Astrofiz. Obs. **44**, 127 (1998).
10. J. P. Swings and Y. Andrillat, Astron. Astrophys. **103**, L3 (1981).
11. K. M. Volk and S. Kwok, Astrophys. J. **342**, 345 (1989).

Translated by V. Astakhov